Laser Welding of Nickel-Titanium and Stainless Steel Wires: Processing, Metallurgy and Properties

THÈSE N^{O} 5120 (2011)

PRÉSENTÉE LE 16 SEPTEMBRE 2011

À LA FACULTÉ SCIENCES ET TECHNIQUES DE L'INGÉNIEUR
CENTRE INTERDISCIPLINAIRE DE MICROSCOPIE ÉLECTRONIQUE
PROGRAMME DOCTORAL EN SCIENCE ET GÉNIE DES MATÉRIAUX

ÉCOLE POLYTECHNIQUE FÉDÉRALE DE LAUSANNE

POUR L'OBTENTION DU GRADE DE DOCTEUR ÈS SCIENCES

PAR

Jonas VANNOD

acceptée sur proposition du jury:

Prof. A. Mortensen, président du jury
Prof. M. Rappaz, Dr A. Hessler-Wyser, directeurs de thèse
Dr L. Bataillard, rapporteur
Dr D. Daloz, rapporteur
Prof. R. Schaller, rapporteur

ÉCOLE POLYTECHNIQUE
FÉDÉRALE DE LAUSANNE

Suisse
2011

Résumé

L'industrie biomédicale a des besoins en constante augmentation dans le domaine des assemblages de matériaux dissimilaires, ceux-ci étant utilisés pour la production de pièces complexes, comme les fils-guides et autres instruments intravasculaires. Leur production est d'autant plus difficile que leurs composants sont de taille micrométrique. Les alliages de nickel-titane sont couramment utilisés pour leur propriété de mémoire de forme et leur résistance à la corrosion. Cependant, ces alliages s'assemblent difficilement avec les autres métaux biocompatibles et tout spécialement les métaux ferreux comme les aciers inoxydables.

Le soudage laser est une technique de choix pour la production d'assemblages de taille réduite et de forme complexe. En effet, la haute densité d'énergie délivrée par un laser permet de réduire la taille de la zone affectée thermiquement et la vitesse de refroidissement élevée peut être utilisée pour éviter la formation de certaines phases, et ceci plus particulièrement dans le cas du soudage de matériaux dissimilaires. De plus, la polyvalence de cette technique permet de varier le facteur de dilution dans le bain de soudure afin de favoriser la formation d'une microstructure particulière.

Lors de ce travail de thèse, le procédé de soudage laser a été appliqué au cas de la soudure de fils superélastiques de nickel-titane (NiTi) et d'acier inoxidables (Inox), lesquels ont un diamètre inférieur au millimètre. Les propriétés mécaniques et la microstructure des soudures ont été optimisées en variant les paramètres de soudage, que ce soit dans le cas d'un laser pulsé ou continu, afin d'obtenir des soudures de bonne qualité.

Dans un premier temps, le système NiTi-Inox a été étudié par solidification contrôlée, afin de pouvoir caractériser le chemin de solidification et la microstructure finale, ceci en variant le facteur de dilution des matériaux de départ. Ces expériences de solidification (Bridgman et four infrarouge) ont été mises en relation avec le diagramme de phase Ni-Ti-Fe afin d'identifier les phases pouvant se former en cours de soudage laser dissimilaire.

Ensuite, le procédé de soudage laser a été optimisé sur la base des résultats précédents tout en utilisant plusieurs variables agissant spécifiquement sur l'intervalle de solidification, le facteur de dilution et la vitesse de refroidissement. Les soudures ont été testées en traction et leurs faciès de rupture ont été analysés afin de détecter les paramètres pour lesquels les soudures présentent une bonne résistance mécanique, et ceci de façon reproductible.

Finalement, le mécanisme de rupture a été étudié afin de comprendre la limitation de la résistance mécanique des soudures par la contrainte superélastique du NiTi. Des expériences de traction *in situ* , la caractérisation des propriétés mécaniques ainsi qu'une modélisation ont été réalisées afin de déterminer quel mécanisme de fracture est activé à l'interface NiTi-soudure.

Sur la base de ces résultats, un modèle composite rudimentaire a été conçu pour expliquer la localisation précise de la fracture et sa contrainte maximale équivalente à la limite superélastique. Enfin, quelques perspectives sont évoquées pour éviter cette limitation de

la résistance mécanique.

Cette thèse met l'accent sur le besoin de conjuguer différentes techniques complémentaires, comme l'analyse des propriétés mécaniques, du chemin de solidification et de la modélisation pour aborder les problèmes complexes liés aux matériaux, tels que la soudure laser de matériaux dissimilaires.

Mots-clés : soudage laser ; matériaux dissimilaires ; nitinol ; acier inoxidable ; alliages Fe-Ni-Ti ; fils-guides ; modélisation ; test de traction *in situ* ; microscopie électronique ; solidification Bridgman ; Four infrarouge ; nanoindentation ; solidification ; intermétallique.

Abstract

The biomedical industry has an increasing demand for dissimilar metal joining processes, which are used for complex configuration designs, such as guidewires and other intravascular interventional devices. Their production becomes more and more challenging as they decrease in size to reach components at the micron range. Nickel-titanium alloys are commonly used for their shape memory and biocompatibility properties, but are difficult to combine with other biocompatible metals, especially ferrous alloys such as stainless steels.

Laser welding is a promising technique to achieve such small and complex shape joints. Indeed the laser high energy density reduces the size of the heat affected zone and the high cooling rate can avoid unwanted phase formation, especially in the particular case of dissimilar joining. Moreover, the high versatility of the technique allows to change the dilution factor in the weld pool in order to carefully select the joint microstructure.

In this thesis, the laser welding process has been applied to superelastic nickel-titanium (NiTi) joining to stainless steel (SS) in the case of submillimetric diameter wires. The welded couple strength and microstructure have been optimized by investigating the influence of the laser parameters of both pulsed and continuous laser welding modes, to achieve sound welds.

First, the NiTi-SS system has been studied using controlled speed solidification experiments that were performed to characterize the solidification path and its resulting microstructure according to the dilution factor of the base materials. Bridgman and infrared furnace experiments were correlated to the ternary Ni-Ti-Fe phase diagram to identify the possible phases that might form during laser dissimilar welding.

Then, the laser welding process was optimized according to the previous results using several parameters to modify the solidification interval, dilution factor and cooling rate in particular. The weld quality was characterized by tensile testing and fracture surface analyses, in order to select the welding parameters leading to repeatable sound welded couples.

Finally, the fracture behaviour of the welded couples was carefully investigated to understand the limitation of the tensile strength by the NiTi superelastic stress. *In situ* tensile experiments, mechanical property characterization and modelling were performed to determine the fracture mechanism occurring at the NiTi-weld interface during testing.

Based on these observations, a simple composite model was designed to explain this precise fracture location and the upper limit, which is equal to the superelastic stress. Moreover, perspectives were detailed in order to possibly avoid this mechanical strength issue.

This thesis has also emphasized the need to connect several complementary techniques, such as mechanical properties investigations, solidification path characterization and modelling to tackle complex materials science issues, such as dissimilar laser welding.

Keywords: laser welding; dissimilar materials; nitinol; stainless steel; Fe-Ni-Ti alloys; guidewires; modelling; *in situ* tensile testing; electron microscopy; Bridgman solidification; infrared furnace; nanoindentation; solidification; intermetallic.

Remerciements

Cette thèse est un travail réalisé en collaboration entre le laboratoire de simulation des matériaux (LSMX), le centre interdisciplinaire de microscopie électronique, tous deux faisant partie de l'École Polytechnique Fédérale de Lausanne (EPFL), et finalement la Haute École Spécialisée de Suisse Occidentale (HES-SO). Cette recherche a été financée par la commission suisse pour la technologie et l'innovation (CTI, projet n° : 8545.1) et par un partenaire industriel (Heraeus Medical Components Division, à Yverdon-les-Bains).

Avant tout, je tiens à remercier largement et le plus généreusement possible les deux personnes m'ayant principalement guidé durant ces quatre belles années. Le directeur du LSMX et également celui de ma thèse : le professeur Michel Rappaz. Je désire lui faire part de toute ma reconnaissance, pour ses encouragements dans les moments difficiles et ses conseils avisés face aux différents problèmes rencontrés durant ce travail. Mais également pour l'ambiance amicale et franche qui règne au LSMX, un véritable encouragement au travail, sans oublier son côté humain et généreux. La co-directrice de ma thèse, la docteur Aïcha Hessler-Wyser, pour son aide dans le domaine de la microscopie électronique et son soutien au cours de cette recherche, ainsi que pour son aide et son encouragement durant la période de rédaction du manuscrit.

Je tiens également à remercier les personnes de la HES-SO ayant participé à ce travail et, en particulier, le professeur Jacques-Eric Bidaux pour sa disponibilité et ses conseils dans le domaine des alliages à mémoire de forme. Le docteur Samuel Rey-Mermet pour sa patience et sa persévérance lors des tentatives de DTA, TGA, et pour la réalisation de nombreux essais mécaniques. De même que Yan Gex-Collet et Vincent Sonney, pour leurs aides respectives sur le projet.

Ma gratitude va aussi au partenaire industriel du projet et plus précisément aux personnes ayant donné écho à mes demandes. Le docteur Laurent Bataillard pour son travail de responsable de projet, mais également celui de rapporteur dans le jury de thèse. Ainsi qu'à Marc-Olivier Lévesque et le docteur Nuno Fazenda pour leur aide dans mes relations avec le monde industriel, et Olivier Müller, Pierre Casteras et Roland Freymond pour leur secours technique.

J'adresse également mes remerciements aux autres membres du jury pour le temps qu'ils ont consacré à évaluer ce manuscrit et leurs remarques enrichissantes lors de l'examen de thèse : le président du jury, le professeur Andreas Mortensen et les rapporteurs, le professeur Robert Schaller et le docteur Dominique Daloz.

Ma reconnaissance va aussi aux différentes personnes ayant participé à l'obtention des résultats au cours de ce travail. Le professeur Michel Bornert pour la technique de corrélation d'images. Le docteur Ayat Karimi pour les essais de nanoindentation. Le docteur

Jean-Marie Drezet pour la modélisation mécanique. La société BREDAM pour la réalisation des essais de soudage par laser continu, et tout spécialement René Gilliard et Alain Woodtli. Sans oublier Jean-Luc Desbiolles pour son infinie patience et son enseignement de la modélisation thermique, ainsi que les services informatiques en tous genres.

Je remercie également les étudiantes Nadia Marxter et Krista Lumsden qui, de par leurs projets de semestre, ont fait avancer cette recherche.

Tout ce travail n'aurait pas vu le jour sans l'aide de Jean-Daniel Wagnière, qui a activement contribué à tous les résultats expérimentaux. Ainsi que l'équipe de l'atelier mécanique des matériaux (ATMX) : Pierre-André Despond, Werner Bronnimann, Adrien Grisendi, Eric Vassalli, Yves Ruschetta et Jean-Marc Colomb. De même que Grégoire Baroz pour son entretien consciencieux des microscopes électroniques.

Viennent ensuite les collaborateurs ayant partagé leurs idées, leur temps et l'excellente ambiance au sein du LSMX et du CIME, et plus particulièrement :

- Jonathan Friedli, pour son amitié sans borne, ses passions, ses idées et tout le temps partagé durant ces dix dernières années à l'EPFL.
- La professeur Cécile Hébert, pour m'avoir accueilli dans son propre laboratoire avant d'y être arrivé elle-même.
- Le professeur Philippe Buffat, le docteur Antonin Faes, Emad Oveisi et le docteur Paolo Di Napoli, pour avoir partagé de nombreuses discussions dans le même bureau.
- Le professeur Pierre Stadelmann pour son aide lors de l'utilisation de Mathematica© et ses propos encourageants.
- Pierre Burdet pour les reconstructions FIB et l'analyse EDX.
- Guillaume Pasche pour les reconstruction des faciès de rupture avec MeX© et son aide pour les plans d'expériences (DoE).
- Ruth Gacoin, Annick Evéquoz et Anne Roy pour leurs aides face aux tracas de l'administration.
- Ainsi que tous les anciens doctorants de ces laboratoires, pour leur conseils avisés et toujours à propos. Et en particulier les docteurs Denis Favez, Mario Alberto Salgado Ordorica et Aurèle Mariaux.

Finalement, mon infinie gratitude va à ma famille : mes parents pour les encouragements, et surtout à Virginie et nos enfants, pour leurs sourires et tout l'amour qu'ils m'ont témoignés au cours de la réalisation de cette thèse.

Contents

Chapter 1

Introduction

Over the last decades, the biomedical sector has become one of the most demanding fields of development in engineering. Indeed, life sciences constantly need research and development of new processes, materials and technologies to improve the medical surgery tools, such as expendable stents to cure coronary diseases or biocompatible cements and implants for bone repair or replacement.

Among the various materials used in this field, nickel-titanium (NiTi) alloys are well-known commonly-used materials for their pseudoelastic, shape memory, biocompatibility and corrosion properties, when atomic compositions of nickel and titanium are similar, i.e., near the NiTi stoichiometric composition [1]. They are used in particular for the design of medical devices dedicated to minimal invasive surgery, such as catheter guidewires, stents or coil anchors. To extend the use of these alloys, there is a particular interest in joining them with other biocompatible metals, such as Stainless Steel (SS) or platinum-iridium (Pt-Ir) alloys.

Different joining techniques are well-known for combining dissimilar materials. However, the use of a final product as an invasive tool inside human body implies several constrains, such as chemical stability, mechanical strength or surface aspects. Three main categories define the joining processes, according to the nature of their bounds:

Mechanical joining processes are widely used for joining metallic pieces, but are much more difficult to implement on submillimetric devices. Nevertheless, if bolting or riveting are no choice, lock-seam forming could be used for small wires joining. However, accurate machining is difficult to achieve and remaining voids between the pieces have a negative impact on the biocompatibly of the joint. In addition, machining reduces the section of the wire and stress are concentrated at the interface between the pieces.

Chemical joining processes are used to bond metallic pieces with the addition of an adhesive as a filler material. The adhesive material is usually an organic compound, which reduces the biocompatibility of the combined device because of the presence of solvents or reactants. The mechanical properties of the bond are usually weaker than that of the base materials, especially when dealing with metals. Thus, most of the glued devices have reduced biocompatibility and mechanical properties, and are difficult to implement on submillimetric wires.

Physical joining processes are the last category of joining techniques and mainly consist in welding for metallic materials.

The latter methods are the most likely to be applied to biomedical submillimetric devices, because their resulting strength is similar to that of the base material and the final welded surfaces have a good aspect, which reduces possible post-processing issues. This group of techniques can be subdivided into three main classes, according to their processing temperature and whether filler materials are used or not:

Soft soldering is the operation in which metallic pieces are joined by means of a molten filler metal. The latter, having a melting temperature lower than that of the pieces to be joined and below 450 °C, wets the base metal. The base materials are not molten, and thus do not participate in the formation of the joint.

Brazing is quite similar to soft soldering, but the filler material has a melting temperature higher than 450 °C. This temperature difference makes the filler material to diffuse inside the base materials and makes stronger bonds, but can produce intermediate phases.

Welding is a process requiring the melting of the original pieces. A filler material, with a melting temperature similar to that of the base materials, may possibly be added to the beam. The bond strength is higher than with the previous techniques and the heat affected zone (HAZ) is smaller due to the shorter interaction time.

Welding is a very promising technique for joining NiTi submillimetric wires, especially due to the easy automation capability of the process. Moreover, the oxidation of NiTi alloys is more likely to be decreased as the HAZ is smaller. The latter aspect also avoids the mechanical property changes in the base wires, especially the loss of shape memory effect or superelasticity in the NiTi wire. Nevertheless, welding dissimilar metals can lead to the formation of unwanted phases, such as intermetallic compounds or metastable phases.

The required heat, needed to reach the melting temperature of the base materials, can be brought by several means, such as electron beam, electric arc, Joule's effect or laser. The latter being especially appropriate to the thin wire welding as no contact is required and the heat flux can be dispensed on the whole perimeter, using an orbital welder. Moreover, the high heating and cooling rates of the laser welded pieces reduce the formation of unwanted phases, but internal stress may be an issue.

1.1 Motivation of the project

Strokes are the most common life-threatening neurological disease, and are the third cause of death in developed countries after heart disease and cancer. In order to reduce open surgical procedures, the biomedical sector is very demanding on complex dissimilar compounds, especially in the field of intracranial invasive surgery. Indeed, NiTi-based guidewires are essential for ensuring the stable delivery of interventional devices.

Design of such medical devices is getting more and more challenging as they decrease in size to reach components at the micron scale. Materials need to be redefined to make sure that their mechanical characteristics and behaviour remain at the required level and assemblies have to be reconsidered so that heterogeneous materials can be combined to reach the highest level of requirements.

This project aims for mastering the weld ability of very thin NiTi wires to other materials, while guaranteeing the mechanical stability of heterogeneous welding. To get

a better control and understanding of the mechanisms involved in dissimilar materials laser welding, mechanical and microstructural properties have been studied on reference welded specimens at sub-micron scale. This was performed in combination to controlled solidification investigations of NiTi-SS alloys. A laser welding process has been tested and improved to reach maximal tensile strength of the joints between NiTi and SS wires.

1.2 Structure of the thesis

If the associated industrial project mainly aims for the production of sound laser welded submillimetric wire couples, this thesis tends to analyse more fundamentally the problematic of dissimilar NiTi-SS welding. It focusses on the mechanical and chemical aspects resulting from the different laser welding conditions and the formed microstructures.

Chapter 2 presents a state of the art review of the NiTi-SS system. The possible interactions between elements are evaluated and discussed to reduce the system to the ternary Fe-Ni-Ti system. Moreover, a review of laser welding and its characteristic issues is presented, especially in the field of rapid solidification.

Chapter 3 describes the used experimental devices. The orbital wire welding positioning setup on both pulsed and continuous laser is explained and illustrated. The controlled solidification experiments, such as Bridgman and infrared furnace, are depicted. Finally the characterization techniques are outlined, the latter being used for microstructure analysis as well as for mechanical property investigations.

Chapter 4 summarizes the results of controlled solidification experiments. These were done to corroborate the simplification of the NiTi-SS dissimilar weld to the Fe-Ni-Ti ternary system and to define the starting point for the welding parameter optimization, based on the observed solidified microstructures.

Chapter 5 concerns the laser welding produced for the industrial approach of this project. The path followed to optimize the laser welding parameters producing the welded couples with the highest tensile strength is detailed and discussed.

Chapter 6 regroups the different investigations made to understand the fracture behaviour of the welded couples while tested in tension. The experiments performed to determine the mechanical properties and microstructure of the different domains are also reported and discussed.

Chapter 7 synthesizes and discusses the results of this work and summarizes the essential conclusions of this study. Several possible further investigations are also suggested to improve the understanding of the encountered issues and overpass them.

Chapter 2

State of the art

This chapter presents the bases and the relevant literature for the problem of laser welding of heterogeneous materials, such as nickel-titanium alloy and stainless steel. It is subdivided into two different sections, first an overview of the studied system and its subsystems (section 2.1), followed by a review of the laser welding state of the art (section 2.2). The elementary knowledge of applied Design of Experiment on the system is reported in appendix A.

2.1 Kinetics and phase transformations in the Ni-Ti-Fe system

This section mainly focusses on the different materials that have been used during this study. The biggest restriction is the need to join biocompatible materials, for invasive surgery tools or parts that will remain in bodies for long times.

The materials choice was reduced to nickel-titanium (NiTi, also called Nitinol) alloys, as their unusual mechanical characteristics are of high interest to design complex tools and devices, and grade 304V stainless steel (SS). NiTi alloys are well known for their biocompatible properties studied over the last decades [2, 3, 4]. SS, and especially the 304 grade, are also considered as biocompatible materials for medical applications and devices [5], although nickel and chromium are suspected to have a negative impact on living cells, as emphasized in orthodontic surgery [6, 7].

In the following subsections, the interactions between elements are discussed in order to predict the phases that may appear. First, the NiTi is presented alone, together with its shape memory properties. Then, the interactions that can occur when welding NiTi and SS on the basis of binary phase diagrams are discussed. Finally the ternary system of the main elements Fe-Ni-Ti will is presented.

2.1.1 Nickel-Titanium

Shape Memory Alloys (SMA) were first reported in the 1930s, according to Otsuka and Wayman [8], but no industrial application was developed at this early stage. The initial alloys where the shape memory effect (SME) was observed were gold-cadmium alloys, followed by copper-zinc (brass) alloys in 1938, and then many alloys were subsequently identified (Fe-Pt, In-Cd, Fe-Ni, Ni-Al, even stainless steels). In 1963, the Naval Ordnance Laboratory reported the discovery of shape memory property in the equiatomic inter-

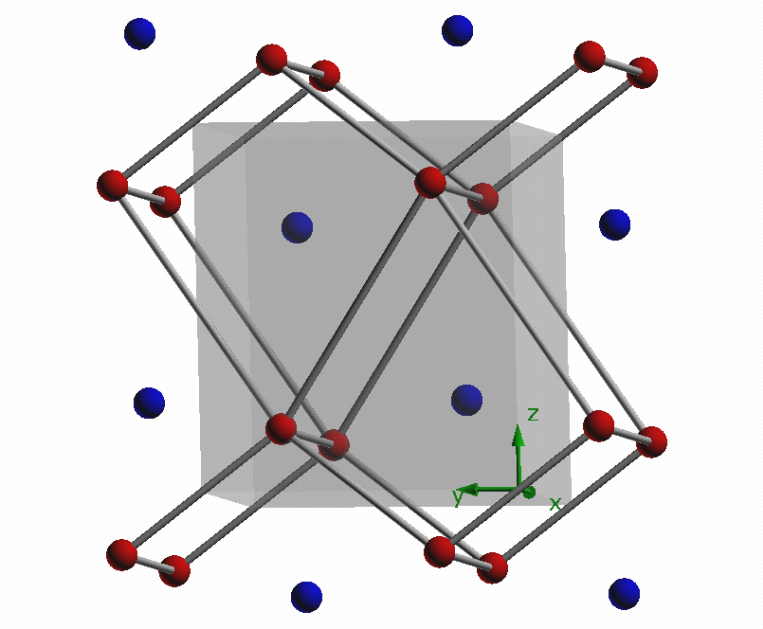

Figure 2.1: Monoclinic cell of the martensite phase of NiTi (highlighted in grey shade), showing both nickel and titanium atoms. The bonds drawn between atoms show the BCC structure of the prior austenite cubic cell, present before martensitic transformation, with its centred atom of the other species.

metallic phase of nickel-titanium alloys [9]. The first industrial use of this material was made by Raychem corporation in Menlo Park, under the name of Cryofit©. This was for cylinder used for pipe connections in the hydraulic industry, which were adjusted under liquid nitrogen [10].

Since then, nickel-titanium (NiTi) alloys are well known for their shape memory and superelastic properties, and widely used in several applications, such as industrial (automotive, robotics, aeronautic,...) or medical ones (optometry, surgery, orthodontics,...) [1].

Shape memory effect and superelasticity

Both Shape Memory Effect (SME) and SuperElasticity (SE) are intrinsic properties of the NiTi intermetallic phase, resulting from the austenite [1]-martensite phase transformation (martensitic transformation) and its inverse (austenitic transformation). These structure modifications occur without diffusion of species and are called diffusionless (or *military*) transformations. They result from an atomic rearrangement in the crystal and lead to crystal structure modifications. This type of phase transformations propagates with a motion of a glissile interface where the atoms move in coordination with each other and their neighbours remain unchanged. Contrariwise, a diffusion-based transfer (*civilian* transformation) along a non-glissile interface leads to an exchange in the surrounding atoms [11].

The martensitic transformation is the change between two NiTi crystal structures, which are stable over different temperature ranges. At low temperature, the martensite phase has a space group number 11, and a primitive monoclinic Bravais lattice, while at

[1]The denomination "austenite" for the mother phase is of course confusing as it has a body-centred cubic (BCC) and not a faced-centred cubic (FCC) structure.

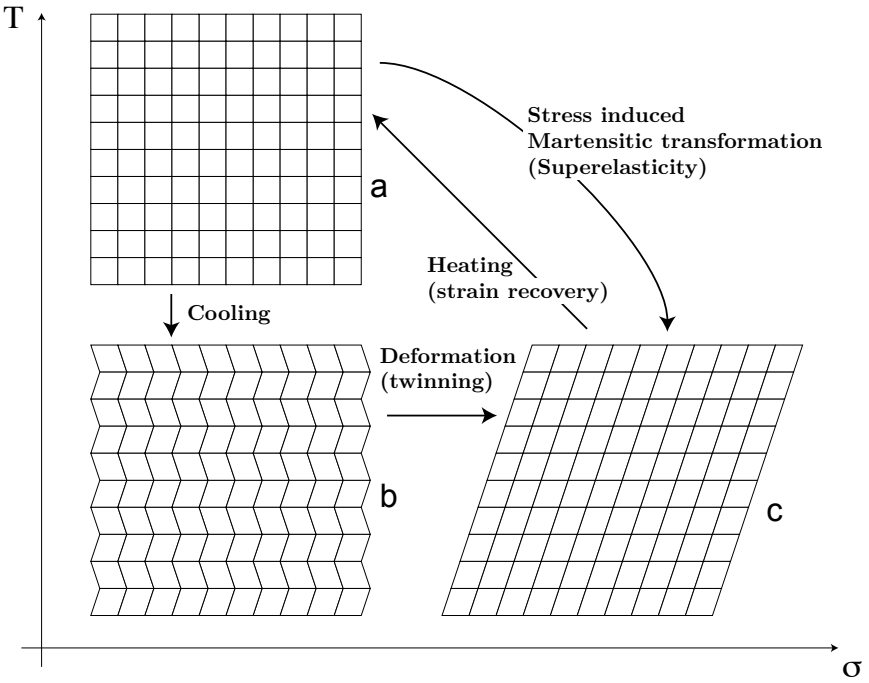

Figure 2.2: Martensitic phase transformation mechanism: during cooling, the austenite cubic structure (a) changes to martensite monoclinic (b), in a minimisation of strain process. When a shearing stress is applied, the martensite crystal deforms by twinning of the structure (c). During heating, the crystal structure goes back to cubic, which does not allow twinning and the original shape (a) is recovered. This is the so-called Shape Memory Effect (SME). An isothermal martensitic transformation can be induced by stress (a to c), leading to superelasticity (SE) of the material.

higher temperature, the austenite has a space group number 221, and a primitive cubic Bravais lattice (see Fig. 2.1 for an illustration of one variant of the crystal change [12]). This crystal structure change results in a local deformation of the structure, which is minimized by the twinning of the crystal (see Fig. 2.2, step a to b) [13].

Fig. 2.1 represents the atomic positions of both nickel and titanium atoms in the martensitic crystal. The grey shape represents the actual martensite unit cell and the bonds delimit the prior austenitic unit cell corresponding to the body-centred cubic structure. The martensite unit cell has the same volume per atom than the austenite structure. This emphasizes the important property of the martensitic phase transformation, being its quasi-equal density of the unit crystal cells. This leads to a phase transformation without volume change and thus, a Poisson's ratio of $\nu = 0.5$ [14].

In martensite structure, deformation up to 8% can be handled only by twinning of the microstructure, almost without crystal defect nucleation. This optimized fitting of the structure is made through the combination of several variants of martensite crystal orientation. A comprehensive study of the twelve possible variations of this orientation relation was made by Miyazaki *et al.* in 1989 [15].

When the sample is heated up into the austenite stability domain, the crystal structure goes back to a cubic lattice. This latter recovery is due to the inability of the austenite phase to produce a twinned structure, another crystal deforms back to its initial structure by diffusionless austenitic transformation. This peculiarity leads to a strong mechanical force to go back to the original sample shape, and to the original atomic positions of

each species due to the precise stoichiometric NiTi intermetallic composition, consisting in Shape Memory Effect (SME). The latter is observed in a range of temperatures defined by the composition of the NiTi alloy, typically between −20 °C and 60 °C (see Fig. 2.3a).

Usually this SME is visible only on heating of the sample, and during cooling it keeps it shape (see Fig. 2.2). However, a so-called training of the sample can lead to a two way SME. This is made by deformation and temperature cycles to induce a maximum of defects that are not stable in every variant of the crystal orientation, and thus lead to a two way SME. Liu and McCormick give more details on this effect [16].

The elasto-plastic mechanical behaviour of NiTi alloys is severely modified by the presence of a constant stress plateau (superelastic), when the transition temperature is below that of the test, the latter being usually room temperature (NiTi is in the austenitic state). This is called superelasticity (SE), especially because the elastic domain can sustain strains up to 10%. This effect is the result of a crystal structure change from austenite to martensite, induced by the stress state. Indeed, this martensite structure becomes thermodynamically stable under sufficient stress load, but recovers its stable austenite structure when stress is released. The variation between transformation temperature and global stress is given by the Clausius-Clapeyron relation:

$$\frac{\mathrm{d}\sigma}{\mathrm{d}T} = -\frac{\Delta H_0}{\varepsilon \cdot T_0} \tag{2.1}$$

where ΔH_0 is the specific enthalpy of transformation at standard condition, ε and T_0, the deformation and the temperature of the phase change respectively [8]. This relation is the basis of the stress-induced martensitic transformation, governing the transition temperature and the external stress required to induce martensitic transformation (superelastic plateau). Thus, theoretically, the superelastic stress increases proportionally to the interval between testing and martensitic transformation temperatures. However, inhomogeneities (such as defects, variant phases,...) induce internal stresses changing the actual superelastic plateau stress.

NiTi Binary Phase Diagram

NiTi alloys are most of the time produced with a nearly equiatomic composition in order to form NiTi stoichiometric intermetallic compound with specific properties (see Chap 2.1.1). However, except for the two pure element phases ((Ti) and (Ni) phases), the equilibrium phase diagram shows two more intermetallic compounds: Ti_2Ni and $TiNi_3$ (see Fig. 2.3b).

Titanium-rich NiTi alloys (48-50% at. Ni) are used as two-way SME alloys, due to the high martensite transformation temperature (see Fig. 2.3a), combined with a training [19]. Nevertheless, these lower nickel concentration alloys are subject to precipitation of Ti_2Ni particles during solidification, due to non-equilibrium effects. Indeed, while cooling, segregation of titanium can lead to the formation of richer liquid clusters, which may finally solidify as Ti_2Ni precipitates located at grain boundaries. Moreover, the precipitation of this brittle intermetallic phase may severely impair mechanical and shape memory properties of the alloy, as they act as crack initiation sites [20]. As this is a peritectic reaction ($\mathrm{TiNi} + \mathrm{Liquid} \rightarrow \mathrm{Ti_2Ni}$), it is limited by diffusion of species in the primary solid phase and thus, is very slow and the remaining liquid can even reach the eutectic composition to form ($\beta - \mathrm{Ti}$), which has a solubility of almost 10%at. Ni [21]. This last step was observed by Lopez *et al.* in large precipitates with two different compositions. These precipitates also act as preferential nucleation sites for the martensite transformation [22, 23].

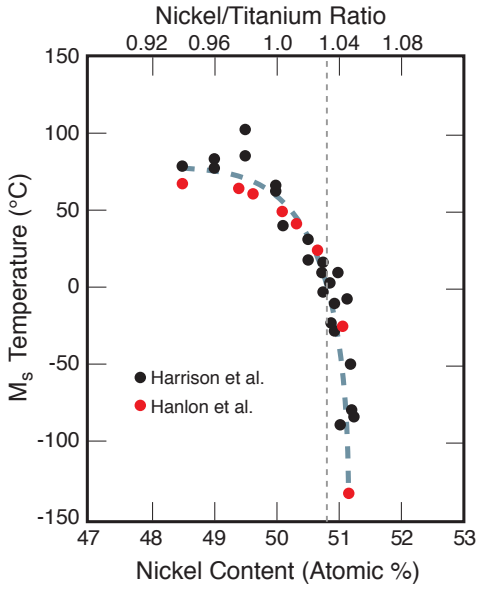

(a) Transition temperature related to nickel content of the alloy [17] (dashed line: composition used in the present study).

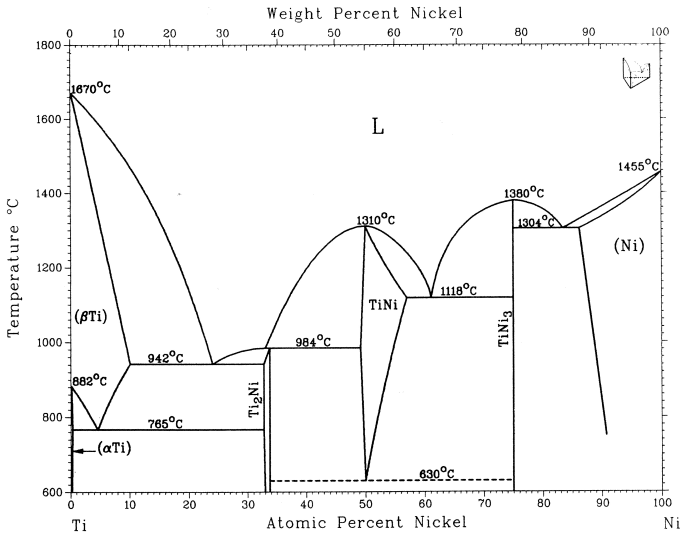

(b) Nickel-Titanium binary phase diagram showing the different stability domains of intermetallic phases [18].

Figure 2.3: Matensite transformation temperature and phase diagram corresponding to atomic concentration of nickel in binary NiTi alloys.

Nickel-rich NiTi part of the phase diagram is better known than the previous one and the variation of the martensitic transformation temperature with nickel is larger (see Fig. 2.3a). Compared to the titanium-rich side of the NiTi intermetallic, this side shows a wider solubility domain and the solidification path ends directly with a eutectic reaction at 1118 °C, which imposes the final microstructure to have a maximum of two phases (NiTi and Ni_3Ti). However, two metastable precipitation phases were observed by Nishida *et al.* in 1986: $Ti_{11}Ni_{14}$ and Ti_2Ni_3 [24]. These intermetallic precipitates are coherent with the matrix and have lenticular shapes [25]. This leads to stress fields in their neighbourhood, which induces a change in martensite transition temperature and preferential nucleation areas [26, 27].

2.1.2 Other Binary Systems

In this study, the materials choice is very limited, as biocompatibility is required for the production of medical components. Thus, Stainless Steel (SS) is a base material for the welding process in invasive surgery tools. So it is essential to understand the influence of each element on the base alloys and between each other. The interactions between nickel and titanium and the exceptional properties of such alloys were presented above (see Sect. 2.1.1). This section will focus on the other possible binary interactions between SS and titanium element.

The first concerned elements are nickel and chromium as they are the most concentrated elements in stainless steel (after iron of course). Iron and nickel have a strong affinity between each other, which is similar for iron and chromium, as they show a complete miscibility into each other (see Fig. 2.4). But a noticeable difference between chromium and nickel is their influence on the stable phase formed when alloying with

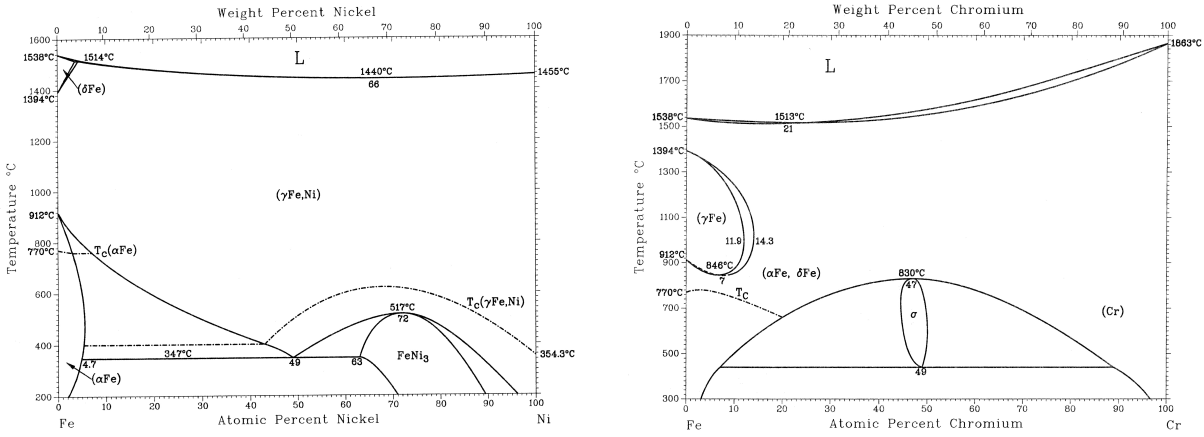

(a) Iron and nickel. **(b)** Iron and chromium.

Figure 2.4: Binary phase diagrams of major stainless steel alloying elements with iron, according to the ASM handbook [18].

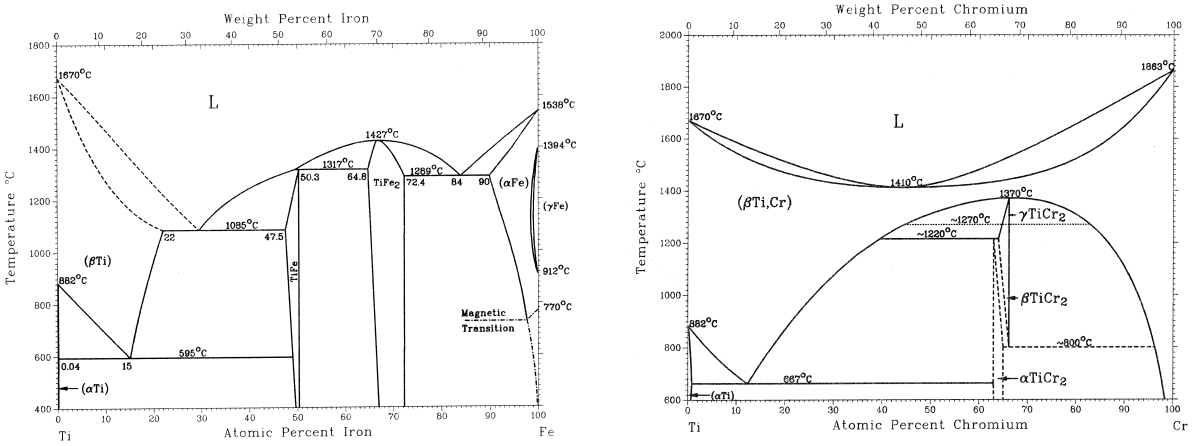

(a) Iron and titanium **(b)** Chromium and titanium

Figure 2.5: Titanium binary phase diagram with major interacting elements, according to the ASM handbook [18].

iron. Chromium enhances the stability of the ferrite (α-Fe), which has a body-centred cubic (BCC) structure, and nickel increases the stability of the face-centred cubic (FCC) austenite (γ-Fe) of iron.

Another binary phase diagram to be considered in this study is the one describing the interactions between iron and titanium (see Fig. 2.5a), because both elements, highly concentrated in the base materials, will interact during welding.

Likewise chromium, titanium acts as a ferrite phase stabilizer, but does not show a complete miscibility with iron. Indeed, two intermetallic phases (TiFe and $TiFe_2$) are observed over a wide range of temperature. Both chromium and titanium are expected to react similarly as their binary phase diagram shows comparable brittle intermetallic phase (σ - CrFe or FeTi, see Fig. 2.4b and Fig. 2.5a).

Moreover, several works have mentioned and analysed the possible formation of these brittle phases during dissimilar laser welding [28, 29], especially between titanium and iron [30, 31]. This intermetallic formation has to be avoided to increase the mechanical

properties of welded areas.

2.1.3 Iron-Nickel-Titanium

Combining NiTi and SS leads to a mixing of several elements, but for the sake of simplicity, this section focuses on the ternary system Ni-Ti-Fe. The influence of chromium is neglected as it is less concentrated than the other elements (Fe, Ni, Ti). Moreover, as seen above, chromium can be assimilated to titanium in the quantification process as it has a similar influence on the phase formation since it is, like titanium, a BCC-stabilizer for iron-base alloys [32]. General consideration about ternary phase diagrams will first be discussed and then applied to the studied Ni-Ti-Fe ternary system.

Ternary phase diagrams are a powerful tool to predict or at least understand microstructures knowing the nominal alloy concentration of each three elements. If binary phase diagrams can be easily represented in two dimensions, three are required to plot ternary phase diagram exhaustively. More accurately, a phase diagram with N_C elements requires $(N_C-1)+2$ dimensions. Indeed, there are two independent variables, the pressure and the temperature, and there is one condition that the sum of the molar concentrations equals 1. The pressure is often fixed at 1×10^5 Pa in the phase diagrams available in literature.

In such a multicomponent system, the number of degrees of freedom (N_F) is given by *Gibbs' phase rule*:

$$N_F = N_\phi - N_C + 2 \tag{2.2}$$

where N_ϕ is the number of co-existing phases. This rule governs the diffusion paths theory, for instance in a ternary phase diagram ($N_C = 3$), three phases ($N_\phi = 3$) can only coexist with two degrees of freedom (temperature and pressure). However, as the pressure is usually fixed, three phases are stable with only one free variable (temperature). The latter, so-called *monovariant* line, degenerates into a single point at fixed temperature (2D isothermal cuts). And by similar argument, four phases are only present at fixed compositions and temperature (*e.g.*, ternary eutectic point).

Based on this rule, Kirkaldy and Brown established the basis of diffusion behaviour in multiphase diagrams, the so-called *virtual path*, for the prediction of diffusion paths according to thermodynamic minimization of entropy [33]. This theory was described by several theorems (or *rules*) that must be followed during diffusion path prediction, like mass balance for instance, either in single or multiple phase regions. Clark defined conventions for representing ternary diffusion paths and predictions for microstructures at equilibrium state [34]. These two works allow to represent diffusion paths according to microstructures in diffusion couples (see Fig. 2.6). This solid-state diffusion theory in ternary system was further investigated by van Loo, in 1990 [35].

As ternary phase diagrams are difficult to handle using only two dimensions, several views are usually represented. Classically, ternary phase diagrams are composed of isothermal cuts at selected temperatures, represented in an equilateral triangle with pure elements at its corners. Another important information about a ternary system is the *liquidus projection* of the phase diagram, which is a top-view of the liquidus surface associated with all solid phases projected over the Gibbs simplex (see Fig. 2.7a). On this liquidus projection diagram, the isotherms are presented as dashed lines and arrows of the monovarient lines indicates the composition path followed by the liquid among solidification *binary crystallization curve* [36].

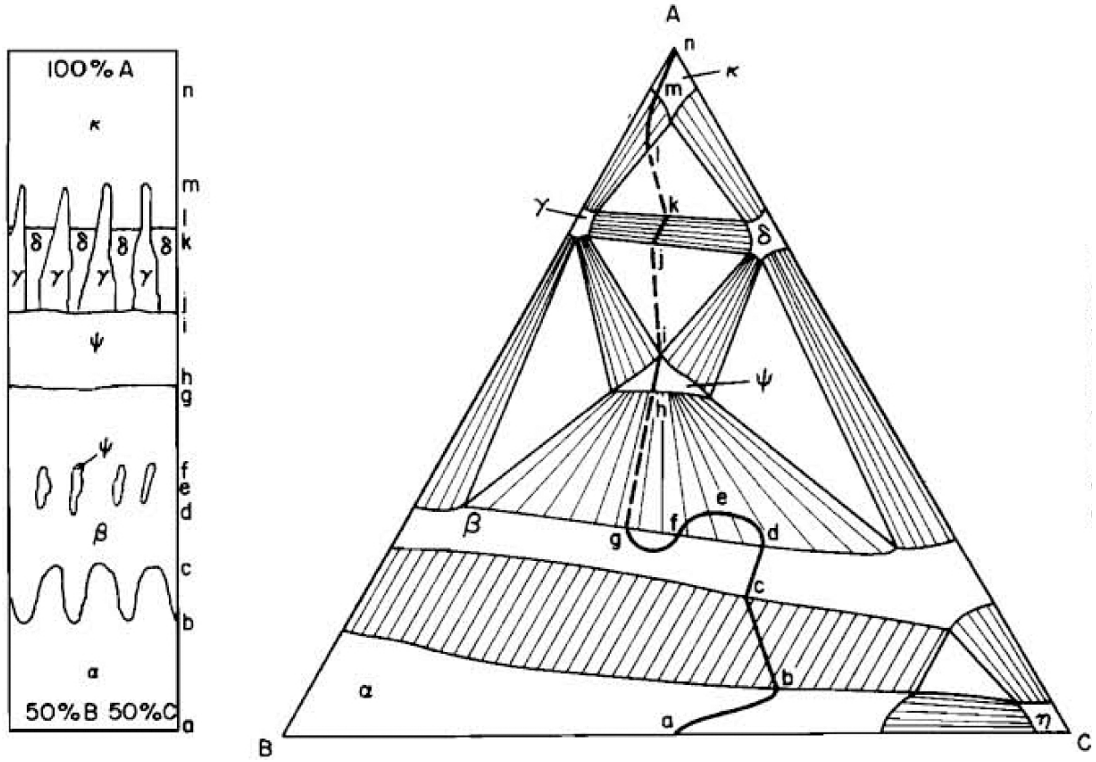

Figure 2.6: Microstructures (left) can be linked to diffusion paths on the corresponding isothermal cut (right). The path has to be continuous and can cross every region, but the three phase region have to be degenerated to a single boundary (see microstructures transition between points i and j). Similarly, the binary regions have to be crossed following the tie-lines, otherwise a phase fraction sequence appears (see the difference between area $d-e-f$ and $g-h$). In the present exemple, pure A would be welded (diffusion couple) with a material made of 50% B-50% C. [34]

Isothermal cuts allow to determine which phase will nucleate and grow when dealing with different concentrations, as in the case of joining dissimilar materials. However, the isothermal cuts as well as the phase diagrams are valid at equilibrium, *i.e.*, they are only valid for very long diffusion time at fixed temperature. On figure 2.6, the diffusion path is represented either by continuous or dashed lines. The dashed lines are instantaneous paths, which means both path ends correspond in the microstructure. Indeed, as only one phase can sustain three freedom variables (at fixed pressure) and thus, the compositions in binary domains have to be split in tie-line extremes compositions (see case $g-h$). The continuous line between points $d-e-f$ is explained by the concentration change outside tie-lines. The latter implies a phases fraction variation as in the $b-c$ segment (and a variation in the composition of the considered phases). However, three phase domains cannot be crossed continuously and have to be split at precise place in microstructure (see segments $i-j$ or $k-l$) [34].

The ternary iron-nickel-titanium system was investigated widely to gather the information about its phase diagram. A first extensive review of this system was done by Gupta in 1990 [37], and regroups two pseudobinary phase diagrams (vertical cuts through the ternary phase diagram). The first pseudobinary, established in 1938 by Vogel and Wallbaum, emphasized the presence of a eutectic point between the two intermetallic coumpounds $Ni_3Ti - Fe_2Ti$ with quite high saturation concentrations [38]. The second one,

studied by Dudkina and Kornilov, enhances the complete miscibility of the $(Fe - Ni)Ti$ intermetallic phase [39]. Both emphasize the high affinity between nickel and iron previously referred in subsection 2.1.2. Another important parameter of strong affinity is the possibility to keep shape memory properties when increasing iron content with a constant titanium concentration over a wide range of temperature [40, 41, 42, 43, 37].

Gupta also established the liquidus projection of the system, and referred several isothermal cuts at different temperatures, followed by Cacciamani *et al.* and Ghosh in 2006 [43, 47], for several isothermal cuts (see Fig. 2.7). These works can help predicting microstructure formation and nucleating phases during solidification. As an illustration, an alloy with the nominal composition of $Fe_{50}Ti_{25}Ni_{25}$ will first form $TiFe_2$ dendrites followed by a coupled growth of $TiFe_2$ and γ, when hitting the U_1E_1 monovariant line (see Fig. 2.7a). The remaining liquid will solidify when reaching the E_1 composition at its ternary eutectic temperature (see subsection 2.2.6 for more details).

Moreover, several studies were published on new phases formation in this system and its associated thermodynamical properties [48, 42, 49, 50, 43]. Wang [48] identified the brittle intermetallic (TiFe and $TiFe_2$) to be the common problem for sound joints between NiTi and SS (either with direct fusion welding or solid-state diffusion process, as encountered by Hinotani [51]). He used a metallic interlayer to avoid the formation of these intermetallic compounds encountered in the NiTi-SS system. Van Loo *et al.* studied the phase relations and the diffusion in the Ni-Ti-Fe ternary phase diagram, especially at 900 °C [42]. Afterwards, Efimenko *et al.*made similar studies at the temperature of 1200 °C in the Ni-Ti-Fe equilibrium [49]. Riani *et al.* reviewed thermodynamical modelling and experimental data and suggested new experimental investigations [50].

Lately, Cacciamani and de Keyser published an exhaustive review of the Fe-Ni-Ti ternary phase diagram [43] and Calphad computation to assess their evaluation of the data [44]. The actual state of the art about this ternary phase diagram contains several isothermal cuts (900 °C, 1000 °C, 1200 °C, computation of 1300 °C, liquidus projection), several pseudo-binary phase diagrams and the well known binary phase diagrams. These results were evaluated and summarized by Raghavan in 2010 [52].

2.2 Laser welding

A laser (acronym for *Light Amplification by Stimulated Emission of Radiation*) is a device that emits light with a high degree of spatial coherence and a precisely defined energy. Contrariwise to a classical thermal or other incoherent light sources, the laser beam consists in a monochromatic wave with a homogeneous polarization. So, the laser beam can either be kept in a parallel beam to transmit light, or focussed to a very tiny spot with high energy density. The foundations of Laser theory (stimulated emissions) were developed in 1917 by Albert Einstein [53].

Every laser is made of a *gain medium* that is surrounded by a highly reflective cavity to keep the light beam confined. This cavity is typically closed by mirrors, with one of them partially transparent to let part of the beam escape. By this mean, the light is going many times through the gain medium and is stimulated by an external energy pumping unit, like a flash lamp. So the gain medium transfers the light pumping energy to the confined beam, with a homogeneous phase and wavelength, before it escapes after many back and forth paths, defining a precise energy and unique beam energy.

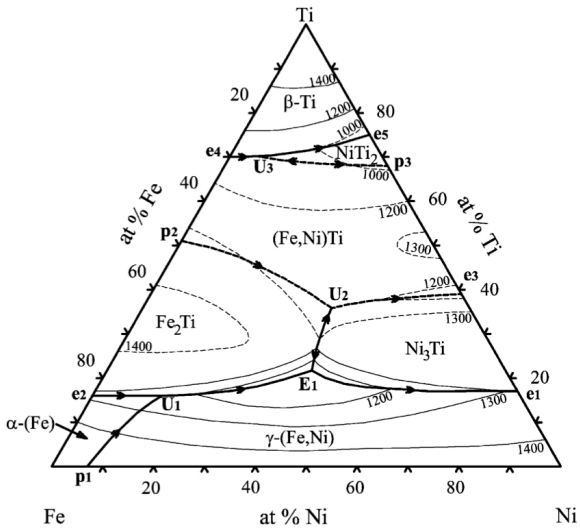

(a) Liquidus projection established by Cacciamani [43].

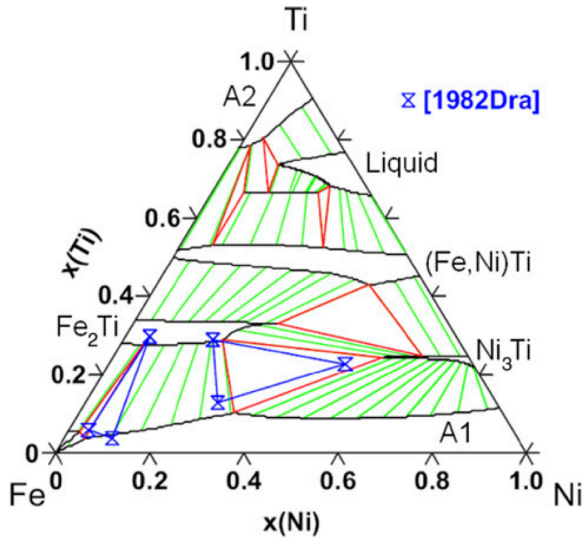

(b) Computation of an isothermal cut at 1300 °C by De Keyzer*et al.* [44].

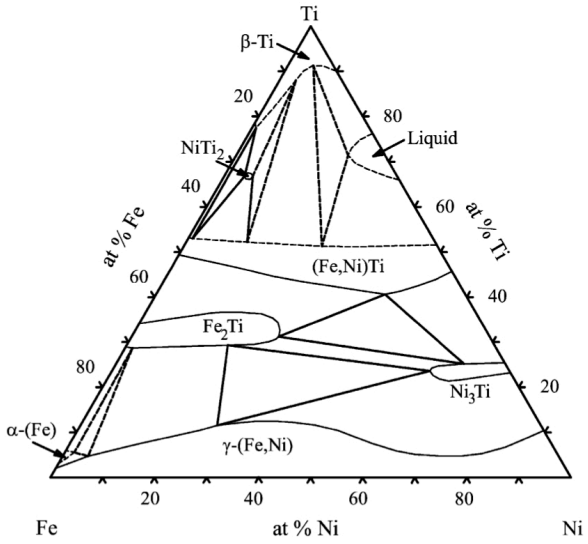

(c) Isothermal cut at 1000 °C by Abramycheva*et al.* [45].

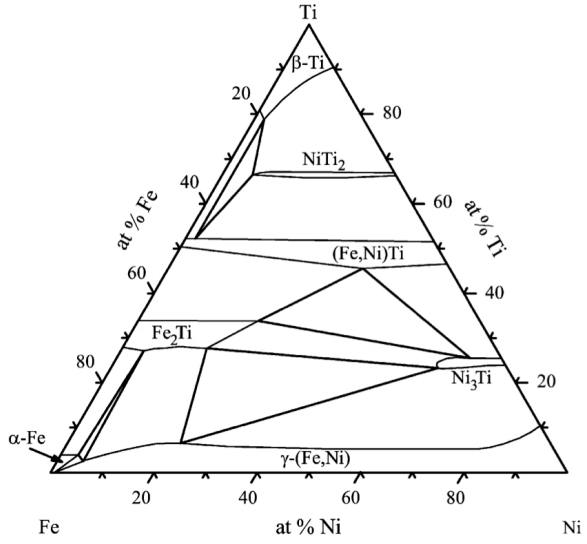

(d) Isothermal cut at 900 °C by Van Loo [42].

Figure 2.7: Liquidus projection of ternary Fe-Ni-Ti phase diagram and three assessed isothermal cuts at high temperature. This diagram is a good approximation of the studied NiTi-SS system, with omission of chromium and low alloying elements of SS. The 1300 °C isothermal cuts is a computation compared to experimental data of rich iron corner of the phase diagram [46].

2.2.1 Laser sources

Laser beam energy has a very narrow dispersion spectrum. Thus, to cover a wide range of applications and materials, there is a need to have a wide choice in wavelength, as the reflectivity of materials varies with wavelength. Several types of gain media are also available, from different solid state lasers to gas lasers:

Solid-state lasers are usually made of a crystalline rod with good thermal and optical properties, which is doped with an element: *the dopant*. These lasers are pumped optically using a shorter wavelength than the lasing wavelength, often from a flash lamp or from another laser. Fiber lasers are often put in another category as they are not strictly composed of a laser rod gain material. Neodymium is a common dopant in various solid-state laser crystals, including yttrium orthovanadate (Nd:YVO_4), yttrium lithium fluoride (Nd:YLF) and yttrium aluminium garnet (Nd:YAG), the latter being the most widely used. All these lasers can produce high power in the infrared spectrum at 1064 nm. They are used for cutting, welding and marking of metals and other materials, as well as in spectroscopy and for pumping dye lasers. The laser frequency can be multiplied to reduce the wavelength by the same amount, when using higher order harmonics, in order to change their range of applications.

Fibre lasers work with a similar principle as solid-state lasers but an optical fibre is used as the laser gain medium, also generally doped with rare-earth elements. However, the high surface ratio of the optical fibre allows a better cooling and thus less thermal strain. These thermal changes have to be minimized to reduce geometry changes of the lasing medium and optimize the beam quality. These lasers are commonly pumped using diode lasers directly guided through the optic fibre. The reflector is made of a succession of layers with a slight refraction index change (*Bragg grating*). Thus, only one specific wavelength is reflected and used for pumping. These lasers are either used in a continuous wave mode or the beam can be chopped to produce a pulsed beam [54].

Gas lasers are made of a gaseous gain materials, such as CO_2 or HeNe. The presence of gas makes the heat extraction easier and the active material can be in high volume with low costs. Moreover, the gain medium cannot be damaged by radiations or thermal strains. Some gas lasers are powered by chemical reactions (*chemical lasers*) or by the use of molecules composed of two species, one being in the excited state (excited dimer = *Excimer*).

Other type lasers can either be based on semiconductors (*diode lasers*) or organic dye (*dye lasers*) as gain medium (several other materials can be used as gain materials).

Basically all laser types are based on the same pumping technique and the main difference stands in the material used as gain medium, and therefore their wavelength and accessible power range.

2.2.2 Working mode

Laser beam are usually working in a *continuous mode*, *i.e.*, the intensity of the exiting beam is constant over time. However, several devices work in *pulsed* mode to reach enough energy density over a fixed duration, as required for drilling, cutting and several

other laser processes. Even if some lasers produce only a pulsed signal, due to their pumping method (*flash lamps*), continuous lasers can be used in pulsed mode using various switching methods to produce desired length pulses [54].

Continuous wave and pulsed lasers can be programmed to fit several application domains, but one parameter is intrinsic to the used lasers, that is the wavelength of the emitted beam, depending on the gain medium. Thus, the absorption of the different targets has to be evaluated previously to avoid a complete reflection of the incident radiation. The other parameters can be varied in a range of values determined by the type of lasers, some of them being specific to pulsed lasers:

Power is the most important characteristic of a laser beam, as condensing power is the key concept of laser radiation. When dealing with continuous lasers, the power is governed by the volume of the gain medium, its efficiency and the input power of the pumping unit. It can vary from a few milliwatts when considering laser pointers or CD-ROM reading units, to hundred of kilowatts in recent military devices. In the case of pulsed lasers, the power can be much higher as the same energy is delivered over a very short duration, so the mean power (P_m) stays constant but the Pulse Peak Power (PPP) is higher: $PPP = \frac{T \cdot P_m}{t_p}$, where t_p is the pulse duration and T the period between each pulse ($T = \frac{1}{f}$, where f is the frequency of pulses, see Fig. 2.8).

Pulse duration is obviously a parameter reserved for the pulsed mode as it defines the duration of each pulse. However it can be extended to continuous wave in some cases, when fixed duration is required, as for wire welding (finite bead length). The pulse duration can vary over several orders of magnitude and is an important parameter as it defines the pulse peak power with the frequency. Indeed, femtoseconds pulses are used in ablation or micromachining [55], and no upper limit exists as continuous wave lasers can handle all durations.

Frequency of pulses is also a parameter confined to pulsed mode. It determines the pulse peak power according to the mean power and the pulse duration (see Fig. 2.8). The frequency corresponds to the inverse of the period, which is the elapsed time between every pulse ignition.

Focal diameter can be changed using different lenses, in order to achieve higher surface power density. Indeed, simple heating applications require large focal diameters to avoid damaging surfaces, but drilling and cutting are examples of high surface energy density applications.

Overlapping is a parameter restricted to pulse mode as it corresponds to the percentage of the current pulse surface covering the previous pulse one.

Transverse velocity is the velocity at which a continuous or pulsed laser is moved over the surface of the material.

Several other parameters may be tuned according to needs for several applications. In the scope of laser welding, a gas shielding is commonly used to avoid oxidation and guarantee a good cooling of the welded areas. Usually noble gases, such as argon, with high purity, are used with a low flux to reduce turbulence and ambient atmosphere intermixing.

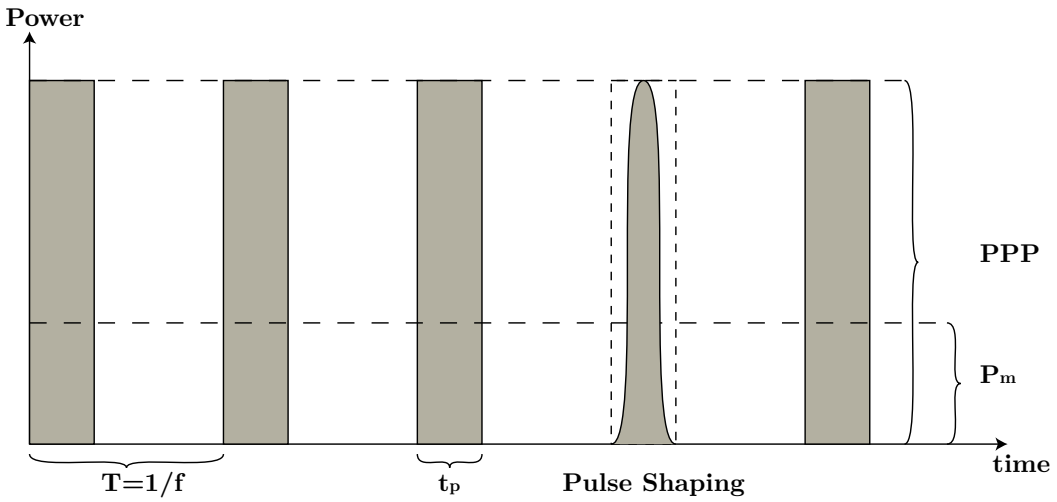

Figure 2.8: Specific pulsed laser mode parameters: the period (T) is the inverse of the pulse repetition frequency (f), the pulse peak power (PPP) is equal to the mean power divided by the frequency and pulse duration (t_P).

2.2.3 Welding configurations

As mentioned above, laser absorption is defined by the incident wavelength and is highly dependent on the target material (see Fig. 2.9a). Several parameters can influence the absorption of the energy by the materials, such as the local temperature, incident angle, surface roughness, formation of a plasma due to materials evaporation, etc.... In the case of laser welding, the absorbed energy needs to be as high as possible to reach the melting point of the metal. Nevertheless, a special care has to be taken when aiming to dissimilar welding, as one of the metals can absorb well the incident energy but not the other. This special case is well illustrated by the research made by Denis Favez on steel-gold dissimilar welds [56].

The absorption coefficient is governed by physical parameters of the material and welding positioning, such as the *refraction index* and the *state* of the target material, the *incident angle* of the beam and its *polarization* [57, 58, 59]. The surface roughness is equivalent to a variation of the incident angle, with a minima for the mirror polished surfaces. Various modifications of the welding device can modify these absorption parameters:

Wavelength can be adjusted to maximize the absorption of the incident energy. The choice of the laser gain medium is crucial as it is the electronic bandwidth of the concerned element that defines the wavelength. However, adequate wavelength lasers may not satisfy pulse duration or power prerequisite of the welding process. But Nd:YAG lasers have another wavelength modulation possibility, which is the frequency multiplying. The frequency multiplying is done using a non-linear optical process, where incident photons on selected non-linear optical materials interact to generate photons with higher energy (shorter wavelength) [61].

Incident angle is also known to change the absorption coefficient as in the case of polarization (see Fig. 2.9a) [60]. However, the sensitivity to the incidence angle is difficult to handle as for the polarization during laser welding, due to the surface quality consisting of several variations of the surface orientation. Most of the time, the beam is perpendicular to the surface to reduce the spot size and increase the

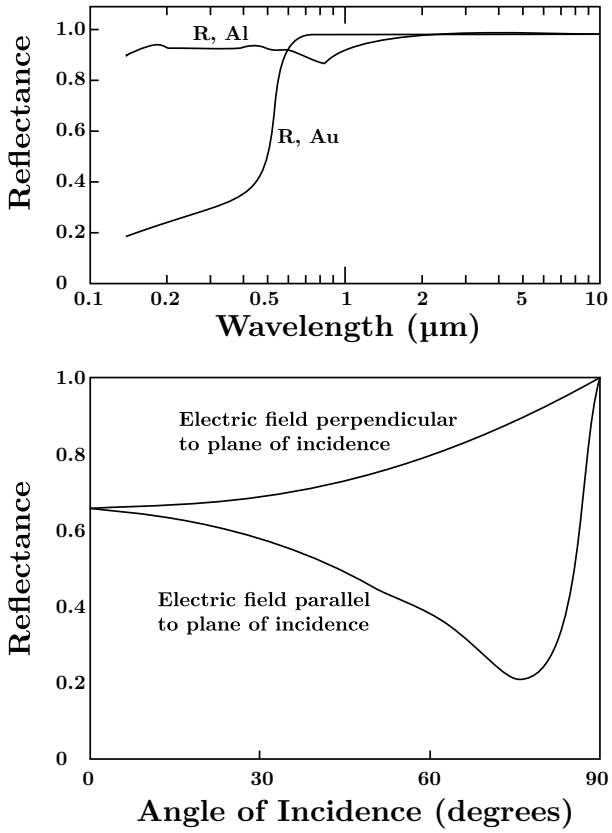

(a) Absorption variation between materials as a function of laser wavelength (top: gold and aluminium) and as a function of incidence angle (bottom: SS).

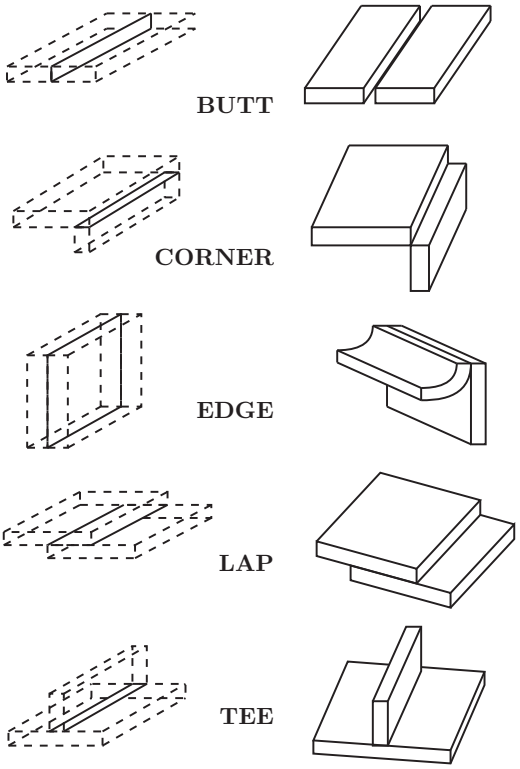

(b) Different joining positions (from top to bottom: Butt, Corner, Edge, Lap and Tee).

Figure 2.9: Influence of materials or incidence angle on laser absorption (a) and different joining configurations (b) [60].

energy density. However, as some reflection occurs, a small misorientation is applied to avoid laser lens damaging.

State of the materials is important as much more energy is absorbed when increasing the temperature near its melting point [62, 60]. Moreover, the presence of a small liquid film leads to a change in absorbed energy. A technique, called *pulse shaping*, is usually used to initiate melting at the surface, and then the power is lowered to obtain a steady absorbed energy. As this control is difficult due to the sensitivity of the parameters, coupling was developed to control the laser power according to the metal temperature during each pulse. However, this requires high reactivity switching and efficient control devices, but was successfully applied on spot welding [63, 64]. Moreover, in the vapour phase the material absorbs more energy than in the liquid state. This leads to a keyhole mode with a high penetration of the beam inside the target material and to a deep weld. Such a mode is used in drilling and cutting if the total thickness is molten and matter is removed by blown gas for instance. Formation of a plasma in the vapour phase state is even more efficient for matter removal and laser absorption.

Welding configurations may change absorption issues, as welding in corner or lap con-

figurations (see Fig. 2.9b) avoids multiple absorption coefficient, the laser energy being transferred to only one of the components. Welding superimposed sheets makes the laser beam interact with only the upper material, the energy being transferred to the bottom one by convection and conduction once the top material thickness is molten. However, most of the configurations are determined by the final product application and choice in the weld configuration is difficult to manage. Nevertheless, another aspect of the configurations can be tuned, in the case of dissimilar welding, the *dilution factor*. It corresponds to the laser beam exposed ratio of each material. For instance, in butt weld configuration (see Fig. 2.9b), the selective positioning of the laser beam on one material will make it melt and transfer the energy to the other one without laser absorption limitation for the second. Moreover, this parameter influences the final composition of the welded area and may be chosen to avoid undesired phase formation [65].

2.2.4 Laser welding modes

During laser welding, two different ways of transferring energy from laser beam to weld area coexist, depending on the power density: *conduction* and *keyhole* modes. At low energy density, which is proportional to the input power and inverse to the spot size, heat transfer is done to the outer surface of the material. The heat is then conducted inside by the molten surface metal by conduction and convection (see Fig. 2.10, left side). Conduction mode welding is characterized by a weld spot cross section having a bowl shape, with a relatively low penetration depth, comparable to the weld diameter. The weld diameter usually spreads out to a bigger size due to Marangoni convection, which tends to drive the hot metals toward the outer part of the spot (see subsection 2.2.5).

Contrariwise, keyhole welding mode is reached with higher energy density laser spots and thus lower spot diameter and higher power. In this mode, the molten metal is locally vaporized to form a plasma, which absorbs more energy. This cavity remains open by the vapour pressure ejecting the matter by the entrance hole (see Fig. 2.10, right side). Moreover, the hole wall acts as a reflecting plane focusing the beam deeper inside the molten area. The final bead width is usually smaller than in conduction mode as the heat is driven deeper in the matter. At high energy, a plasma plume can form at the top of the keyhole canal and temporary shade the laser beam, leading to oscillations in the welding depth. All cutting and drilling processes are made in keyhole mode, where matter is ejected by a gas flow or simply due to the vapour pressure increase inside the canal. The transition between conduction and keyhole mode is a key aspect of laser welding as explained by Lee *et al.* [67].

2.2.5 Marangoni convection

During laser welding, the surface tension of the free liquid surface, γ_{lg}, has a strong effect on liquid motion in the molten pool. The energy distribution of the laser beam leading to a higher temperature near the center of the laser spot, a thermal gradient appears radially at the surface of the molten zone. The surface tension depending on temperature, a driving force appears at the surface of the bath, leading to its displacement. If the increase in temperature lowers the surface tension, the driving force will lead the center and warmer liquid to flow in direction to the weld perimeter, inducing a thermal *Marangoni* convection. This results in a broadening of the molten area due to heat transfer by convection toward

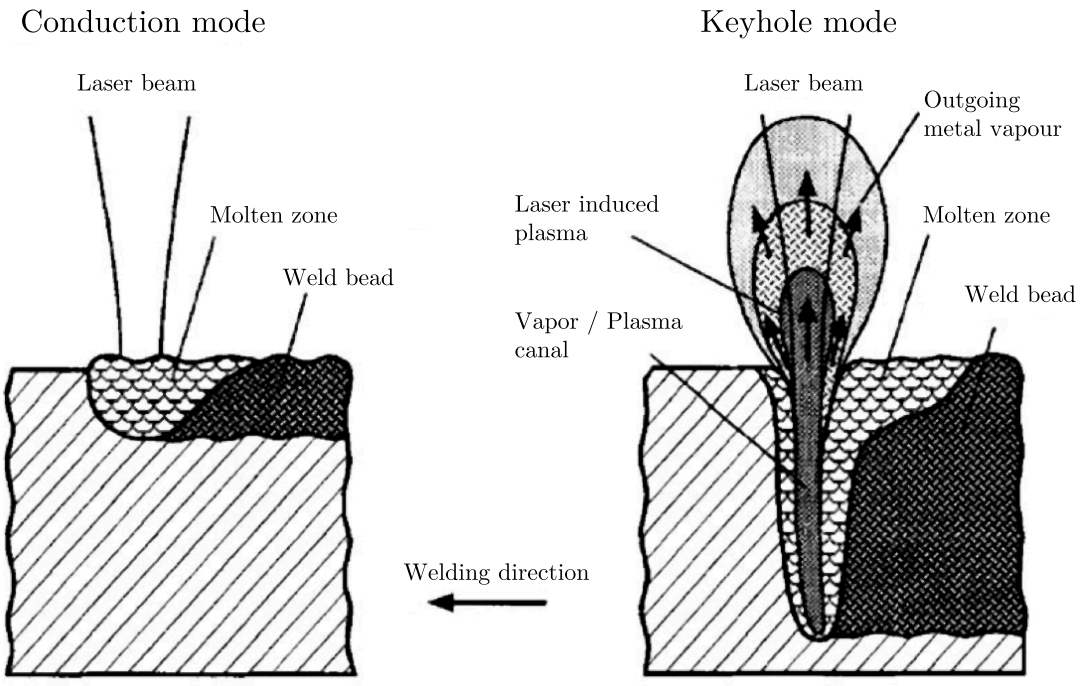

Figure 2.10: Principle of laser melting, cross view of the two different melting modes: (left) conduction mode, (right) keyhole mode. The penetration depth is higher in keyhole mode as the absorption increases due to the formation of a plasma and the beam is focused down the canal by complete reflection on its wall [66].

the outer part of the weld (see Fig. 2.11). An inverse effect is possible for materials having an increase in their surface tension with temperature. Some trace elements, such as sulphur in the case of steel, may have a huge influence on this parameter [68].

Likewise thermal gradient effect, a *chemical Marangoni convection* is possible when a species concentration gradient arises at the surface of a liquid pool, which is precisely the case of dissimilar laser welding. In fact, if a metal has a smaller surface tension, it will be pulled toward the higher surface tension metal part of the pool. A perfect illustration is the dissimilar welding of gold and stainless steel, where the gold is driven to the side of stainless steel and leads to huge convection during solidification [56].

In the case of NiTi and SS, similar values of surfaces tension near their respective melting point cause the NiTi to have the lowest value at the same temperature.

2.2.6 Solidification

After energy is transferred to the metal and the molten state is reached, cooling and solidification occur when the laser beam energy input is interrupted in pulsed mode or when the laser beam moves along the piece in continuous mode (see Fig. 2.10). As mentioned above (see subsection 2.1.3), solidification in multiphase alloys can lead to quite complex microstructures for various reasons: microsegragation at the local scale, composition inhomogeneities of the melt when dissimilar materials are welded, variable cooling conditions, etc... Moreover, laser welding typically implies very fast solidification speed (isotherm velocity), up to $1 \times 10^3\,\mathrm{m\,s^{-1}}$ in extreme cases [60]. And fast solidification rates usually encountered in welding can lead to several non-equilibrium effects: solute gradient in the solid and in the liquid, very fine structures for which curvature becomes important,

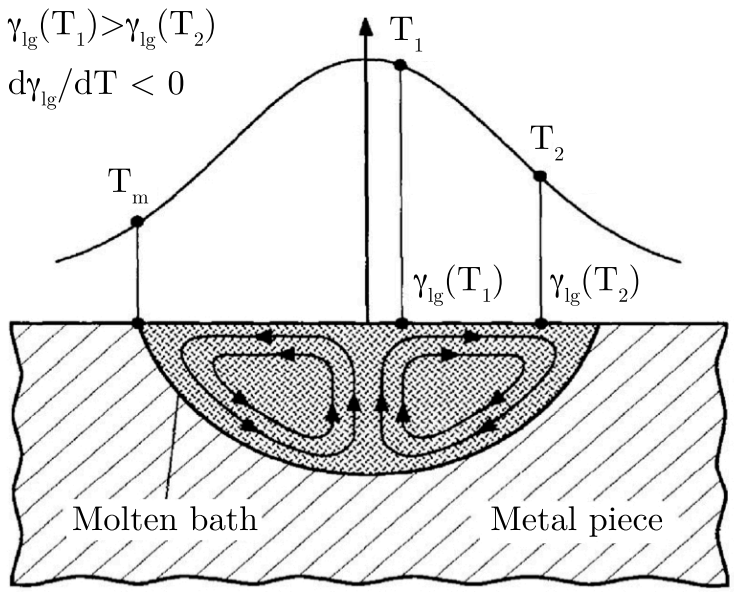

Figure 2.11: Marangoni thermal convection is induced by liquid-gaz surface tension (γ_{lg}) variations with temperature. A negative gradient ($\frac{d\gamma_{lg}}{dT} < 0$) leads to a broadening of the weld bead as the surface tension is lower in the center of the joint due to a higher temperature. [66]

attachment kinetics effects, solute trapping, metastable phase formation, etc... [36]

Microsegreagation is expected during solidification of multiple phase microstructures. Even if the melt has a uniform composition, the low Fourier[2] of the solid leads to a deviation from the lever rule. In other words, the solid composition is not uniform in the solid microstructure. This microsegragation can be significant even at the scale of primary and secondary dendrite arm spacings.

Composition inhomogeneities are of course important when dealing with dissimilar welding. Marangoni convection tends to unify the molten pool concentrations, but the proximity with the original unmolten materials, combined to the short interaction time, leads to inhomogeneities in the weld pool. The longer the interaction, the smaller the inhomogeneities, but the weld-base wire interface concentrations differs from one side to the other.

Variable cooling conditions are present during laser welding. For instance, at the end of a laser pulse (or at the bottom of the pool in the case of continuous laser welding), the isotherm speed is null and increases rapidly as solidification starts when heat is extracted (or the beam moved away). This may lead to a transition from planar front to columnar and finally equiaxed microstructures (see Fig. 2.12b).

Dendrite tip or eutectic kinetics could also vary a lot in laser welding. The beginning of solidification does not start at the liquidus temperature (T_{liq}), but an undercooling ($\Delta T(v)$) is required to form the solid phase, either dendrite or eutectic (see Fig. 2.12a). The higher the solidification speed, the higher the undercooling.

[2]The Fourier number ($Fo = \frac{D \cdot t}{L^2}$, where D is the diffusivity, t the characteristic time scale and L the length scale of interest) defines whether diffusion is important ($Fo \gg 1$) or not ($Fo \ll 1$).

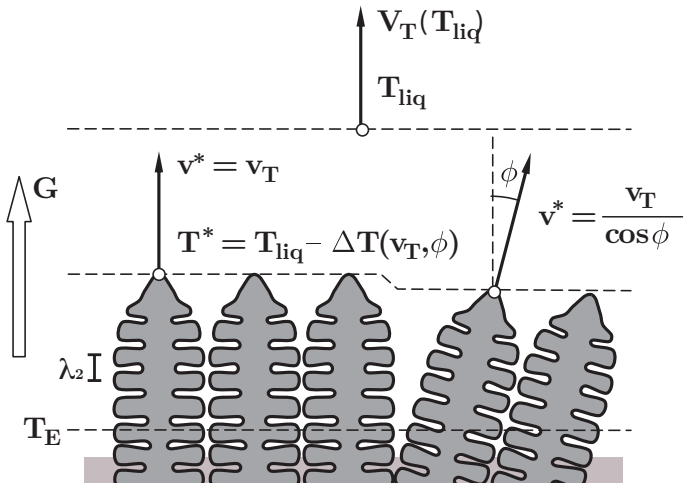

(a) The dendrite tips are behind the actual liquidus temperature as an undercooling is required as a driving force for solidification. In addition, dendrites are forced to grow in specific crystalline directions, but isotherm change continuously, which leads to growth competition. Eutectic phases are not constrained to grow along specific direction and their undercooling depends only on velocity.

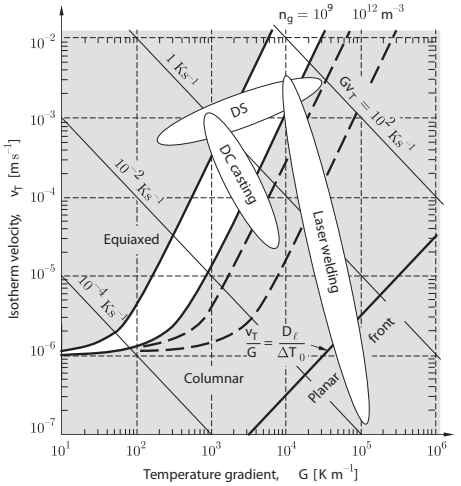

(b) Laser welding implies high temperature gradients, but isotherm velocity that may vary widely according to the location. At the start of solidification, the isotherm velocity is almost null, but increases rapidly to reach high value at the end.

Figure 2.12: During solidification, isothermal speed defines the solid growth speed, which can vary over several orders of magnitude in the case of laser welding [36].

Curvature affects the undercooling, even if the main contribution to the dendrite tip undercooling is solute diffusion. But when the velocity increases, the radius of the tip decreases and capillarity plays an increasing role. At very high speed, even absolute stability can be reached, when no more dendrites form and a new planar front develops.

Attachment kinetics is usually not important for metals, but can be important for intermetallic phases. In the latter phases, the interface velocity depends also on the growing crystal orientation, some crystalline directions having a faster growing speed.

Solute trapping may interfere in solid phase formation as the interface velocity increases. The solute elements cannot be rejected in front of the solidification interface and are trapped in the solidified structure, leading to non-equilibrium compositions in the solid phase.

Metastable phase formation is possible, especially at high solidification speed, when nucleation and growth can be affected. Metastable phases (that were not predicted by the equilibrium phase diagram) can nucleate if their composition and kinetics are well adapted to the solidification conditions.

2.2.7 Porosity and hot cracking

As previously mentioned, multiphase solidification associated with welding induces several inhomogeneities such as microsegregation, phase formation, composition gradients. Moreover, solid phases having usually a higher density than the liquid, porosity may

be observed during solidification. Indeed, final solidification happens between dendrites trunks and arms and liquid feeding associated with solidification shrinkage induces a pressure drop in this high solid-fraction region. If there is a lack of feeding, shrinkage porosity with complex shapes might form. Pores are highly pinched between the solid microstructure and have high curvature, which increases stress intensity factor in these regions, like around crack tips.

These complex shape shrinkage porosities may appear in continuous laser welding as the interaction time is longer, compared to pulsed laser welding. Indeed, the shrinkage porosity tendency is inversely proportional to the ratio of the thermal gradient over the speed of the isotherms. The longer the interaction time, the lower the thermal gradient, while the isotherm speed is similar in both techniques. Porosity may also remain in keyhole laser welded beads resulting from plasma or metal vapour trapped during solidification. These voids are larger and have spherical shape as they form before the solid network develops, but they are randomly spaced in welded microstructures [69].

Furthermore, *hot cracking* is an issue in laser welding. During growth, dendrite structures follow the thermal gradient and thus are nearly perpendicular to the isotherms during cooling. When the beam is driven in a single direction, these isotherms change along time to end up aligned with the traverse direction of the laser. Thus, final solidification ends up in the middle of the bead and is highly sensitive to void formation, leading to a weakening of the structure against shrinkage, which tends to open any nucleated voids. This may lead to a continuous crack propagation along the weld centerline and tremendously reduces the welded joint mechanical properties [70].

2.2.8 NiTi-SS dissimilar welding

Laser welding is a well-known method for autogenous metallic materials welding. NiTi has been successfully welded using pulsed laser technique [71, 72, 73, 74, 31]. Continuous laser welding was also used to join NiTi to itself [75, 76]. Similar direct welding processes were applied to NiTi autogenous joining, such as resistance welding, which was the first successful solution [77, 78]. Tungsten Inert Gaz (TIG) welding was used to join sheets and wires of NiTi by Kimura and Tobushi [79, 80], while friction welding of cylindrical bars was made by Shinoda [81]. A patent was claimed in 1995 by Masunaga about joining NiTi to other metals using a heating and forging process at the solid state. The slow diffusion of species in the solid reduces the brittle intermetallic layer thickness. Nevertheless, the Heat Affected Zone (HAZ) had no more SM properties due to composition changes, which was an issue for several applications [82].

Moreover, complementary techniques were widely used, mostly to preserve the SME and SE properties of the welded joint. Melting of the microstructure and composition change due to the alloy high affinity and sensibility to other elements lead to the loss of these SM properties. Thus indirect melting processes, such as friction stir welding of thin plates were investigated [83].

The use of interlayer in case of dissimilar welding has been widely used to avoid brittle intermetallic phases formation [48]. A patent has been claimed by Mietrach in 1987 on bonding titanium alloys to ferrous ones using diffusion welding and successive interlayers to avoid brittle phase formation [84]. Hall claimed another patent on welding titanium to ferrous metals, but the nickel used as filler material to modify the weld pool composition and its poisonous ion reduce the biocompatiblility of the welded devices [85].

Nevertheless, laser welding is also a common technique used in dissimilar metallic

materials joining without interlayer use [28, 86], even in the case of NiTi-SS [30, 31]. Sun and Ion [28] first reviewed the subject of laser dissimilar welds in 1995 for several metallic alloys and welding configurations. These authors reported that welding Ti and Fe alloys was particularly difficult but possible. Favez [56] welded successfully SS with gold, using the difference of absorption between the two materials and Marangoni convection associated with the gold composition gradient.

In 2002, Uenishi *et al.* [30] welded SS wires with NiTi wires in crosswise and parallel configurations. They achieved satisfactory quality welds with wires of 150 to 350 µm, but did not try a butt weld configuration. The most recent study on the SS-NiTi subject was published by Gugel *et al.* in 2008 [31]. The authors achieved faultless joints between wires of SS and NiTi by Nd:YAG laser spot welding in a butt to butt configuration. The mechanical properties of the joints were determined by tensile testing, but no metallurgical analysis was conducted on the welds.

Two more patents were claimed on dissimilar laser welding of NiTi in the field of biomedical engineering, first by Ales on welding medical guidewires core to another part using laser or similar heat flux sources [87]. This patent is more about weld configuration and welded part geometries. The second patent claimed by Flanagan was on the subject of dissimilar welding of stents with radiopaque markers, such as gold and copper, which have higher laser reflectance than NiTi [88].

2.3 Design of Experiment

Three different sets of experiments were made on NiTi-SS system, two with a pulsed laser and the last with a continuous laser. They are based on an improved full factorial design. Explanations of the full factorial design and then the different modifications leading to the two chosen models are given in Appendix A. A first set of experiments considered seven parameters (*Position*, t_p, PPP, f, PS, I and V, see Sect. 5.2). The two others were made with a reduced number of parameters, which are detailed in the results section as they depend on the first set analysis.

Chapter 3

Experimental methods

This chapter describes the different experimental setups used during this study. First, samples compositions and their preparation will be detailed (section 3.1). Then the laser welding facilities and their orbital positioning will be discussed, either in pulsed or continuous configurations (section 3.2). The furnaces used for unconstrained (infrared) or constrained (Bridgman) growth solidification experiments and their samples will be detailed (section 3.3). Finally, a list of the microstructure observations and analysis equipments and the used techniques will be made (section 3.4).

3.1 Samples

This research was focused on one composition of nickel-titanium shape-memory alloy and stainless steel, the concentrations of which is listed in Table 3.1. Both NiTi and SS were delivered by the industrial partner, Heraeus Materials, manufactured and certified by Fort Wayne Metals, Indiana. All the wires came from a single production lot of each material, to ensure maximal reproducibility of experiments over the duration of this research.

All NiTi alloys used during welding or solidification experiments were certified to have a 50.8 at% nickel composition, thus to be austenitic (superelastic) nickel-titanium alloy at room temperature (see section 2.1.1). Welding tests were also done with a platinum-iridium alloy, containing 10 wt% Ir, as mentioned in the initial project research plan, corresponding to the needs of the industrial partner.

Table 3.1: Composition of SS and NiTi wire materials in weight percent, according to the manufacturers.

Alloy	Denomination	Ni	Ti	Fe	Cr	Cu	Mn	C
NiTi	SE508	55.95	Bal	<0.02	<0.01	<0.01	-	<0.03
SS	304V	8.56	-	Bal	18.59	o.25	1.25	<0.08

3.1.1 Preliminary samples

Over the whole study, several types of specimens were produced, according to specific experimental purpose. Welded couples were produced using different lasers and sample shapes. At an early stage of the research, preliminary samples were done on massive specimens of austenitic NiTi (brand denomination SE508). The goal of these experiments

was to find an operating window for classical laser parameters, such as pulse duration and pulse power. These were all stainless steel or nickel-titanium autogenous weld beads made at different moving speeds.

Afterwards, welding between massive plates of NiTi and stainless steel was made. The specimens were cut in a massive ingot by Electrical Discharge Machining and were manually polished with SiC grinding paper, to recover a mirror surface.

Some of the plates were machined down to a thickness of 300 µm in the welding region, in order to approach at best the final geometry of the wire couple. This was done when solidification shrinkage cracks were thought to be induced by the remaining unmolten contact surface between the two plates below the weld pool. As the plates were in contact and the molten bath not crossing the entire thickness, a tensile strength was thought to induce hot cracking in the bottom of the solidifying weld bead (see section 2.2.7).

3.1.2 Wire samples

The NiTi wires were delivered with a diameter of 400 µm and stress annealed by the manufacturer. Afterwards, they were wire-drawn in the Heraeus Materials Components Division in Switzerland to reach the final requirement of 300 µm diameter. Finally, the wires were annealed again to recover their superelastic property and rectified to keep a perfect straight shape.

The wires were cut down to 30 cm segments using a Rawiler SiC disk saw and their surfaces were rectified by Electrical Discharge Machining (EDM) all in a single path, to avoid edge-rounding effects. The black oxide layer that develops during the annealing treatment was chemically etched to obtain an oxide-free surface, just before laser welding. Chemical solution used for oxide removal was composed of 10% volume of hydrofluorhydric acid (HF), 40% volume of nitric acid (HNO_3)[24]. The wires were etched for approximately five minutes before being washed and swept manually.

The NiTi wires superelestic plateau was characterized by the manufacturer at 545 MPa, with an elongation of 8%, which is corroborated by the further *in situ* tensile testing (see section 6.1.1).

Stainless steel wires were used as received from the same manufacturer, who produced them by wire drawing, directly to the final diameter (300 µm). They were cut and rectified in the same way as the NiTi wires.

3.2 Laser welding

Three different laser installations were used for the samples produced during this work. Preliminary investigations were done at the LSMX (*Laboratoire de Simulation des Matériaux*), EPFL, where massive autogenous remelting were made on NiTi plates and few massive dissimilar welding parameters were experimented. Afterwards, the dimensions were reduced to that of the wire samples and the configuration switched from planar to orbital welding. These second investigations were done on both a continuous and a pulsed laser orbital welder. The continuous laser was at Bredam (*Bureau de recherche et de developpement d'appareils médicaux*) in St-Sulpice, and the pulsed laser in HMCD (*Heraeus Medical Components Division*) in Yverdon-les-Bains.

3.2.1 Massive laser welding

Preliminary laser welding experiments were made at LSMX-EPFL, with a pulsed Nd:YAG laser, which is a solid-state laser rod excited with a flash lamp (see section 2.2.1). It has no frequency multiplication, so it emits in the infrared ($\lambda = 1064\,\text{nm}$), but a *beam-splitter* at its end offers the possibility to divide the power equally into two optical fibers. This was sometimes used to reduce the emitted power below its minimum (10% of the maximal one) as half of the beam was deflected and defocussed on a cooled target. It was a Rofin-Sinar RSY-1000P laser with a power of 1.2 kW, a pulse frequency range f between 0.4 Hz and 1000 Hz, and pulse durations t_p from 0.3 ms to 20 ms.

The laser was equipped with two possible focal diameter of 300 µm or 600 µm guided by optical fibres to the laser head. The sample holder was positioned by a 3-axis motion table and aligned with video recorded images.

Rectangular plate samples used for dissimilar (and similarly autogenous) laser welding were clamped on a vise and carefully aligned either horizontally or vertically to ensure correct focussing of the incoming beam on both plates. A force was applied on the vise to improve contact between the plates and counterbalance thermal shrinkage after welding.

3.2.2 Continuous laser orbital welder

As detailed previously (see chap. 2.2.3), several common configurations are used in laser welding. For this research, the final design requires a welding with a smaller diameter, or at least equal, to the initial one, so the butt-weld configuration was used. The two wires were aligned, facing each other, and then welded by a laser orbiting around the surface.

The orbital welding set-up (see fig. 3.1) was designed in collaboration with Bredam, who produced two positioning tables adjustable on both the continuous and pulsed laser setups. The device was made of two small grips, normally dedicated to hold a 300 µm diameter piece on a lathe, driven by a single rotating axis couple to an adjustable speed motor. The lathe grips (*Schäublin*) were aligned on an optical rail, and precisely positioned the wires, using two micrometric screws. The wires ends to weld were positioned with the help of hard metal jig bushings hold in a channel by springs. The loose end of the wires, coming out through the grips were held by a tube to avoid flapping. Finally, an argon shielding flux was blown to the welding zone from beneath, through a hole drilled in the channel between the two bushings, in order to have a laminar flux.

The laser used at Bredam was a continuous type fibre laser (Single-mode fibre laser, SPI Lasers (*Southampton Photonics Inc*), Model 200W-R3-SM-WC), with an initial focus diameter of 20 µm. In order to have comparative results with pulsed laser welding, the beam was defocussed to increase its diameter and the corresponding molten pool width to nearly 100 µm.

The welding parameters were varied according to first observation results to find an operating window. Further, a composite DoE was realized to find optimal parameters using continuous laser welding and were compared to pulsed laser DoE (Design of Experiment). The precise parameters used in these DoE are given in the result section as they were determined after the preliminary welds.

3.2.3 Pulsed laser orbital welder

Pulsed laser welding experiments took place in Yverdon-les-Bains on the HMCD production line, in a clean room. The pulsed laser is a Lasag SLS 200 CL8 with a focal diameter

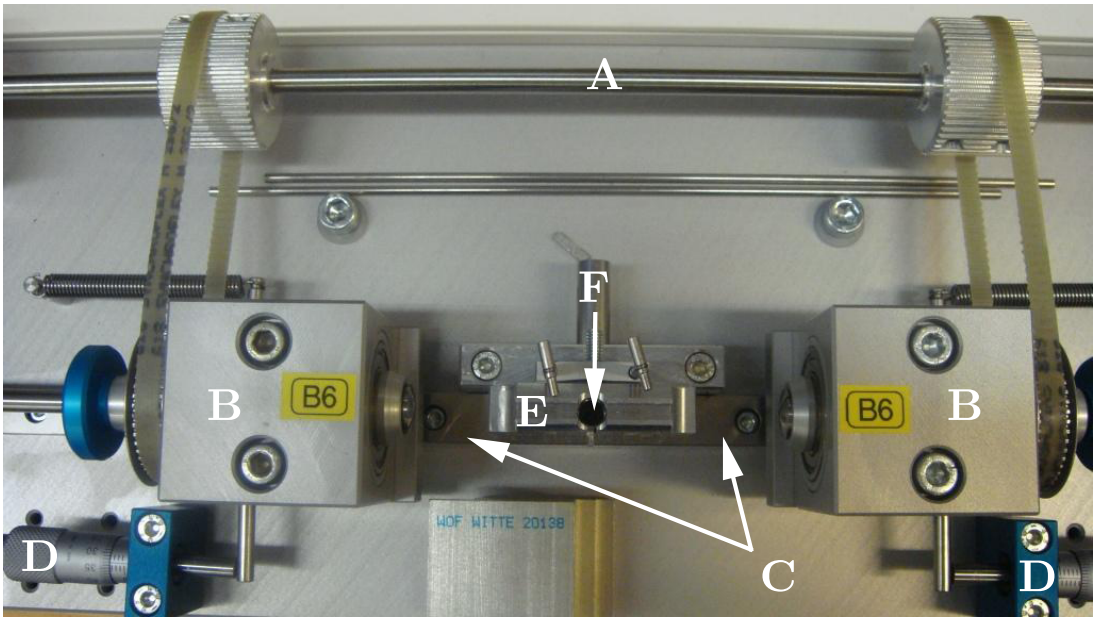

Figure 3.1: Overview of the laser positioning device, seen from above. The motorised axis (A) makes the two bands rotating the 300 µm diameter spring machine round collets into the spindles (B), to have a good synchronisation of the wire rotation speed. Both spindles are moved on a bench (C) with micrometric screws (D). The trench holding the wire drawing dies (E) is drilled with the argon shielding gas flux inlet (F).

of 100 µm aligned on a motorized linear guide (see fig. 3.2). This is a solid-state laser rod Nd:YAG laser with a 1064 nm wavelength (no frequency multiplier). The pulse duration range is from 0.1 ms to 100 ms, and the pulse frequency range, between 0.1 Hz and 200 Hz. The maximal pulse energy is 8 J and the average power maximum 10 W.

The positioning device was an exact copy of the one displayed at Bredam, for continuous laser welding (see fig. 3.1).

3.3 Solidification experimental devices

In order to investigate the different structures that grow under controlled conditions, several solidification experiments were made using a Bridgman and an infrared furnace. Sample compositions were defined to be similar in both set of experiments, which means three mixed samples and two pure samples, one for NiTi and one for SS (only in the infrared furnace experiment set, see Table 3.2).

Samples	Pure NiTi	25 wt% SS	50 wt% SS	75 wt% SS	Pure SS
Bridgman	-	BS_09	BS_07	BS_08	-
Infrared	IR_09	IR_07	IR_05	IR_06	IR_08

Table 3.2: Sample compositions for solidification experiments (Bridgman and Infrared furnaces), with their respective reference names.

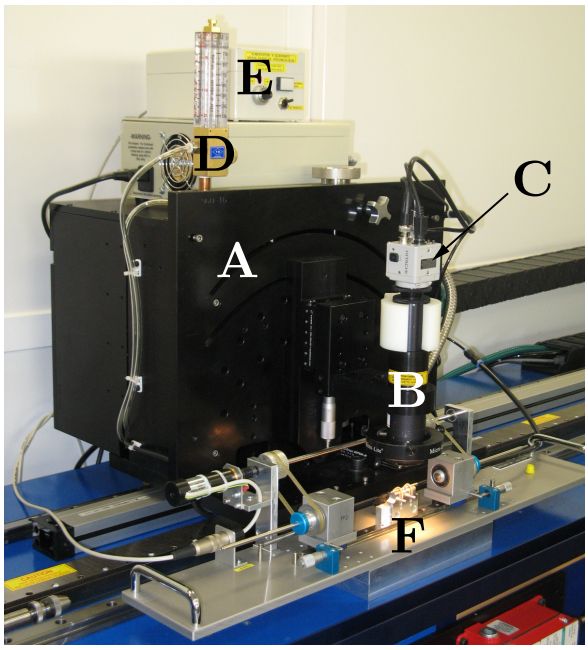

(a) Overview of the orbital laser, with the linear motorized head (A), the laser head (B) and the image recorder (C). Argon debimeter (D) and motor controller (E) are placed at the top of the motorized head. The positioning device (F) is set below the laser head, screwed on the table.

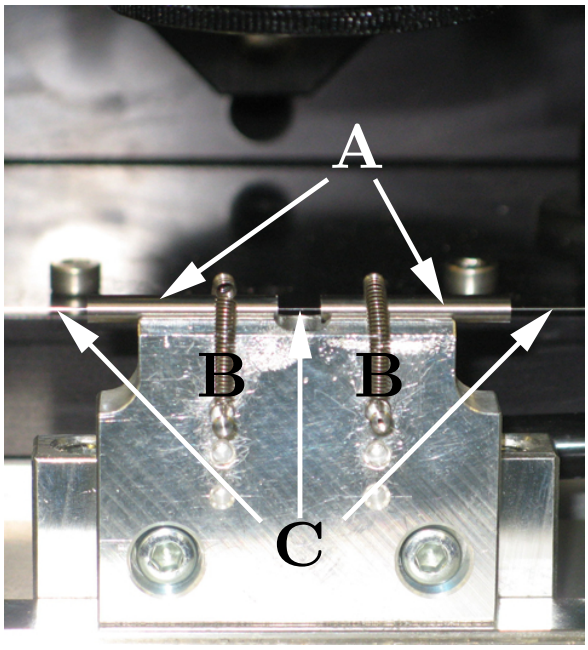

(b) Detail of the positioning pieces for the centering of the wires, showing the wire drawing dies (A) held aligned in the trench by the springs (B). Wires are visible in between and on each side of the picture (C).

Figure 3.2: Orbital welder overview and positioning pieces detail at Heraeus. The positioning device is identical to the one at Bredam (see fig. 3.1).

3.3.1 Bridgman directional solidification

Bridgman solidification experiments were done at LSMX, with an Elphiac© induction furnace especially designed for directional solidification in a high thermal gradient. The aim of these experiments is to obtain information concerning the phase formation sequences, depending on composition, as a function of the growth speed.

This Bridgman furnace is a vertical furnace in which a sample is moved at a constant velocity through a controlled thermal gradient (see Fig. 3.3). The sample is contained in a crucible, which passes trough a cylindrical molybdenum susceptor heated by induction coils coupled to a high frequency power source. The susceptor is wrapped in zircon insulating sheets in order to minimize thermal radiation, and thus maintain a fairly homogeneous temperature field over its whole length. Below the hot zone, an adiabatic zone and then a liquid metal cooling bath (LMC) underneath control the thermal gradient. This LMC is kept at room temperature by a water cooling system and the whole system is kept under vacuum. Vacuum (or controlled ambient) is compulsory to avoid molybdenum oxidation in the hot zone. Inside the furnace, a linear displacement device allows vertical motion and rotation of the sample at controlled rate during experiment.

The sample is contained in a 500 mm alumina crucible with an internal diameter of 5 mm. Bulk materials were precisely weighted at inquired compositions and melt in a induction heated vacuum furnace. The molten matter was cast as cylinders in a preheated copper mould with final diameter slightly below the crucibles diameter (4.5 mm and 11 cm long). Two of these were used for each experiment as a minimal length of 16 cm is required

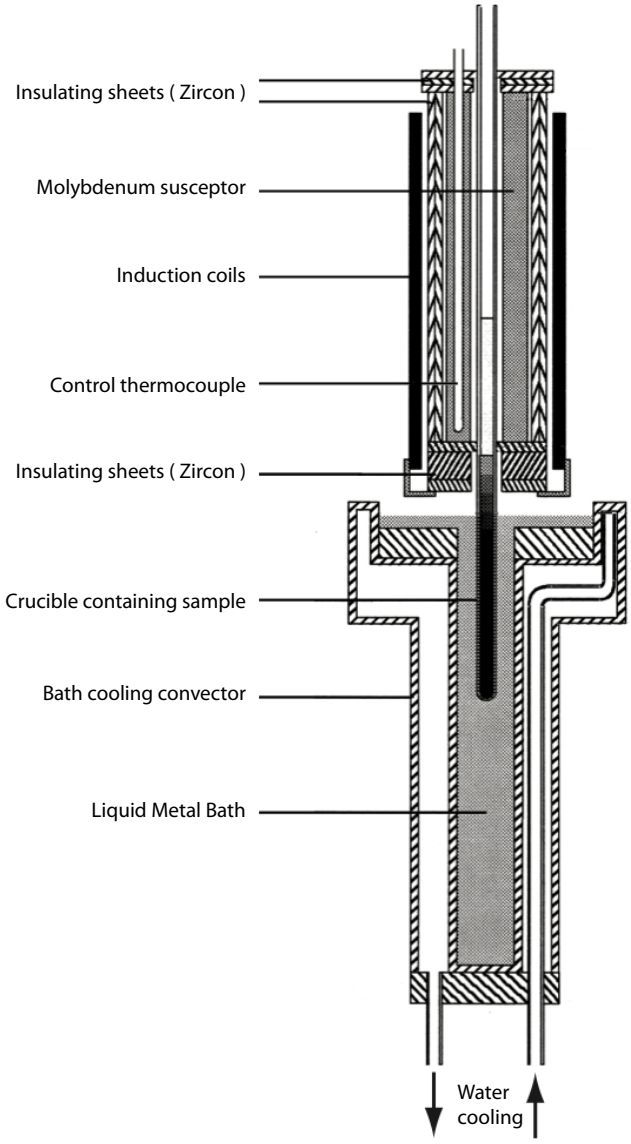

Figure 3.3: Scheme of the Bridgman furnace used for directional solidification experiments.

for a complete Bridgman sample.

The experiment itself can be divided into three main steps, corresponding to different positions of the sample, with respect to the LMC surface:

Heating of the sample is done inside the molybdenum susceptor under vacuum. A constant heating rate is imposed to the furnace until 1500 °C. Degassing occurs in the vacuum chamber around 700 °C and 400 mbar of argon are then used to prevent oxidation of titanium. A 30 min homogenization time is waited at 1500 °C to reach a steady temperature in the whole setup before starting the Bridgman experiment.

Sample positioning was established at a $3\,\mathrm{mm\,min^{-1}}$ speed downward, until the crucible was immersed 1.5 cm in the LMC bath. Position was held for 1.5 h, until thermal steady state and a constant thermal gradient were established in the sample.

Directional solidification was made with an imposed motion of the crucible into the LMC ($3\,\mathrm{mm\,min^{-1}}$) over a length of 5 cm. As the thermal gradient remained nearly constant, the imposed speed was also the solidification speed, thus a complete thermal history is present in the sample, explaining the importance of the last step. The thermal gradient in the adiabatic zone was evaluated to be about $20\,\mathrm{°C\,mm^{-1}}$, by Kohler and Favez [89, 56].

Quenching was done when the crucible was released into the LMC, as the sample holder is freed from motion device by the melting of its holding wire. The small Kantal wire that holds the sample is molten by Joule's effect when a current passes trough the wire.

After solidification, the specimens were extracted and further analysed, using mechanical polishing and optic or electron microscopy techniques (see sections 3.4.1, 3.4.2 and 3.4.3).

3.3.2 Infrared Furnace

The goal of these remelting experiments was to determine the liquidus (and solidus if possible) temperature for the different remelted compositions. As the cooling rate is highly important for microstructure nucleation sequences, several ranges of cooling rate have to be analysed. Between slow cooling in the Bridgman solidification experiments ($\approx 1\,\mathrm{°C\,s^{-1}}$) and rapid cooling in pulsed laser welding ($\approx 100\,\mathrm{°C\,s^{-1}}$), infrared solidification experiments were performed at LSMX to explore intermediate cooling rates ($\approx 10\,\mathrm{°C\,s^{-1}}$, according to measurements).

Infrared furnace (IRF) experiments were done at LSMX to obtain mixed samples at intermediate cooling rate. The furnace (VHT-E48 by Ulvac-Riko, Inc.) is made of four lamps, each placed on one of the two focal points of an elliptical mirror. These four mirrors have a common focal point (where the sample has to be located) and are placed at 90° from each other. A quartz cylinder acts as a shield in case of unexpected trouble and defines the maximal size of the experiment and positioning setup (see figure 3.4). The maximal power of the furnace is 24 kW, focused on the center line of the furnace.

As exposed above, the positioning device has to fit inside the protective quartz cylinder and allows the light to reach the specimen. Moreover, the specimen has to be held in the

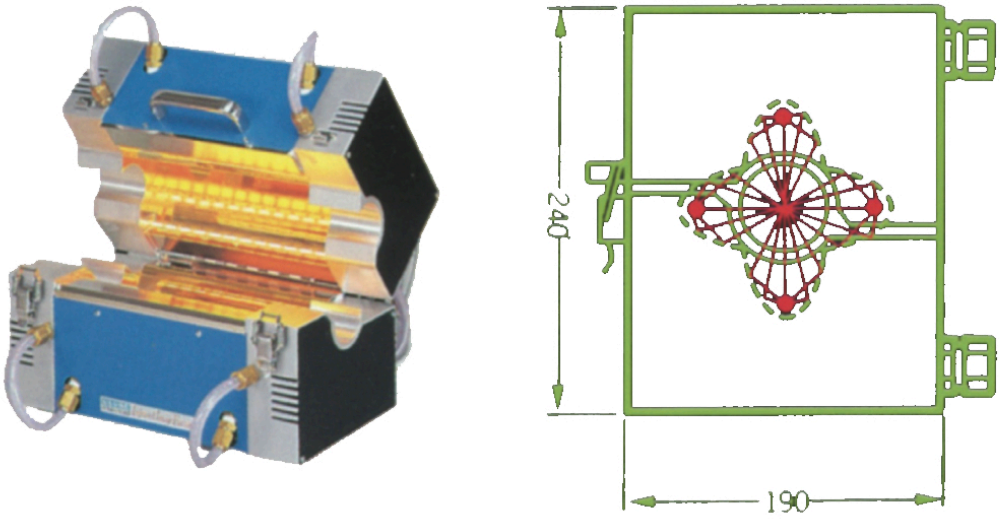

Figure 3.4: Global view of the Infrared furnace used for medium speed solidification (left) and lateral sketch of the furnace (right). The latter shows the four lamps and their light path to the sample (red), the gold plated elliptical mirrors (dashed lines) and the overall structure with dimensions (green) including the protective quartz tube containing sample holder.

middle of the device without any direct contact to a quartz piece, as this piece would melt and collapse or at least become opaque to the infrared radiation, and fail. Everything has to be held from outside the furnace where the temperature will be lower, by structure pieces in Macort for example, which need to be held below 450 °C to avoid cracks induced by thermal stresses.

The positioning device (see figure 3.5) was designed as two concentric quartz cylinders, the outer one is part of the infrared furnace and acts as a shield for the gold mirrors, and the inner one is required to pull the vacuum during all the experiment. The Macort guides were machined down to have a small gap with the quartz cylinder to avoid thermal stresses due to dissimilar expansion coefficients with the quartz. Another Macort guide was used to ensure a good centering of the alumina sheath, which contains the S-type thermocouple and holds the crucible in the middle of the furnace. This last Macort part was machined to allow air flow on its sides during pumping. The vacuum sealing was done by two especially designed aluminium connectors, one equipped for thermocouple data acquisition and the other for vacuum pumping. A mobile pumping unit made of a vane pump followed by a turbomolecular one, aiming to reach a sufficient vacuum quality to avoid titanium oxidation (around 1×10^{-5} mbar).

The crucible itself was made of a 6 mm diameter compact graphite rods cut to 2.5 cm long segments with a perpendicular drilled hole in the middle (see figure 3.5, magnified view). The center hole acts as the crucible containing matter to remelt, and the alumina sheath as a holding part for the crucible. The sheath contains a thermocouple for thermal data acquisition and furnace temperature control command.

The infrared samples were prepared using plates, which were machined to 4.5 mm diameter disks and superimposed one above the other. The plates were grounded to desired weights to obtain chosen compositions by adding several of them. The SS base material was placed below the NiTi, which led to carbide formation issues in the SS and thus a change between the expected compositions and the measured ones (see section 4.1).

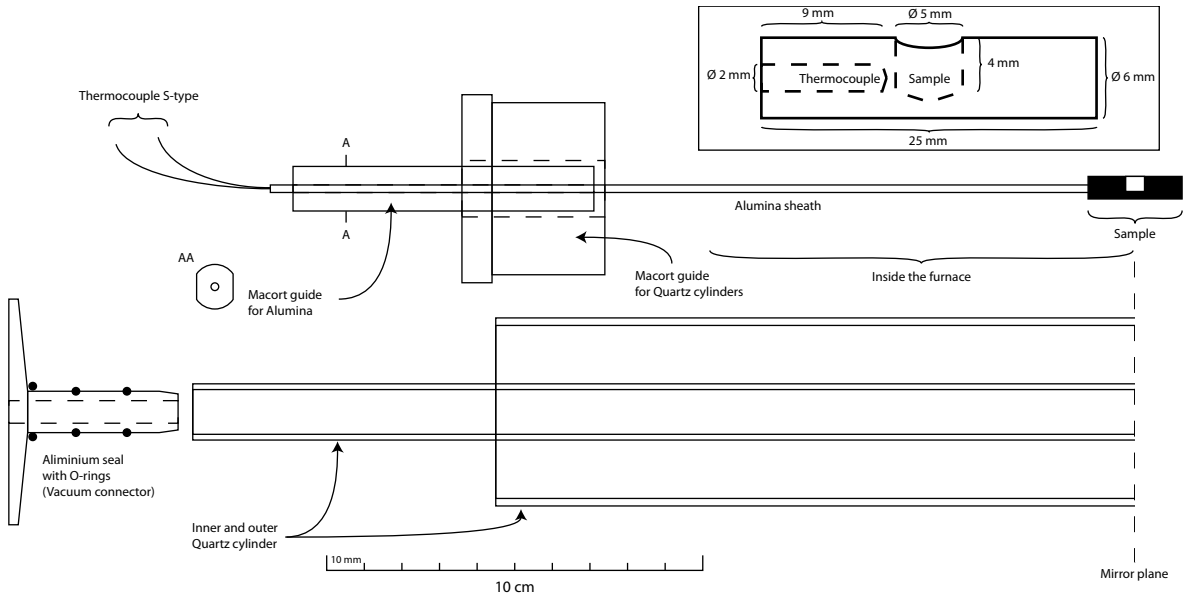

Figure 3.5: Sketch representing the design and positioning device for the infrared furnace experiments. Above, the several ceramic pieces (alumina sheath and Macort guides) are shown with the thermocouple and the graphite sample holder. Below, the two quartz tubes are sketched with their metallic (aluminium) seal for vacuum pumping, with a symmetry at the center of the furnace. All pieces are drawn with the same scale except the magnification of the graphite crucible, showing the holes drilled for the sample and the alumina sheath containing the thermocouples (shown in dashed lines).

Experiments were conducted with a $2\,^{\circ}\mathrm{C\,min^{-1}}$ heating rate and a natural cooling with a reduced power of 25% of the lamps (less than 6 kW). A minimum power during cooling was necessary in order to reduce the cooling rate (in absolute value), as a too large power induces too much noise in the cooling curves. With this reduced power, the cooling rate was about $10\,^{\circ}\mathrm{C\,s^{-1}}$ close to the liquidus, but no latent heat release effect could be detected in the cooling curves. Thus no information about solidification interval could be deduced. Finally, after complete solidification, the samples were cut in halves and prepared by mechanical grinding to a mirror surface quality for SEM EDX measurements (see section. 4.1).

3.4 Microstructure analysis

Several techniques were used for observations, analyses and weld microstructure characterizations, namely optical (OM), scanning (SEM) and transmission electron microscopy (TEM). 3D reconstructions or views were obtained using focussed ion beam (FIB).

3.4.1 Sample preparation

Samples were prepared using a fairly similar procedure, except for initial cutting. Concerning laser welded couples, the samples were reduced by wire sawing to a small segment of half a centimetre and glued onto a small aluminium sample holder. Afterwards, they were polished down to the wire center to have a longitudinal cut of the welded part. Bridgman and infrared furnace samples were cut by EDM or SiC cutting disks, and then

polished like the laser welded wires, using a tripod on polishing disks.

The polishing was done with a tripod polisher on diamond lapping films *(Allied Company, Diamond lapping films type B)* with proper acetone and ethanol cleaning between the various steps of downsizing diamond particle sizes (6 micrometer, 3 micrometer, 1 micrometer, 0.1 micrometer). The final step was a mechanical polishing using a colloidal silica solution (grain size of 0.02 micrometer), that makes a little chemical etching of the surfaces *(Buehler Company, Mastermet 2)*. Finally, samples were cleaned with demineralized water and dried to avoid dust.

3.4.2 Optical microscopy (OM)

For Bridgman solidification samples, the fairly coarse microstructure and the size of the specimen were such that optical microscopy was priorly used. A Reichert *(model Me-F3)* optical microscope was used with polarized light and interference contrast to enhance the microstructure details.

3.4.3 Scanning electron microscopy (SEM)

Scanning Electron Microscopy (SEM) was made at the CIME on FEI-XLF30 microscopes, one optimized for high resolution imaging (SFEG) and the other used for *in situ* tensile testing and Energy Dispersive X-ray spectrometry (EDX).In Electron Microscopy (EM), the same configuration was used for all techniques, but several signals are emitted from the sample, each being used for a specific purpose.

Secondary Electrons (SE) are loosely bound electrons from the sample atoms, for example outer shell electrons. They are emitted when inelastic interactions between incident beam electrons and sample atoms give sufficient kinetic energy to eject them from their energy layer. Thus, they have a low energy (<50 eV) and those escaping the sample come from the near sample surface (few nanometres) as the deeper ones are reabsorbed by the sample. These SE can be attracted by a potential (around 200 eV), thus their detector can be placed away from the sample. As their number depends mostly from the tilt angle of the surface, the obtained contrast is mainly due to topography [90].

BackScaterred Electrons (BSE) are incident electrons that had one or, most of the time, several elastic interactions with sample atoms to be deviated away from the surface and be detected. If they are also dependent on the tilt angle (used for EBSD technique), another important parameter is the average atomic number (Z) of the sample. Indeed, more interactions occur when the atoms are heavier, thus BSE signal gives a mass contrast of the sample with few topography information. The BSE coefficients can be approximated by a third order polynomial equation, and by a linear mixing rule regarding the phase composition. In the case of NiTi and SS mixing, the average BSE coefficients are quite similar and the contrast has to be optimized to reveal the microstructure. Contrariwise to SE, BSE cannot be deviated and have to be collected as close as possible from the sample surface. One drawback of BSE regarding SE is the large interaction volume from where they are issued, as they have much more energy than SE [90].

X rays are produced when an outer shell electron looses energy to fill a lower energy position left empty by another electron, for instance when an incident electron interacts with the matter. Thus, this photon has a very specific energy for each element, equal to the energy transition between orbitals, which can be quantified and identified to give information about the sample composition. As in the case of BSE, X-ray cannot be deviated and thus a collimator is oriented in the direction of the sample to avoid signal from other regions (due to BSE), and a precise working distance (WD) between sample and lenses has to be respected [90].

These three main interactions between beam and matter are used in the same way, which is the discrete scanning of the sample over a grid. At each point, the desired signal is recorded and the scanning continues after a defined elapsed time. This mapping is regrouped in an image where each pixel has a grey level corresponding to the intensity of the signal at this point. In the case of EDX signal, the recording is a spectra that can be quantified to determine concentration of desired species at each point, and thus EDX signal gives several grey level maps.

Electron BackScatter Diffraction (EBSD) technique, on the opposite, is based on recording a full camera image at each scanning point. This tremendous difference is a key parameter that allows to record information about sample crystallography using Bragg's diffraction in an SEM. The sample has to be tilted to a 70° angle with respect to the incident beam, with an acceleration voltage around 20 keV being an optimum for signal in this technique. Indeed, this specific positioning of the sample leads to a scattering of the incident electrons inside the matter, which then diffract at the sample surface while exiting the sample (when Bragg's law is satisfied). The sample acts as a point source, thus the diffracted electrons form two cones. These cones have huge opening angle due to the flat Ewald sphere associated with electrons [91, 92]. When these two, so called Kossel's, cones intersect a vertical phosphorous screen, flat-hyperbolic curves appear (a bright band inbetween missing signal black lines), so called pseudo-Kikouchy bands, due to an analogy with TEM diffraction. These bands are characteristic of the sample structure crystallography and allow a rapid Bravais lattice identification. This technique allows new possibilities in phase determination as it depends only on crystallography and is very useful in the case of similar phase compositions or unknown phase solubility. But it requires a complete database of the search phases and is limited by similarities in crystal structures. This technique was used as a validation to EDX measurements as laser rapid cooling may lead to unstable phase compositions. However, it was limited due to the interaction volume of BSE that can bias the crystal identification, by recording polycrystalline informations. Moreover, a deformation free surface is required as the Bragg's diffraction occurs in the first 20 nm below the sample surface. Thus, a chemical or electrochemical polishing is most of the time required, to get rid of the mechanical strains induced during polishing.

3.4.4 Focused Ion Beam (FIB)

The Focused Ion Beam (FIB) technique allows a precise sample milling using heavy ion impacts, and is usually coupled to a traditional SEM to compose a so-called "dual beam" platform. FIB instrument itself is very similar to an SEM running a liquid metal ion source

in place of the usual electron source. This source is most of the time made of gallium due to its low melting point and low vapour pressure. Moreover, its low surface energy allows ensuring a good wetting of the tip and its electrical properties are high enough for a perfect use of these ions. The latter are extracted by an electrical field ($1 \times 10^8\,\mathrm{V\,cm^{-1}}$) and accelerated through the ion column by a voltage in the range of 5 to 30 keV. The ion beam current can be varied from a few picoAmperes to 20-30 nanoAmperes, depending on the desired milling speed. High quality surfaces are obtained at low milling speed, since it avoids redeposition of ejected matter onto the surface and ensures a perfect flatness of the milled surface. This last milling also reduces radiation damages, such as amorphization.

FIB technique can also be used to deposit matter by gas precursor deposition at selected places. This is used to protect a surface or as a welding technique during so-called "lift-out" transfer technique. The precursor is an organometallic gas containing the desired ions and is blown near the sample surface to be adsorbed. However, these adsorbed molecules only decompose where the ion or electron beam interacts (emitted SE split the precursor), allowing an accurate deposition on areas of interest.

The instrument (*Zeiss NVision 40 CrossBeam*) used in this work is a dual beam platform allowing a high lateral resolution milling (4 nm at 30 kV) by the FIB column while imaging with SE. This technique may be used to produce thin lamellae necessary to transmission electron microscopy (see section 3.4.5), but also for volume reconstruction using successive slicing and imaging or EDX mapping.

In the case of TEM lamellae production, the sample is milled out perpendicularly to the visible surface, the area of interest being previously protected by carbon deposition to avoid its milling during imaging. Afterwards, clearance tranches are cut on each side and the lamella can be grounded in several steps with reduced speed. This milling speed decrease aims also to avoid Ga^+ ions implantation in the surface, while it makes a non-zero angle with the ion beam. To avoid redeposition, the specimen is cut and extracted from the massive sample before the final thinning thanks to micromanipulators, then welded onto a TEM sample grid using precursor gas decomposition. At the end, the lamella is thinned until its two perfectly parallel surfaces are free of defect (and down to electron transparency). Typical sizes for these lamellae are 5 µm by 5 µm and are electron transparent for TEM imaging and diffraction (below 100 nm thick, depending on material density).

In the case of volume reconstruction by SEM imaging and EDX mapping, the process is similar except that a cubic volume has to be protected and cleared. The front face, which is milled, faces the EDX detector. Redeposition or parasite X-rays due to BSE impact on bulk materials have to be avoided during milling, therefore the other side of the specimen has to be milled. The volume reconstruction is made by successive SE images or EDX maps taken between defined milling steps. The typical voxel (unit volume) resolution in SE images is around $10 \times 10 \times 10\,\mathrm{nm^3}$ while EDX resolution is lower (around $100 \times 100 \times 100\,\mathrm{nm^3}$) due to the high interaction volume where X-rays are generated. Finally, the corresponding images are piled up in stacks and treated by applying imaging filters to extract desired contrast or phase compositions.

3.4.5 Transmission electron microscopy

Accurate phases identification was made at specific locations of the welded samples by Transmission Electron Microscopy (TEM), using a *Philips CM300*. Indeed, due to the rapid cooling and solidification rate, weld microstrucures are very fine and thus difficult to

identify by EDS in SEM bulk samples. As TEM lamellae are much thinner, the interaction volume generating EDX signal is tremendously reduced and chemical measurements are more accurate for local sampling. Observations were made in DSTEM (*Dark field Scanning Transmission Electron Microscopy*) using an ADF (*Annular Dark Field*) detector, which collects diffracted and diffused electrons only, while the thin electron probe scans the region of interest. The advantages of this technique is to reveal a contrast in atomic number, although it contains a diffraction contrast too. As the image is formed by the scan of a very thin probe, it is then easy to position it accurately on a small region of interest for EDX analysis.

TEM lamellae were produced by the standard FIB lift-out technique [93], in regions of high interest such as the interface between the weld and the NiTi base wire, where a particularly bright contrast was observed. Samples were also taken in the bulk of the weld to get phase compositions and an accurate identification of the different concentrations of species as a function of the location in the weld pool.

3.5 Mechanical Testing

In order to test the mechanical properties of the welded couples, which is key for the final application, several tests were performed. Most of them were wire tensile testing, either classical (see section 3.5.1) or *in situ* (see section 3.5.2) inside an SEM with observations of the inhomogeneous strain field using automated Digital Image Correlation (DIC) (see section 3.5.3). Fracture SEM imaging and analysis (see section 3.5.4) was made on broken samples while nanoindentation (see section 3.5.5) measurements gave local mechanical properties required for simulations in specific regions of the welded specimen (see chapter 6.1.4).

3.5.1 Tensile testing

Tensile tests were performed on laser welded wire couples at the Haute Ecole Spécialisée de Suisse Occidentale (HES-SO) in Sion (Valais). They were done with a Zwick© tensile tester (Typ 1455 20 kN Materials Testing Machine, Floor-Standing), with a 2 kN force sensor.

The samples were wire NiTi-SS couples welded with a continuous or pulsed laser, varying key process parameters, with a typical length of 30 cm for each materials (total length of 60 cm). The tensile testing protocol followed the ASTM standards F2516-07 *(Standard Test Method for Tension Testing of Nickel-Titanium Superelastic Materials).*

Each end of the specimen was attached using a capstan grip, and an initial length of 15 cm between grips for tensile testing. The test was controlled by the displacement speed ($0.5\,\mathrm{mm\,min^{-1}}$) of the mobile crosshead. Preloading was mandatory to avoid misalignment or displacement resulting in a partial unloading during tensile experiment. To ensure a good repeatability of the experiments, 10 samples for each set of welding parameters were tested in a complete random order, to minimize systematic errors.

3.5.2 *In situ* tensile testing

The purpose of these tests was to understand the interesting mechanical behaviour of the welded area under tension. Indeed, failure of the joint happened on each sample at the end of the superelastic plateau.

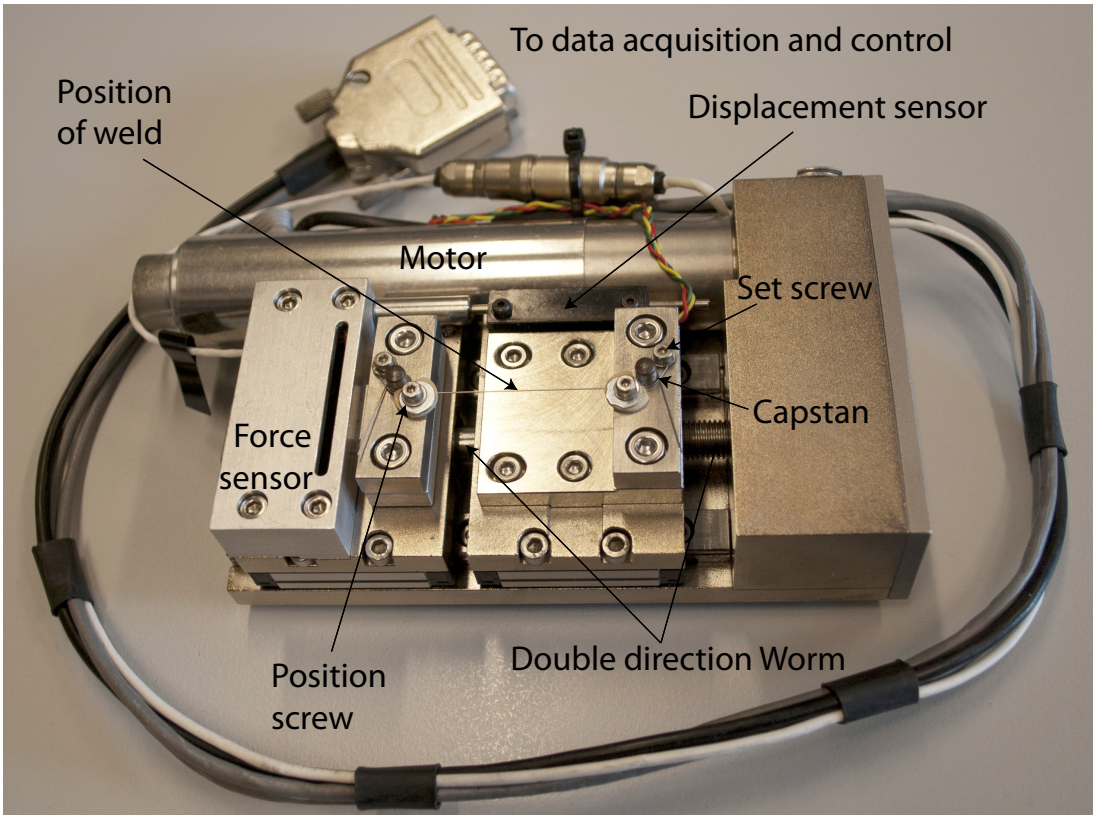

Figure 3.6: Picture of the *in situ* tensile testing device used in SEM, showing the wire couple positioning at initial state.

In situ tensile testing were done at CIME on a small tensile tester adapted to fit in an SEM vacuum sample chamber. This device was designed by Deban© (see fig. 3.6) and modified with capstan grips to satisfy micrometric wire tensile testing. It was equipped with a 695 N force gauge and a double direction worm controlling clamp motion, and two positioning screws with rubber plates to avoid wire movement when superelastic deformation recovered after breaking. The initial length between the clamps was 5 cm and the displacement speed was set to $0.5\,\mathrm{mm\,min^{-1}}$. This was chosen to keep a deformation rate similar to the tensile tests made at the HES-SO (see section 3.5.1), as it is the lowest displacement speed available on the controller. As the NiTi wires superelastic plateau is at 550 MPa (which gives a tensile force on the gauge around 35 N for a 300 µm diameter wire), a 10× gain was used to increase the resolution on the sensor measurements. Moreover, a calibration of the force sensor was done using the superelastic stress of a NiTi homogeneous wire, using another calibrated tensile machine and similar test parameters.

No deformation gauge was used as the traditional extension measurements sensors with blade grip would lead to failure and the sticking elongation gauge could not be placed onto the sample. Thus deformations were obtained by relative displacement of the grips normalized to the initial grip gap.

Even if the two grips move symmetrically on both side of the observed region, repositioning of the sample had to be done several times during testing due to the very different properties of NiTi an SS. SE surface images were taken at several steps during testing. Moreover, SE imaging was averaged over a long dwell time to reduce statistical noise and thus enhance the image contrast. As some compliance of the tensile testing device was observed, *i.e.*, sample relaxing and thus displacement between the several images, a

multiple image averaging was not a choice to decrease the noise.

Cross-sections of a couple of *in situ* tensile tested specimen were prepared by mechanical polishing along the wire axis. In order to have a sufficient precision in positioning the two broken parts of the specimen after failure, small metallic references were glued on each wire before tensile testing.

A few welded couples were grounded down to a final diameter of 200 µm, in order to remove inhomogeneities on the welded surface. The aim was to get rid of artefacts (such as surface defect, weld reduced section, preferential crack initiation site), when unusual fracture mechanism was observed. Their diameter was reduced by centerless mechanical grinding technique at Heraeus Medical Components Division in Yverdon. All these samples were produced with same weld parameters, the one leading to the highest weld mechanical properties.

3.5.3 Automated digital image correlation

Investigation of strain field inhomogeneities during *in situ* tensile tests was made with automated Digital Image Correlation (DIC) from SEM SE micrographs. It has been performed using CMV, a specific software developed at the Ecole Nationale des Ponts et Chaussées (ENPC) by Prof. Michel Bornert.[94]

The images were subdivided into square juxtaposed correlation windows. Their size, around 30x30 pixels, was chosen such that each window contained enough natural image contrast for automated pattern matching. This contrast was essentially due to surface imperfections induced by grinding (asperities, inclusions, scratches, etc.). The wire was discretised into 30 windows along its diameter. The motion of each window was deduced by standard DIC algorithms, making use of an affine shape function and bilinear grey level interpolations to reach subpixel accuracy in displacement evaluations.[94] Once the displacement of the center of each window was determined, the strain field was computed using an 8-neighbours scheme in order to reduce the resulting standard deviations, following Allais *et al.*[95] Because the natural contrast of the images was low, the resulting accuracy was below that usually expected from DIC algorithms, but was however sufficient to quantify and compare strains in various parts of the wire. The mesh had to be interrupted along any singularities, such as a crack, as the deformation deduced from opening is singular.

3.5.4 Fracture analysis

A selection of the most interesting tensile tested broken samples were observed by SEM either at HES-SO (concerning DoE sample series) or at EPFL (for the *in situ* tested samples). These observations aim to point out accurately the failure area where the crack propagates and the resulting fracture microstructures. Analysis were done on both wires fracture surfaces, by SE imaging and EDX mapping.

Samples were picked out in the batch of DoE designs, especially when unusual behaviour, fracture mechanism or Ultimate Tensile Strength (UTS) was observed. The broken surfaces were oriented perpendicularly to the beam and carefully identified. Analysis were made on a Zeiss (Model LEO 1525) equipped with a Gemini column. SE imaging was used to enhance topography contrast, as BSE phase density contrast would be biased by the roughness of the surface area. For the same reason, EDX measurements were rather qualitative than quantitative.

In situ tensile tested samples were observed by SEM on a Phillips XLF-30 microscope using SE signal. Surface roughness reconstruction was made using three symmetrically tilted images around the perpendicular position (angles: $-7°, 0°, 7°$). This reconstruction was done with the help of the MeX software, provided by Alicona©. This allowed to make a clear distinction between brittle and ductile fracture surfaces, as the roughness is much more important in the second case. Moreover this stereoscopic reconstruction allows to draw the fracture surfaces or to profile and map deformation structures in the ductile areas.

3.5.5 Nanoindentation

Local mechanical properties of base materials and welded zone, such as Young's modulus and yield stress of the elastic domain, were needed to model stress and strain. Thus, nanoindentation experiments were done on a representative welded couple, to determine its local mechanical properties, especially in the Heat Affected Zone (HAZ) of each wire and in the transition region between the wire and the welded area.

The experimental device mapped automatically a defined region of half a cross-section of a welded wire with a constant spacing between each measurement. These measurements were done with a Berkovitch-type (three faced-pyramid) indenter and using the continuous stiffness method detailed by Oliver and Pharr[96]. The Berkovitch indenter was preferred to the Vickers one especially because sharpness of the tip is easier to ensure when only three surfaces are present (Vickers indenter tends to have an edge at its end). Moreover the property calculations are the same as Vickers calculations, commonly used in industry.

The maximal penetration depth of the indenter was set to $1\,\mu m$ with a penetration speed of $5\,nm\,s^{-1}$. A harmonic amplitude of $2\,nm$ was superimposed to this penetration motion in order to provide a continuous calculation of the Young's modulus and hardness over the experiment. At low penetration depth, the measurements were quite noisy as the surface of contact between the indenter and the specimen section was very small. This noise decreased as the indenter penetrated deeper in the material and the tested volume became more representative of the polycrystalline specimen. For these reasons, the values given in the result section were averaged over the last stage of the indentation curve.

Chapter 4

Controlled speed solidification

This chapter presents the results of the controlled speed solidification investigations performed during this work. First, infrared furnace experiments are discussed as an unconstrained growth solidification experiment. Then, Bridgman furnace results are summarized for the constrained growth investigations. Controlled speed solidification experiments were used to get information about phases that might appear for different compositions of the NiTi-SS system. As detailed in the experimental section, several specimens were prepared with a desired dilution ratio. Moreover, these experiments were performed to get qualitative information about the solidification speed dependence of the phase formation. For both experiments, the resulting phases after solidification were observed by OM, SEM and chemical analyses were performed using EDX.

4.1 IR Furnace

Five mixing ratios were investigated using the infrared furnace described in section 3.3.2. Actually, three had mixed compositions and two corresponded to the pure base materials (SS and NiTi). The mixed specimens were chosen at equidistant composition on the ternary phase diagram (see Fig. 4.1). The infrared furnace experiments were done using graphite crucibles to have a fast heating of the specimen due to the graphite high absorption in the infrared wavelength. The drawback is that specimens with high SS content exhibited iron and chromium carbides formation. Only the pure NiTi and the 75% NiTi - 50% SS (sample C) specimens had final compositions as predicted by the initial mixing ratios. The mixing was done using bulk SS and NiTi plates placed one above the other (SS plate being at the bottom, see Fig. 4.2a). The SS bulk plates encountered carbon diffusion, reducing the amount of SS in the final composition (see Fig. 4.2b). Thus, the original 50% NiTi - 50% SS (sample B) became a 63% NiTi - 37% SS (sample B') and the 25% NiTi - 75% SS (sample A) became 50% NiTi - 50% SS (sample A'), see table 4.1 for compositions. The pure SS sample had completely reacted with the crucible and a large amount of carbon was measured (more than the maximal 5 wt.% of cast iron, according to the EDX measurements, meaning that saturation is reached) and was thus not interesting anymore for this study. The pure NiTi sample showed a normal equiaxed solidification leading to globular grains of NiTi phase (not shown). All the following discussions will focus on the measured sample compositions with their respective sample names (A', B' and C').

EDX measurements in the carbides areas showed the exact predicted concentrations in the three main SS elements (Fe, Cr, Ni) plus a large amount of carbon. The composition

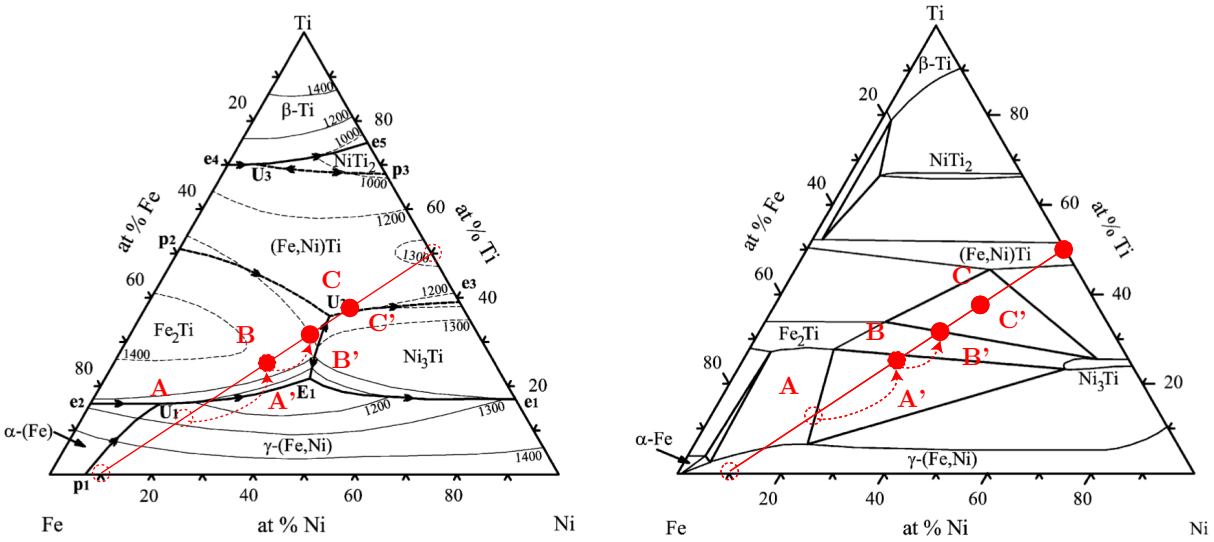

(a) Fe-Ni-Ti liquidus projection with the highlighted compositions used in controlled solidification experiments [43].

(b) 900 °C isothermal cut with the highlighted compositions used in controlled solidification experiments [42].

Figure 4.1: Studied compositions were defined at 25% (A), 50% (B) and 75% (C) weight ratios of the base materials (NiTi and SS). Two more experiments were done with the base materials. Chromium is not taken into account for the composition reference of SS (Fe-10%Ni). The dashed circles correspond to nominal compositions and the filled dots to the final (the arrows highlight the change due to carbides formation in SS). The actual composition of (A), *i.e.*, (A'), is superimposed with the (B) composition, which actually moves to (B').

of the remaining zone mixed with NiTi was changed from the expected composition, but the carbon level was low. This carbide formation results in a large unstudied SS-rich region of the ternary phase diagram, which was not really an issue as most of the interest was in the NiTi-rich side of the phase diagram.

According to the liquidus projection of the ternary phase diagram, the 50% NiTi-50% SS (A') and 63% NiTi - 37% SS (B') should have similar primary phase (Fe_2Ti) but a different final microstructure as the A' sample should hit the U_1-E_1 monovariant line and the B' sample the E_1-U_2 line.

BSE SEM observations enforced by EDX measurements showed two distinct areas in the A' mixed sample (see Fig. 4.3). The first (SS-rich area at the bottom of the A' sample) with a primary γ-(Fe,Ni) phase surrounded by a γ-(Fe,Ni) and Ni_3Ti eutectic (see Fig. 4.3a). The second (NiTi-rich area at the top of the A' sample) with Fe_2Ti dendrites encircled by a Fe_2Ti and Ni_3Ti lamellar eutectic phase (see Fig. 4.3b). The presence of these distinct areas is probably the result of the segregation of the species in the sample due to the original NiTi plate being at the top of the SS plate. Moreover, some titanium carbides with highly faceted shape were observed all over the sample: they were embedded in the eutectics, but not in the primary phases.

The 63% NiTi - 37% SS (B') sample showed the same microstructure as the NiTi-rich side of the 50% NiTi - 50% SS (A') sample, but including another phase present in the middle of the eutectic. The latter phase was identified to have a (Fe,Ni)-Ti structure, which formed finally in the remaining liquid pockets (see Fig. 4.4a). The supposed solidification path is the following: The primary Fe_2Ti dendrites form in the bulk liquid, lowering the iron and titanium concentrations in the remaining liquid. The U_2-E_1

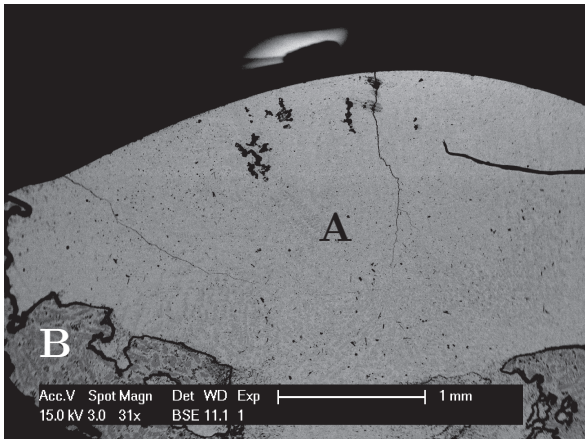

(a) Overview of the 63% NiTi - 37% SS (B') specimen (A = sound region (low carbon content), B = contaminated region (high carbon content)).

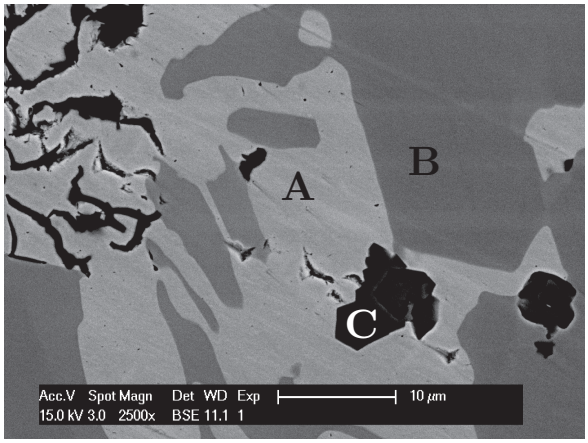

(b) Detail of the contaminated region of the 63% NiTi - 37% SS (B') specimen (A = cementite (Fe_3C), B = austenite (γ-(Fe,Ni), C = titanium carbide).

Figure 4.2: BSE SEM observations and EDX analyses highlighting two main areas in the 63% NiTi - 37% SS (B') infrared specimen. The SS plate (disposed below the NiTi plate) reacted with the graphite crucible during heating. This carbonation reduced the SS amount in the final composition. Few titanium was found in the contaminated areas, this element being concentrated in small titanium carbides.

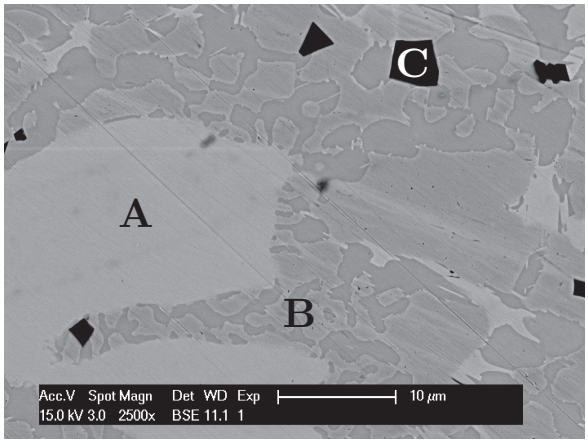

(a) SS-Rich area of the 50% NiTi - 50% SS (A') specimen (A = primary γ-(Fe,Ni), B = eutectic (γ-(Fe,Ni) - Ni_3Ti), C = titanium carbide).

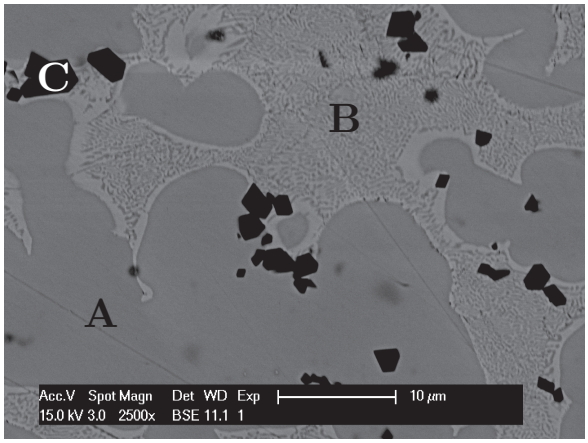

(b) NiTi-Rich area of the 50% NiTi - 50% SS (A') specimen (A = primary Fe_2Ti, B = eutectic (Fe_2Ti and Ni_3Ti), C = titanium carbide).

Figure 4.3: BSE SEM observations and EDX analyses highlighted two main areas in the 50% NiTi - 50% SS (A') infrared specimen. Primary phase (A) was surrounded by a eutectic structure (B), which embedded some titanium carbides (C).

Specimen name	A	B	C
Intended compositions	25% NiTi 75% SS	50% NiTi 50% SS	75% NiTi 25% SS
Measured compositions	50% NiTi 50% SS	63% NiTi 37% SS	75% NiTi 25% SS
	A'	B'	C'

Table 4.1: Infrared controlled solidification samples encountered composition changes due to carbide formation in the SS base materials before melting. Intended compositions were shifted towards higher NiTi concentrations.

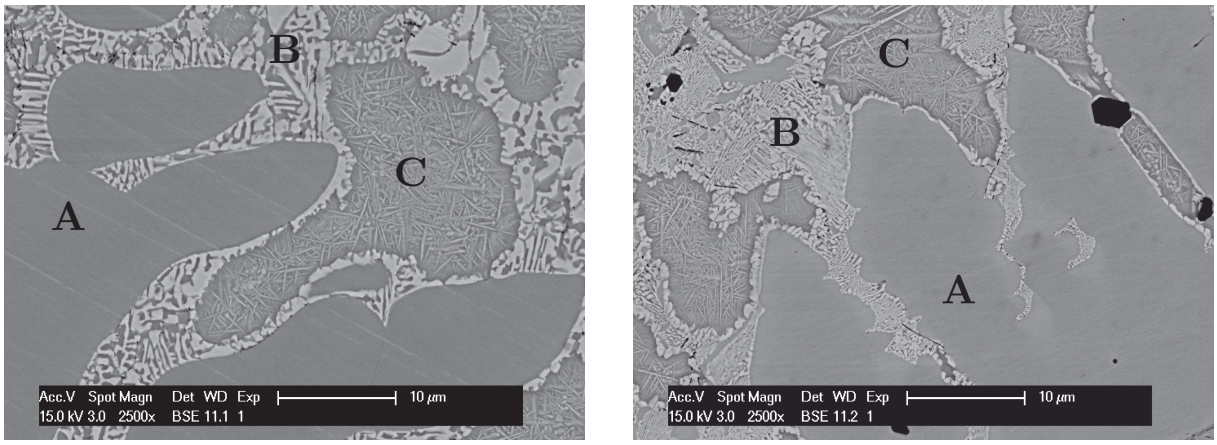

(a) 63% NiTi - 37% SS (B') specimen. **(b)** 75% NiTi - 25% SS (C') specimen.

Figure 4.4: BSE SEM observations, coupled to EDX analyses of the NiTi-rich samples (B' and C'), showing the (Fe,Ni)-Ti phase with a needle-like structure (A = primary Fe_2Ti, B = eutectic (Fe_2Ti and Ni_3Ti), C = (Fe,Ni)-Ti).

monovariant line is then hit on the U_2-side of its saddle-shape, forming the surrounding eutectic (Fe_2Ti and Ni_3Ti). The final liquid solidifies along the U_2-e_3 line with (Fe,Ni)-Ti and Ni_3Ti formation.

The last infrared specimen of interest (C'), with the nominal and final composition of 75% NiTi - 25% SS, had a similar microstructure to the previous one (B') (see Fig. 4.4b). The liquidus projection predicts a microstructure composed of (Fe,Ni)-Ti and Ni_3Ti. However, SE observations and EDX analyses revealed the presence of the Fe_2Ti phase in several locations. This can result from inhomogeneities in the molten sample, errors in the available phase diagram, or kinetics effects for the different phase formation. Nevertheless, this indicates a nucleation advantage of the Fe_2Ti phase, which formed in all samples, even at compositions for which the available phase diagram does not predict it.

The compositions measured by EDX were difficult to accurately define on the ternary phase diagram due to the presence of a fourth element: chromium. Indeed the lack of information about chromium effect on the stability domains of the phases widened the error of chemical measurements. Thus, EBSD identification of the phases was performed to validate the solidification paths explained previously for each sample. However, mapping were impossible to obtain due to the fine microstructure, smaller than the spatial resolution of the technique (around 1 µm), so only point identifications were performed.

These infrared experiments revealed that the mixing ratios of NiTi and SS with high NiTi content always lead to the formation of Fe_2Ti dendrites as a primary phase. As many of the expected concentrations inside dissimilar NiTi-SS laser welds exhibit high NiTi contents, the Fe_2Ti phase will thus be present. According to literature, the latter is a brittle intermetallic phase and should be avoided to reach sound welds. Thus, the welding experiments have to be designed in such a way so as to have a higher SS content to reduce the formation of this phase. This was done by moving the beam towards the SS wire side in order to reduce the titanium concentration of the weld pool.

4.2 Bridgman Furnace

This section summarizes the Bridgman solidification furnace experiments. The aim is to make correlations with the unconstrained growth experiments discussed above (infrared furnace experiments), as both solidification experiments were done at about the same cooling rate. Three different mixing ratios were investigated in the Bridgman furnace: 75% NiTi - 25% SS, 50% NiTi - 50% SS, 25% NiTi - 75% SS. Almost no carbide formed in the samples, keeping the final compositions of the samples as expected. Microstructure observations were made using a Reichert© optical microscope with polarized light (see Fig. 4.5).

All the samples showed a dendritic structure developing along the thermal gradient, in the adiabatic zone of the Bridgman furnace. In this region, experimental data showed that the thermal gradient (G) was between 20 and 25 $K\,mm^{-1}$. Fig. 4.5 shows the three specimens at specific NiTi-SS ratios. Labels A and B correspond to the position of the dendrite tips and eutectic front, respectively. The lack of accuracy in sample positioning ($\pm$ 1 mm) generates an error in temperature determination (around 50 °C), which makes the correlations with the ternary phase diagram difficult. However, the solidification interval, which does not depend on the positioning accuracy ($\Delta T = G \times \Delta x$, which is precisely measured on the micrograph), was below 100 K, in the three different samples.

The area at the eutectic front position of the 25% NiTi - 75% SS specimen showed

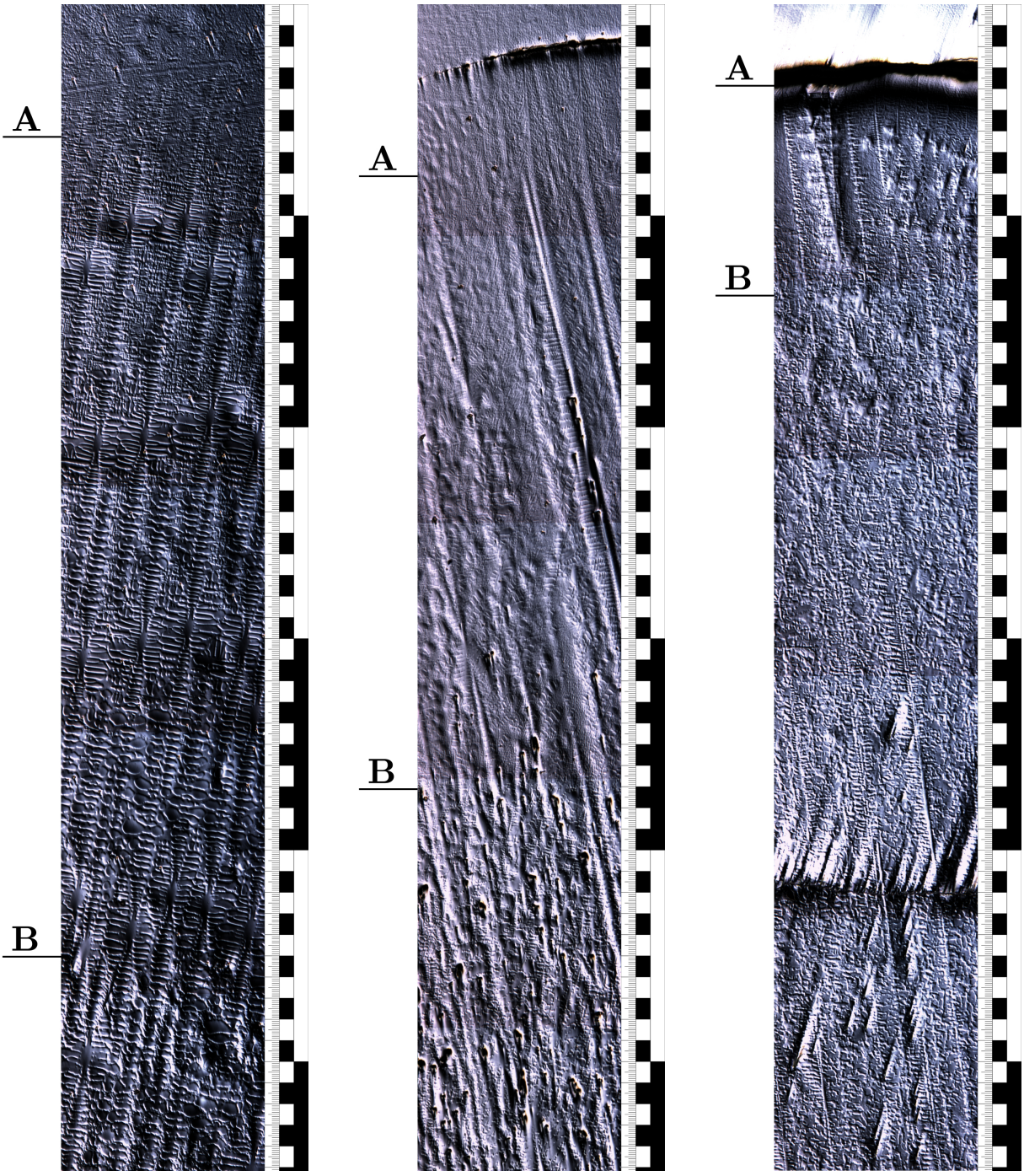

(a) 25% NiTi - 75% SS. **(b)** 50% NiTi - 50% SS. **(c)** 75% NiTi - 25% SS.

Figure 4.5: Quenched Bridgman specimens showing dendritic (A) and eutectic (B) structures at the end of solidification. In the quenched microstructure, the dendrite tips are visible just below the liquidus temperatures (A) and the final solidification of the liquid occurs at the eutectic temperature (B). The three different samples were produced with the same conditions (vertical thermal gradient $G \approx$ 20-25 $\mathrm{K\,mm^{-1}}$, pulling speed $v = 500\,\mu\mathrm{m\,s^{-1}}$). The main scale (long block lines) corresponds to 1 mm.

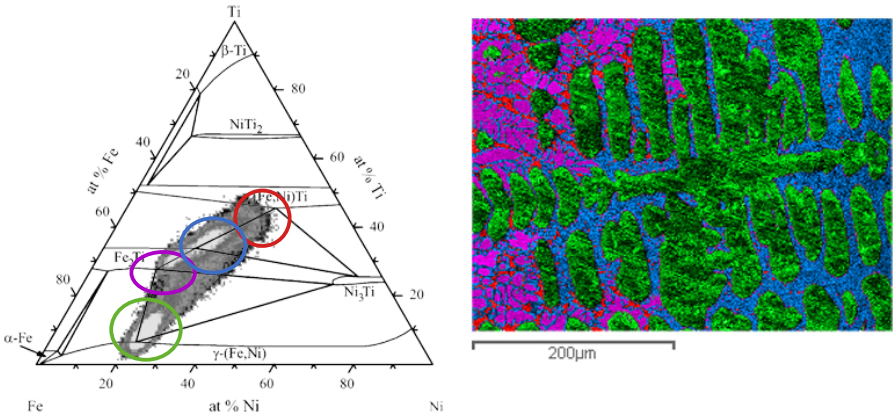

(a) 25% NiTi - 75% SS.

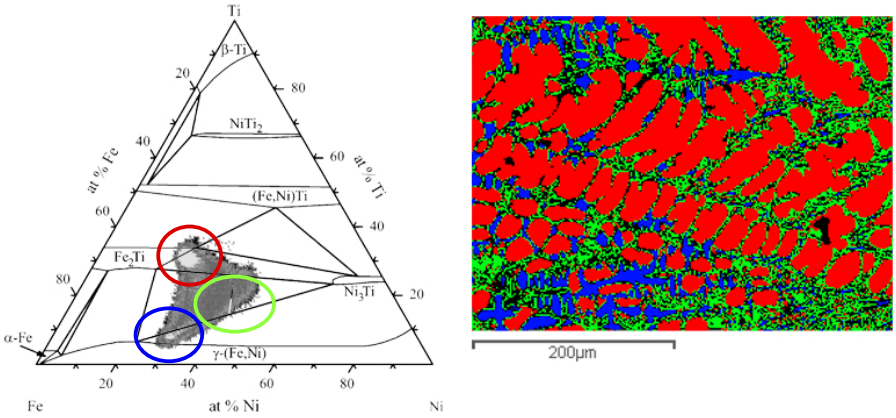

(b) 50% NiTi - 50% SS.

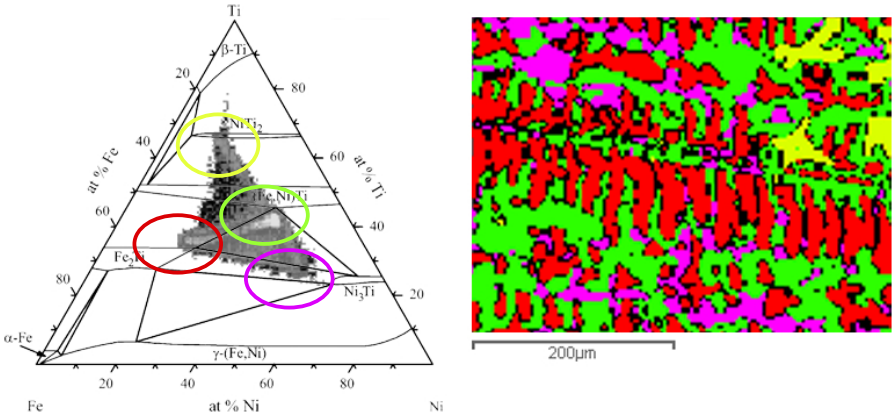

(c) 75% NiTi - 25% SS.

Figure 4.6: EDX chemical analyses of the Bridgman solidification samples emphasizing the primary and surrounding eutectic phases. On the left side, the Fe-Ni-Ti isothermal cut at 900 °C is superimposed to the intensity contour plot of the EDX measurements (chromium is not represented but taken into account during quantification). Indeed, the deconvolutions of the EDX spectra were done with four elements, but only the three principal ones are represented. Compositions of interest are circled with a color corresponding to the locations on the BSE micrograph (right side). The EDX mapping were performed over a 512×380 grid area during 8×10^4 s, with an indexed count rate of 4×10^3 cts s^{-1}. The analysis was performed at 15 keV without standards, using a "site lock" option to ensure positioning accuracy during the whole data acquisition.

primary γ-(Fe,Ni) dendrites embedded in the quenched liquid (see Fig. 4.6a, green and blue areas, on the right of the micrograph). During solidification, this liquid transformed into a eutectic structure of Fe_2Ti and (Fe,Ni)-Ti, in between the primary dendrite skeleton (pink and red areas). This composition was not observed in the infrared solidification experiments because of the reaction with the crucible, but Fe_2Ti brittle phase is still present at high SS mixing ratio in the eutectic structure.

Comparatively to the previous Bridgman sample, the 50% NiTi - 50% SS specimen has an inverse solidified structure, meaning that Fe_2Ti primary dendrites developed first (see Fig. 4.6b, red areas on the micrograph). The interdendritic liquid solidified as a binary structure made of γ-(Fe,Ni) and Ni_3Ti (see Fig. 4.6b, green areas on the micrograph). The γ-(Fe,Ni) phase had a larger size and is visible in blue on the micrograph, but Ni_3Ti is too fine to be resolved in SEM EDX and appeared averaged with γ-(Fe,Ni) phase. This is also the reason explaining that the frozen liquid seems to have an average composition in between those of the individual phases composing the eutectic. Thus, compared to the 25% NiTi - 75% SS specimen, this sample composition is actually across the U_1-E_1 monovarient line, which was predicted by the liquidus projection.

These two first samples exhibit an extended dendritic structure compared to the last specimen, which had the highest NiTi mixing ratio (75% NiTi - 25% SS). This small primary phase fraction and the corresponding short solidification interval are both hints about the proximity of the initial composition to a monovarient line of the liquidus projection. Indeed, the primary phase propagates with a dendritic structure between A and B before the eutectics starts to form. This reduces the maturation of the structure, thus reducing the secondary dendrite arms spacing. The chemical analyses of the specimen showed primary Fe_2Ti dendrites, which was unexpected at this composition (see Fig. 4.6c, red areas on the micrograph). According to the Fe-Ti-Ni liquidus projection, the primary phase should be (Fe,Ni)-Ti or Ni_3Ti. However, the chromium effect is not well known and could result in a Fe_2Ti primary phase enhancement. Nevertheless, both of these phases were highly present in the solidified interdendritic solid (Ni_3Ti in purple and (Fe,Ni)-Ti in green). Observed $NiTi_2$ composition was made in areas corresponding to the dendritic structure, which had then decomposed in the solid state, likewise during a peritectic reaction (yellow zones on the micrograph).

4.3 Summary

The observations of these infrared and Bridgman specimens showed the omnipresence of the Fe_2Ti brittle intermetallic phase in every mixed composition. This phase seems to have a low nucleation cost and develops rapidly in the microstructure, either in constrained or unconstrained growth. Laser welding experiments should not except this rule, despite the much higher thermal gradient and cooling rate, and their corresponding microstructures are likely to show the same phase. The range of solidification speeds investigated does not affect the phase formation and the system is fairly well described by the Fe-Ni-Ti ternary phase diagram.

Chapter 5

Laser Welding

This chapter focusses on the experimental results relative to the final application of the project, which was to achieve sound welds between 300 µm diameter wires of NiTi and SS. All reasonable parameter options are discussed and detailed in chronological order (according to successive findings from prior experiments).

5.1 Preliminary Welds

As described in the corresponding experimental section (see section 3.1.1), preliminary experiments were made on massive samples. This planar geometry was used to simplify the experiment to its maximum. Plate welding is easier to investigate than wire welding, because accurate positioning and laser beam motion are simpler.

A first batch of laser remelting experiments were conducted on both materials of interest (NiTi and SS). The investigated parameters were the laser beam power, the pulse duration, the beam motion speed and the frequency of pulses. However, it became rapidly evident that the minimal power delivered by the 1 kW Nd:YAG laser of LSMX available at the beginning of this study was still too high for a direct correlation with wire welding experiments. The minimal power using a 50% Beam Splitting (BS) produced a surface remelting spot or bead with the focal diameter size (300 to 600 µm), being much more than acceptable size for 300 µm diameter wire welding. Moreover, these remelting spots had a maximal depth of 100 µm, which would not be sufficient to reach the center of the wire.

Autogenous welding experiments were thus conducted to find the energy density necessary to reach the transition from conduction to keyhole welding mode to reduce width over penetration depth ratio of the laser spots. Nevertheless, the optimal parameters were found to be around a power density of 1 kW/mm^2 and a duration of pulse below 2 ms in order to avoid cracking in pure NiTi beads. Indeed, higher power density lead to the formation of cracks in homogeneous remelting experiments, which were observed to propagate perpendicularly to the isotherms in NiTi. These cracks result from hot tearing at the end of microstructure solidification. The use of pulse shaping, in order to reduce cooling rate, did not avoid crack formation and propagation in autogenous NiTi remelting beads.

Finally, the frequency of pulses and the sample motion speed were not an issue, but needed to be adjusted to ensure a continuous weld bead with a sufficient overlapping between each laser spot.

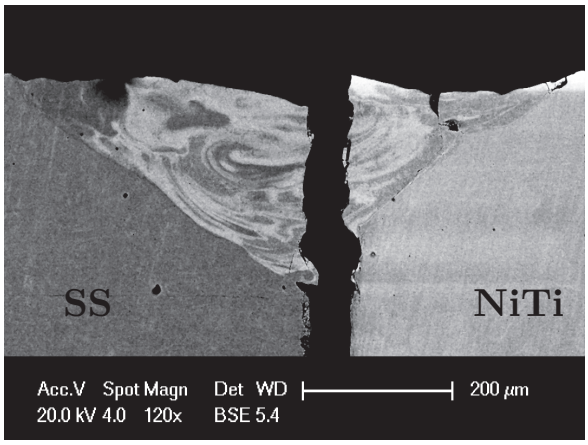

(a) SEM BSE image of a cross-section made in a dissimilar weld trial showing both NiTi and SS base materials and the weld area.

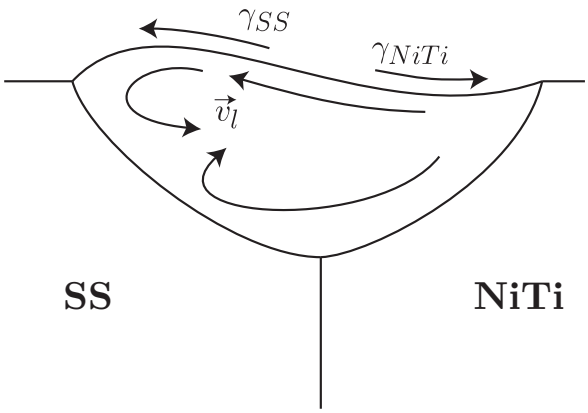

(b) Scheme of the convection flows ($\vec{v_l}$) that are visible on the left BSE image. They result from Marangoni convection due to the lower surface tension of liquid NiTi (γ_{NiTi}) than that of SS (γ_{SS}).

Figure 5.1: Dissimilar weld trial showing mixing in the weld pool between NiTi and SS base materials. The density contrast emphasizes the Marangoni convection flows, that occur during welding and resulting in composition inhomogeneities across the weld pool.

Heterogeneous weld beads were performed between NiTi and SS 1.5 mm thick plates, in the same preliminary setup. None of the trials resulted in sound welds or even sufficient mechanical strength to sustain handling of the specimen. However, these broken samples gave information about chemical compositions and microstructures of the welded zone (see Fig. 5.1). Chemical quantifications showed higher amounts of iron and chromium, with a composition closer to SS than NiTi, in dark zones (see Fig. 5.1a). Moreover, Marangoni convection flows are visible in the frozen weld from the shape of SS-rich dark, and NiTi-rich bright zones. Even if the global direction of flow seems to be clockwise in the weld, the flow at the surface seems to go from NiTi to SS as indicated by the overall surface shape. This complex flow is schematized in Fig. 5.1b. It is expected as the surface tension of liquid SS is higher than that of NiTi, the surface tension being scaled usually with the melting point. This displacement of the surface towards SS plates leads to complex flows inside the bath and a fairly homogeneous composition of the weld (all analysed elements were found in every location of the weld).

5.2 First Design of Experiments

As summarized in the theoretical part, two main designs of experiments (DoE) were used to optimize the welded samples Ultimate Tensile Strength (UTS). First, the Fractional Factorial Design (FFD) was used to screen a large number of laser parameters. Then, a Central Composite Design (CCD) was planned with a reduced number of parameters, not only according to the prediction of the first model, but also by considering the observations made on the first DoE specimens.

The large number of experimental sets required for a Full Factorial Design as first Design of Experiment (with seven parameters: $N_{exp} = 2^7 = 128$) lead to the use of generator to reduce the number of runs to $2^4 = 16$ (a two level Fractional Factorial Design $2_{\mathrm{IV}}{}^{7-3}$, see App. A).

The seven parameters were chosen initially as follows:

Pos is the parameter representing the central position of the beam. The "0" position corresponds to the beam centred at the interface between the two wires and "-50" means the beam hits 50 µm on the SS wire.

t_p is the pulse duration expressed in ms.

PPP for Pulse Peak Power is the maximal power delivered by the laser beam during each pulse, in kW. The main interest is to have independent parameters and thus *PPP* was modified to keep the mean pulse power constant. Therefore, *PPP* was doubled whenever the Pulse Shape was sinusoidal and not rectangular. Indeed, the energy being the integral of the power over the pulse duration, it is highly dependent on the pulse shape. As the sinus shape is half the area of a rectangular shape, the PPP was adjusted with a factor two.

f is the frequency of repetition of the pulses during the weld, expressed in Hertz.

PS defines the used pulse shape, either "Top-Hat" (Rect) or "sinusoidal shape" (Sinus).

I is a parameter which describes the path followed by the laser beam during the weld. The choice of the different paths was made due to the sensitivity of laser welding to "hot tearing" (see section 5.1). As each pulse remelts part of the previous one, the only remaining cracks are the ones behind the beam spot. So, two paths were experienced, a standard circular one and another following a sine wave trajectory along the SS-NiTi interface during the rotation of the wires, in order to limit the progression of cracks in the bead. The parameter I is the half-amplitude of the sine wave, expressed in microns.

V is the wires rotation speed, expressed in rotation per minutes (RPM).

The main measured response was the UTS in [MPa] of the welded couple while tested in traction at 0.5 mm/ min rate. The length of the tested specimens was 200 mm, thus the average deformation speed was: $\dot{\varepsilon} = \frac{0.5\,\mathrm{mm/\,min}}{200\,\mathrm{mm}} \times \frac{1}{60} = 4.2 \times 10^{-5}\,\mathrm{s}^{-1}$. In Table 5.1, the value expressed in the column called "UTS" is the mean of 10 samples measured for each set of parameters. The next columns are the depth and width of the weld pool observed on a transverse section. As the depth is non-linear due to the cylindrical shape of the wires, and the widening depends on the focal diameter of the beam, mainly the UTS was taken into account.

5.2.1 Effects and analysis

The influence of each laser parameter on the resulting tensile strength (UTS) can be modelled. The effects of each parameter have to be determined by multiplying the transpose of the Experiment Matrix by the resulting vector (UTS), as detailed in the theoretical part A.1.4. Fig. 5.2a represents the “Lenth” graph, that shows the impact of each parameter on the final strength of the joint. A positive/negative impact indicates that the parameter has to be maximized/minimized to improve the UTS of the joint, whereas near zero the parameter has almost no effect.

As several couples were not welded at all, some sets of parameters result in a zero value in the UTS column. Thus, information was lost during this DoE. The positioning of the

	Pos	t_p	PPP	f	PS	I	V	UTS	$Depth$	$Width$
Units	μm	s	kW	Hz	-	μm	RPM	MPa	μm	μm
Parameter #	1	2	3	4	5	6	7	-	-	-
D01	0	0.5	0.04	30	Rect	0	30	0	0	0
D02	-50	0.5	0.08	30	Sinus	0	60	0	0	0
D03	0	2.5	0.08	30	Sinus	50	30	172.2	110	220
D04	-50	2.5	0.04	30	Rect	50	60	0	0	0
D05	0	0.5	0.16	30	Sinus	50	60	0	250	210
D06	-50	0.5	0.08	30	Rect	50	30	0	110	150
D07	0	2.5	0.08	30	Rect	0	60	421.1	300	210
D08	-50	2.5	0.16	30	Sinus	0	30	352.0	300	1000
D09	0	0.5	0.04	60	Rect	50	60	0	0	0
D10	-50	0.5	0.08	60	Sinus	50	30	0	0	0
D11	0	2.5	0.08	60	Sinus	0	60	376.5	170	210
D12	-50	2.5	0.04	60	Rect	0	30	0	0	0
D13	0	0.5	0.16	60	Sinus	0	30	293.3	110	150
D14	-50	0.5	0.08	60	Rect	0	60	136.6	75	150
D15	0	2.5	0.08	60	Rect	50	30	0	0	0
D16	-50	2.5	0.16	60	Sinus	50	60	0	0	0
D17	-25	1.5	0.06	45	Rect	0	45	439.6	75	150
D18	-25	1.5	0.06	45	Rect	0	45	423.8	75	150
D19	-25	1.5	0.06	45	Rect	0	45	385.1	75	150
D20	0	0.5	0.16	30	Rect	50	60	452.6	250	210

Table 5.1: List of parameters for each experiment done during the first dataset, the three last columns are the responses, mean value of UTS testing performed on 10 couples for each set (MPa), observed liquid pool depth and width (μm).

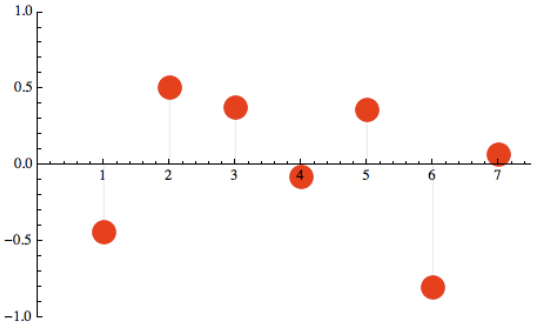

(a) Characteristic "Lenth" graph showing the main effects of each parameter, labelled by their corresponding numbers (see Table 5.1). The vertical axis value gives the influence of each parameter (positive or negative impact).

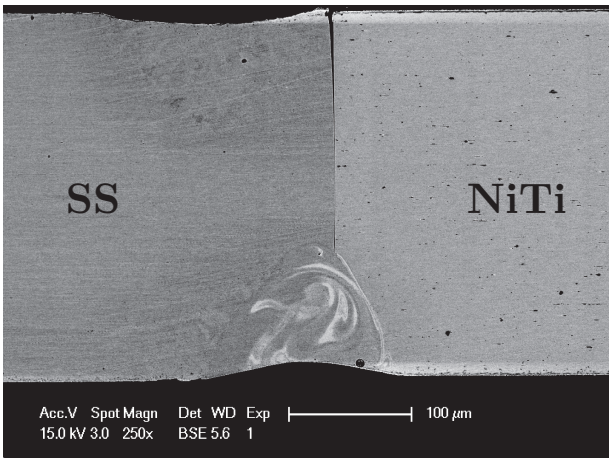

(b) Dramatic consequence of parameter #6 (trajectory of the laser beam). The lateral displacement is too important and no welding happened at the top of the transversal cut (autogenous SS remelting is visible).

Figure 5.2: The Lenth graph highlights the main effects of the parameters, but hidden defaults in the DoE planning bias the conclusions.

wires was also troublesome, as some wire couples have been misaligned before welding. A special care was taken in the second DoE to avoid these problems, and thus only the main primary effects were taken into account here.

Based on this experimental set and its analysis, the following observations and conclusions can be made:

- The sixth parameter (laser path itinerary) had a very negative impact. This can be explained by the semi-amplitude of the sine wave, which has a size similar to the focal diameter. When the beam was positioned mainly on the SS wire, the molten pool did not touch the NiTi wire at the maximum of the oscillation and produced incomplete welding of the perimeter (see Fig. 5.2b). Moreover, also due to inertia of the mobile laser head, five waves maximum could be reached per rotation, so the reduction of the "hot tearing" tendency was negligible. Thus, this parameter had to be avoided for the central composite design, as it leads to partial welding of the joined couple. The latter problem is highlighted by transversal cut of the weld (see Fig. 5.2b), showing that the SS wire is molten in the upper part of the cut, but no reaction with NiTi has occurred. As this parameter has obviously a very negative impact, it was set to its minimal value, which is "0", meaning that no oscillations are made (circular path). This is the reason why this parameter is not investigated further in the following DoE.

- By decreasing impact order, the second factor (pulse duration) showed a high influence on the UTS. This parameter was kept for the central composite design, as it is one of the most important parameters in laser welding, describing the repartition in time of the energy, once the power of the laser beam is fixed. However, the huge gap between maxima and minima had to be reduced, to avoid oscillations between the plasma state and conduction mode, with no stable intermediate state.

- The first factor (position of the beam) has a negative effect, which means that the preferential positioning on the SS wire seems to have a negative influence over the resulting strength. Nevertheless, similarly to the sixth parameter, positioning on the SS wire is too far from the interface (half the focal diameter), therefore the values had to be evaluated again over the following DoE. Keeping this parameter is nevertheless important as it influences the mixing ratio of SS and NiTi, which was shown to have a major effect on the phase formation, and thus on the UTS (see previous sections).

- The third factor (PPP, the Pulse Peak Power) was also kept for the second DoE as it is a key parameter of laser welding since it defines with the pulse duration the energy input in each pulse. Moreover it shows a strong effect on the weld strength (UTS).

- The fifth factor, representing the pulse shape, was dropped, even if it has a strong effect on the UTS, due to the multiple interactions between the pulse peak power and the duration, leading to large variations in energy input.

The two last factors (#4 frequency and #7 velocity) have low impact over the UTS, as each pulse of maximum 2.5 ms leaves about five times this duration to the weld pool to solidify before the next one and thus interactions are really low between pulses. The rotation speed has no physical effect over the energy repartition or the penetration depth, but influences the superimposition of the laser spots. Thermal simulation (see figure 5.5) showed that the temperature at the center of the interface was slightly raised but reaches a steady state after a few pulses (see section 5.3).

The main information given by this DoE was the narrow window leading to sound welded couples. Artificially low UTS were induced by partial welding of the wire interface, which lead to non-welded area inside the weld, reducing the effective surface sustaining stress during tensile testing. Moreover, a sinusoidal shape of the laser itinerary emphasized this latter issue, as some positioning of the laser beam missed the NiTi wire (see Fig. 5.2b).

5.2.2 Fracture analysis

As discussed above, most of the sample sets realized in this first DoE led to disjoint specimens, caused by either an excess or a lack of welding energy. Such specimens were not tested and mainly broke while positioning in the tensile tester, but longitudinal cross-sections had been prepared on most of them, showing partial welding (see sample from set D06 on Fig. 5.2b). However, among tested joined samples, several ones exhibit a wide distribution of UTS even for the same conditions (see Fig. 5.3), and others had a low UTS. The latter ones were associated with partial welding with a remaining untouched surface in the center of the wires. This was for example the case in the sample sets D03 and D14.

The sample sets with a wide UTS distribution, such as D08 and D13, showed brittle fracture across the welded area, but also sometimes contained shrinkage porosity. For instance, the sample set D08 showed this type of porosity in some specimens, but not all (see Fig. 5.4a). In Fig. 5.4b and 5.4c, no porosity was visible and a perfectly brittle fracture was observed.

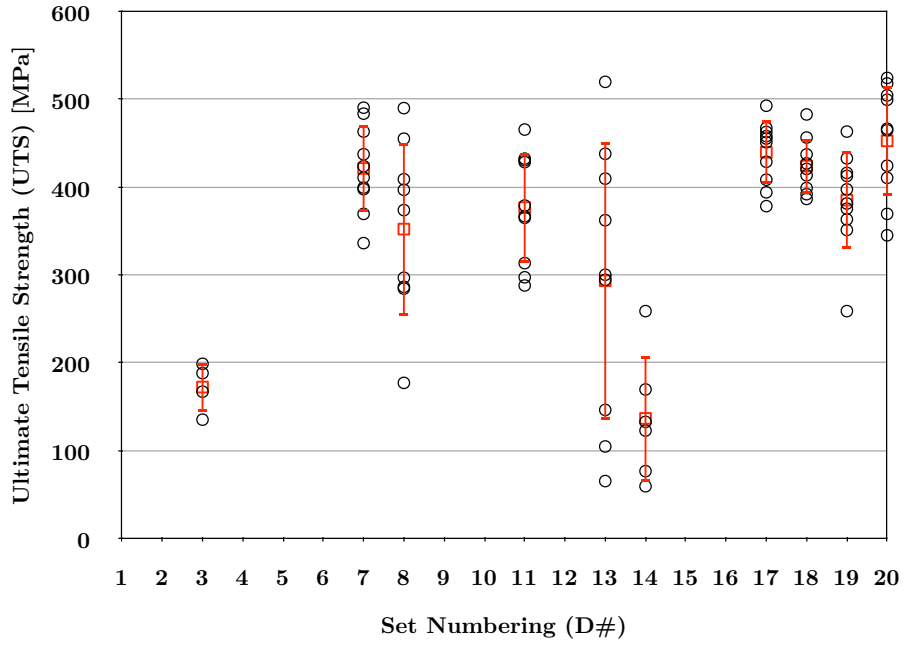

Figure 5.3: Ultimate Tensile Strength (UTS) of the dissimilar laser welded wire couples from the first Design of Experiments performed at HERAEUS using a pulsed laser. Each circle stands for a measurement and the red squares are the mean values with their standard deviations. The horizontal axis represents the laser parameter set numbering (see Table 5.1).

5.3 Weld pool thermal modelling

After these first results, thermal calculation was realised in order to confirm that frequency of pulses and wire rotation speed had a low impact on the weld thermal history. Thermal calculation was done using Calcosoft© from the ESI Group [97], to model the heating of the wires during pulsed laser welding. Several trials were done to find the minimal size of the modelling domain to avoid boundary effects and the finite elements sizes. The laser beam was taken as a surface heat source orbiting around the domain, with the laser beam parameters used in a standard sample welding. Both NiTi and SS wires were modelled using their own properties, which were taken in the Smithells Metals Handbook [98]. No convection was implemented, but the liquid thermal conductivity was increased to model the system more realistically.

The main purpose of these calculations was to determine the thermal history of the specimen during welding. Indeed, the influence of a laser pulse on the material and the cooling time has to be understood to know the importance of the frequency of pulses as a laser welding parameter. Fig. 5.5 shows the final results used to corroborate the pulse frequency influence on the global heating of the wires. The modelling domain was extended to two discrete cylindrical domains (SS and NiTi wires), with a diameter of 300 µm and a length of 5 cm for each.

On Fig. 5.5a, the effect of the laser pulse is visible on the NiTi wire, while the SS wire is made transparent. The molten pool is dark and the color scale corresponds to the

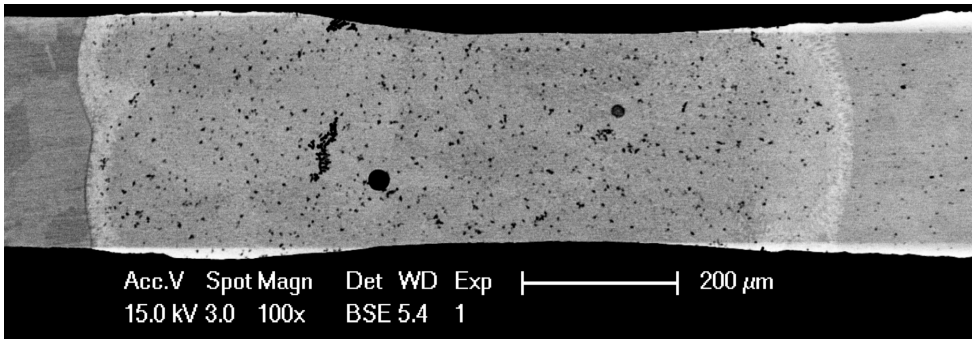

(a) BSE micrograph of a longitudinal cross-section of a specimen from sample set D08.

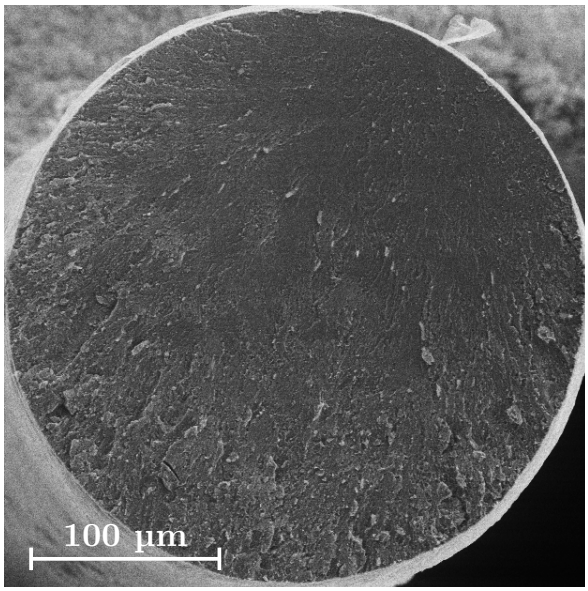

(b) SE view of a fracture surface on the NiTi wire side.

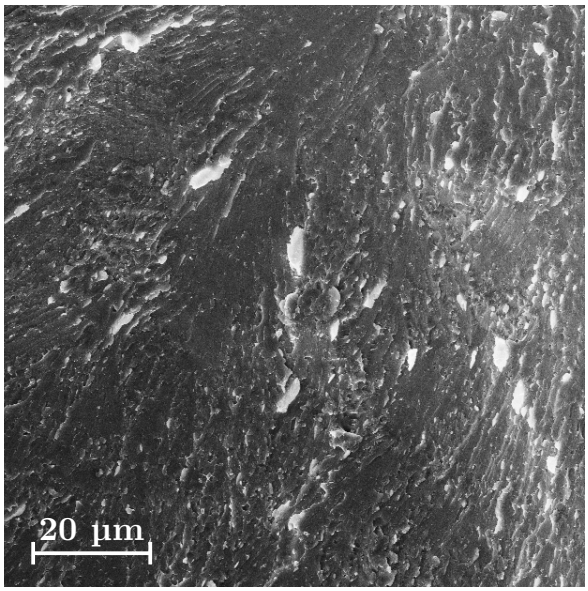

(c) SE detailed view of the same fracture surface.

Figure 5.4: Sample set D08 showing shrinkage porosity of complex shape leading to weak welded joints. Nevertheless, other specimens of the same set had a high UTS with no visible porosity, explaining the wide distribution and standard deviation of the UTS values within the same sample set (see Fig. 5.3).

temperature of the NiTi wire. The contact interface shows a heating of the wire center, considering conduction welding pool only, yet with an increased thermal conductivity to mimic convection.

Fig. 5.5b represents the evolution of the temperature at the centre of the contact interface between the two wires. A global temperature increase occurs in the wires, but the cooling interval between each pulse allows full solidification of the bath. This sufficient cooling time highlights the independence of every pulse during welding, which can thus be considered as single pulse. This observation is important to understand the huge difference between both pulsed and continuous welding, as continuous welding deals with a complete molten interface over the whole welding time. The interaction times are thus very different in the two cases and phase formation and growth are widely affected. Please note that the energy is delivered at the sample surface, thus no convection to keyhole transition is modelled. Thus, the center of the wire remains always solid even using real energy input, as measured experimentally.

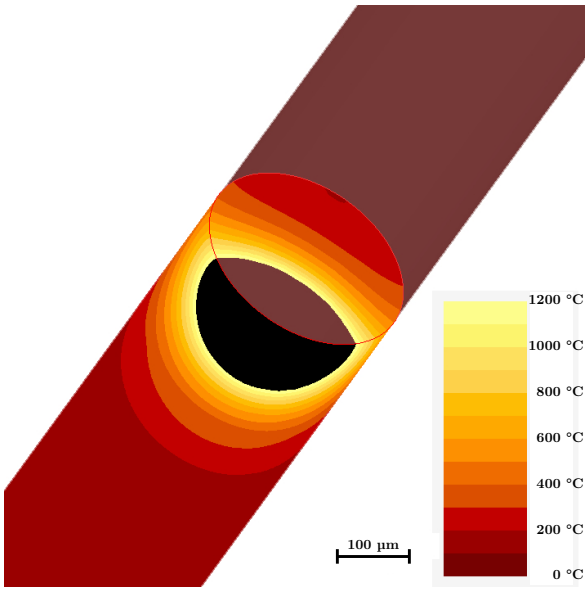

(a) Modelling of temperature during a laser pulse showing the resulting molten pool (dark areas) at the surface and interface. NiTi wire is at the bottom left and SS wire is transparent at the top (brown wire).

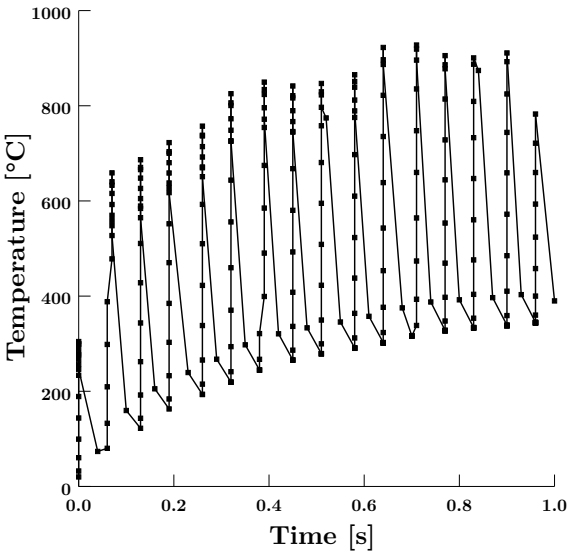

(b) Evolution of the temperature of the central point of the interface shows the effect of pulses over time. A global heating of the wire happens, but remains acceptable to avoid oxidation of the NiTi wire.

Figure 5.5: Modelling of the wire couple was done using two cylindrical domains (300 µm diameter and 5 cm long), corresponding to the base materials wires. The laser was applied as an alternate heat source on the wire surface. The melting temperature was set to 1200 °C, delimiting the conduction pool. Convection was artificially modelled by an increase of the liquid thermal conduction, as no fluid flow modelling was performed.

Another observation is the relatively low temperature encountered between two laser pulses, which is low enough to avoid the rapid oxidation of the NiTi base wire. At steady state, *i.e.* after about 0.8 s of treatment, the base temperature between two pulses is about 350 °C. In continuous welding, oxidation could be an issue as the temperature is higher all over the sample surface for longer durations.

5.4 Second Design of Experiments

The following experimental matrix was designed to develop a quadratic (and a linear) model, using a Central Composite Design (see Appendix A for details on the method). A reduced number of parameters were investigated, according to the observations from the first DoE made on the same orbital pulsed Nd:YAG laser setup of HERAEUS (see Table 5.2). The pulse peak power (PPP) and the pulse duration (t_p) were kept as the only laser intrinsic parameters, but over a narrower range around the medium values of the previous DoE to avoid both extremes. Conduction mode welding biases the results through partial welding while plasma mode vaporizes the material without welding. The third parameter concerns the dilution factor in the weld, using beam positioning across the wires common interface (rectilinear path was followed to reduce the partial welding issue mentioned before).

The first DoE revealed a low impact of the pulse frequency (f) and wire rotation

	PPP	t_p	Pos	f	V	E_{pulse}	UTS
Units	kW	s	μm	Hz	RPM	mJ	MPa
Parameter #	1	2	3	-	-	-	-
E01	0.12	1.8	0	13.9	22.1	193	393.2
E02	0.12	1.8	0	13.9	22.1	193	375.5
E03	0.12	1.8	0	13.9	22.1	193	351.5
E04	0.14	2	20	12.5	19.9	264	374.1
E05	0.14	2	-20	12.5	19.9	263	395.8
E06	0.14	1.6	20	15.6	24.9	201	380.4
E07	0.14	1.6	-20	15.6	24.9	200	409.6
E08	0.1	2	20	12.5	19.9	177	341.7
E09	0.1	2	-20	12.5	19.9	177	446.5
E10	0.1	1.6	20	15.6	24.9	141	383.2
E11	0.1	1.6	-20	15.6	24.9	142	463.1
E12	0.147	1.8	0	13.9	22.1	247	373.9
E13	0.093	1.8	0	13.9	22.1	149	468.2
E14	0.12	2.07	0	12.1	19.2	230	370.6
E15	0.12	1.53	0	16.3	26.	160	387.5
E16	0.12	1.8	27	13.9	22.1	192	422.3
E17	0.12	1.8	-27	13.9	22.1	191	418.4

Table 5.2: Experiment matrix for the second dataset of experiments performed at HERAEUS, with the three investigated parameters (PPP, pulse peak power, t_p, pulse duration and Pos, positioning of the beam with respect to the interface between the two base wires). The frequency (f) and velocity (V) columns are values calculated to have a constant cooling time relatively to pulse duration. E_{pulse} is the energy per pulse (mJ) delivered by the laser unit. The UTS (UTS) is averaged over 5 welded couples tested for each set of parameters.

speed (V), which mainly govern the overlapping of successive laser spots. In this DoE, a constant overlapping (25 µm) was set up, leading to a constant number of pulses required for a weld experiment. Thermal modelling showed a global heating of the wire, but a partial cooling in between them. Thus, the cooling time was set to be 40 times the pulse duration, and the wire rotation speed was adjusted to keep a constant number of pulses ($N = 38$, 25 µm spacing) over a complete rotation. Modelling detailed in the previous section led to the same observation (see section 5.3).

DoE calculations are detailed in Appendix A.2.

5.4.1 Analysis of the model

The first observation was that all the experiments led to successfully welded couples in this DoE (see Fig. 5.6). Narrowing the range of investigated parameters was the result of the previous investigations, which led to these full welded joints without void formation at their center. However, another issue then raised concerning the grouping of laser parameters since small differences between the sample UTS was observed. Almost all samples in this new DoE had a UTS in the range of 350 to 450 MPa.

Modelling of the results through a classical variance analysis (ANOVA, see App. A.1.4) shows a tiny and insignificant change between the use of a linear or a quadratic model, as shown in Table A.6. Indeed, the zero-order coefficient c_0 remains constant and high, when

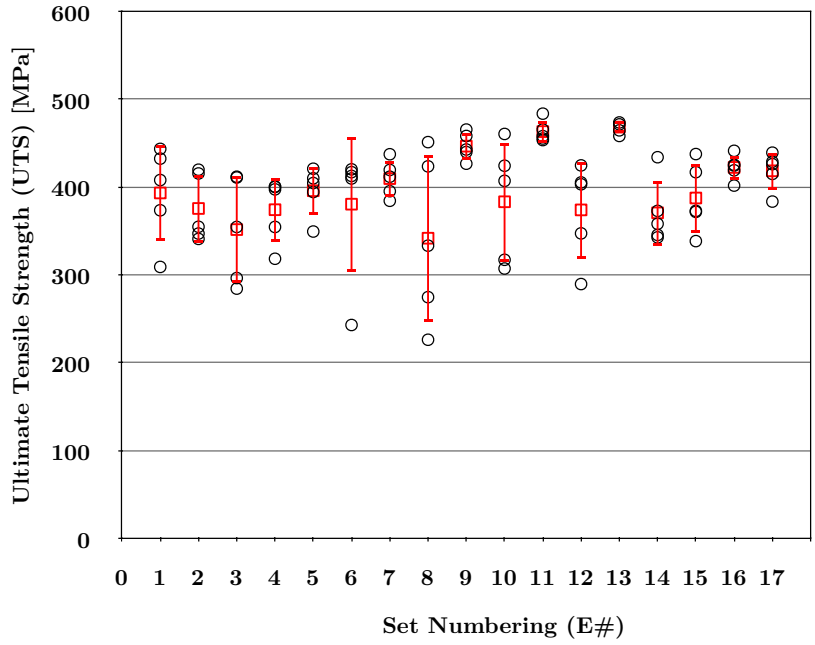

Figure 5.6: Ultimate Tensile Strength (UTS) of the dissimilar laser welded wire couples from the second Design of Experiment performed at HERAEUS using a pulsed laser. Each circle stands for a measurement and the red squares are the mean values with their standard deviations. The horizontal axis represents the laser parameter set numbering (see Table 5.2).

profiling the experiment using both models, according to the other coefficients, which were quite small. Higher order coefficients of both models are constant and thus, the use of the quadratic model had no real justification. However, first-order coefficients are all negative, which can give some hints of the best laser welding parameters. The factor c_1, corresponding to the laser power, leads to the idea of minimizing the input power. The second factor (c_2) is less important, but also leads to a pulse duration reduction. These first two negative factors mean that the laser input energy ($E = t_p \times PPP$) has to be minimum, while still being enough to melt the center of the wires during a pulse. This is clearly visible in Fig. 5.7.

The specimens welded with the highest energy (*i.e.*, highest energy per pulse since the number of pulses in a weld is constant) are sample sets E04 and E05. As shown in Fig. 5.7a, several voids resulting from either gaseous phase trapped during solidification, or solidification shrinkage (see section 2.2.7) are visible in the welds. This visible shrinkage porosity at the bottom centre of Fig. 5.7a lowers significantly the UTS, as it acts as a preferential crack nucleation site with a stress intensification at the void tip. The high energy involved in welding such samples also widens the joint length to more than 0.5 mm, which is twice the size of the sample set exhibiting the highest UTS (E11, see Fig. 5.7b). The latter has a welded area length smaller than the wires diameter at the perimeter, and around 100 µm at the center of the wires. The sinusoidal shape of the interfaces between weld and base wire is more pronounced in the second sample set (E11) than the first one (E04), which may lead to a stress concentration in the outer perimeter of these interfaces

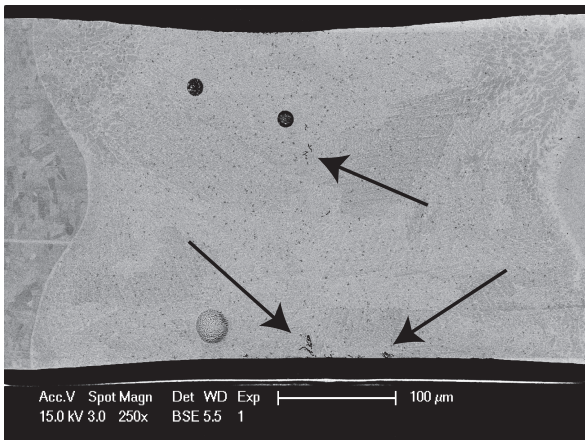

(a) Sample E04, 264 mJ.

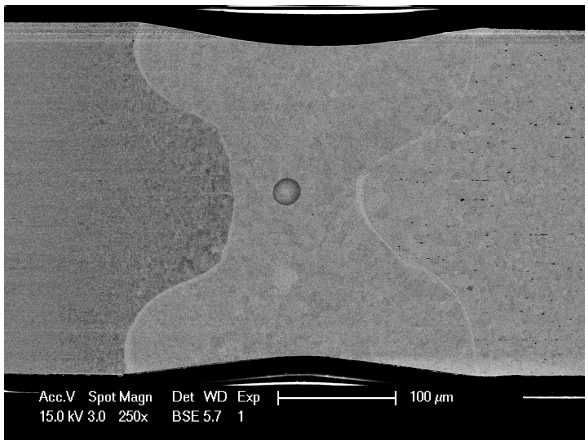

(b) Sample E11, 142 mJ.

Figure 5.7: BSE cross-section view of a welded couple with, (a), the highest and (b) the lowest weld energies. Spherical porosities were often present in sound welded couples, resulting from plasma or vapour trapped in the molten pool while solidifying. Shrinkage porosity with complex shape and high curvature were only found in the high energy welded specimens. Arrows in (a) point out the shrinkage porosities.

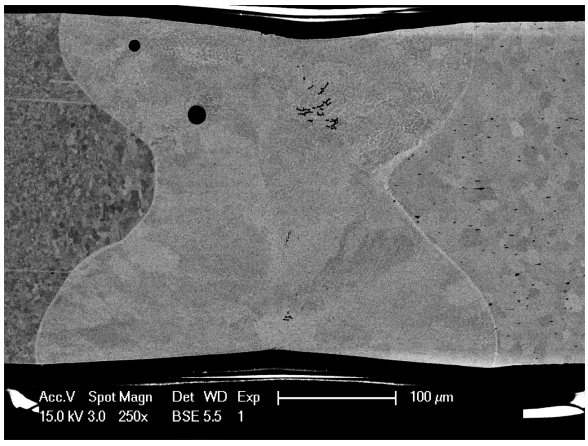

(a) Global view.

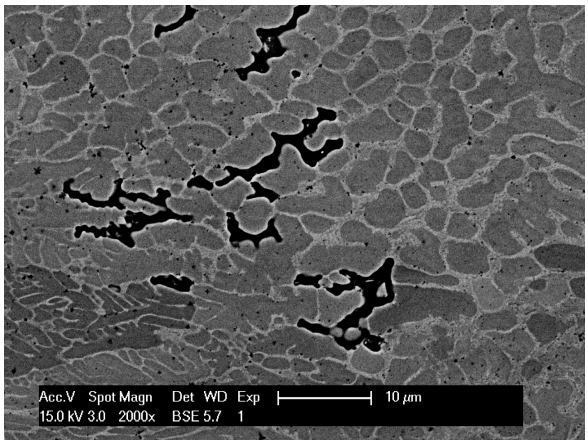

(b) Detailed view.

Figure 5.8: BSE images of a longitudinal cross-section from sample set E03, corresponding to a mid-value parameters of the second DoE.

(see section 6.1.1). In high UTS specimens, spherical porosity was also found, which had a lower impact than shrinkage porosity on the UTS as the curvature is much smaller.

In this DoE, a wide standard deviation is also observed in several sample sets, such as the middle ones (E01-E03, used to check reproducibility), which UTS standard deviations are greater than 50 MPa (see Fig. 5.6). This broadening of the UTS range mainly results from the early failure of some specimens during tensile testing. These early ruptures are observed in samples with high welding energy and SEM imaging shows shrinkage porosity between grains having a dendritic structure (see Fig. 5.8). These defects are located right at the center of the weld, where final solidification occurred, as the heat flux was extracted along the base wires (see Fig. 5.8a). The complex shape of the porosity in this case is interconnected but looks discontinuous in the cross-section, as shown in Fig. 5.8b.

The effect of positioning the laser beam with respect to the base wires contact interface

is difficult to quantify using this DoE (as all the UTS variations between sample sets are within the range of their standard deviation). Nevertheless, the corresponding coefficient, in both the linear and quadratic models, is negative, which justifies a positioning of the beam on the SS base wire (less titanium is then present in the weld pool). The latter observation is consistent with conclusions drawn after the infrared furnace experiments analysis (see section 4.1). However, this has to be carefully done as the bowl shape of the interfaces between welded area and base wires leads to a reduction of the weld length in the core of the wires. In the earlier DoE, this narrowing led to partial welding with a remaining non-welded interface in the center of the wires, and thus lower quality welded samples.

However, this repositioning changes the dilution factor of the species inside the weld pool and increases the proportion of γ-(Fe,Ni) primary phase and thus reduces the amount of brittle intermetallics. Indeed, the controlled speed solidification experiments with a high SS over NiTi ratio (*i.e.* 25% NiTi - 75% SS) showed primary iron-based dendrites with few Fe_2Ti brittle intermetallic phase (see section 4.2).

5.5 Third Design of Experiments

Another DoE was realized on dissimilar NiTi-SS wire welding by HERAEUS at Yverdon-les-Bains. Its purpose was to widen the range of the same parameters used in the previous ones, especially because the resulting welded samples were quite similar (see subsection 5.4.1). The optimal parameters were found to lead to a low energy weld (around 150 mJ/pulse, with a constant spacing between each spot), which is similar to the second DoE performed previously.

The best UTS was found to be equal to 450 MPa, which is the exact superelastic plateau stress limit. Looking at the strain value, some samples have sustained around 4% strain, which corresponds to the superelastic strain (8% elastic deformation) on half of the couple, as the SS wire has no superelastic properties and stands on half the tested length. The latter observation was the initiation point for the *in situ* tensile experiments made in an SEM at EPFL (see subsection 6.1.1).

5.6 Continuous laser welds

In parallel to the pulsed laser welding experiments, a continuous laser setup was used at BREDAM in St-Sulpice, to produce NiTi-SS dissimilar welds and make a comparison with the previous DoE. The studied parameters in this case were the mean power (P), the weld duration (t_w) and the rotation speed (V). The mean UTS was calculated on 5 samples for each set of parameters (see Table 5.3). These parameters are slightly different than those used for the second pulsed laser DoE, as the pulse duration has no meaning in continuous welding. The power and weld duration were used to vary the total energy delivered during the rotations of the wires and the rotation speed determines the number of rotations made during this energy delivery (minimum: $10\,\text{RPS} \times 0.12\,\text{s} = 1.2$ rotation). The rotation speed is much higher than that of pulsed laser DoE experiments (RPS instead of RPM) in order to have a homogeneous weld. Indeed, the weld bath no longer solidifies during welding and thus the energy has to be equally distributed.

The last six sets (A13 to A18) were used as reference to check the reproducibility of the experiments, and showed lower UTS (around 350 MPa) than that of the second

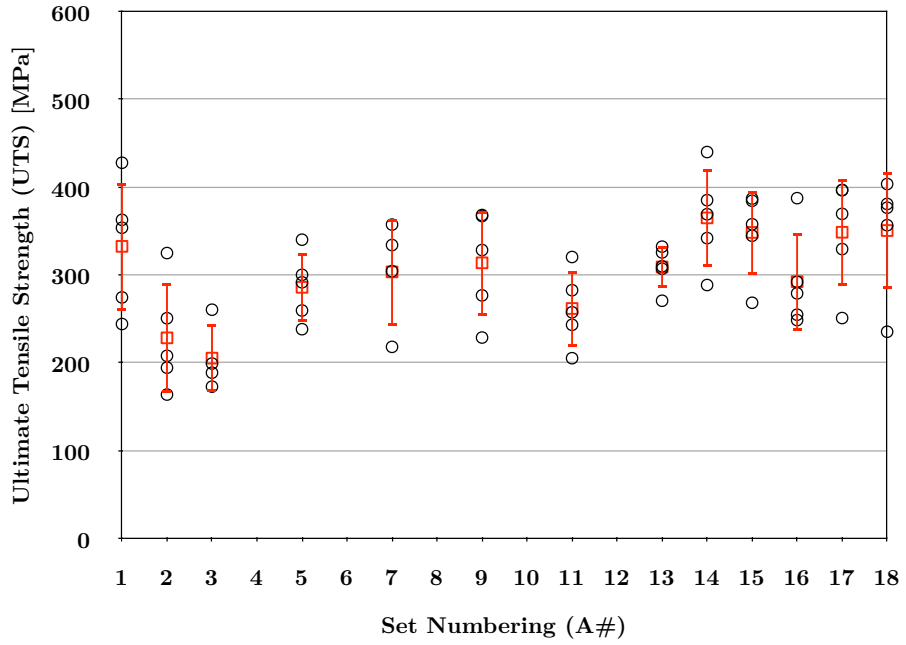

Figure 5.9: Ultimate Tensile Strength (UTS) of the dissimilar laser welded wire couples from the Design of Experiment performed at BREDAM using a continuous wave laser. Each circle stands for a measurement and the red squares are the mean values with their standard deviation. Horizontal axis represents the laser parameter set numbering (see Table 5.3).

pulsed DoE samples. These low values are due to the frequent surface shrinkage porosity observed in these samples, and acting as preferential crack nucleation sites, thus lowering the mechanical properties of the joined couple (see Fig. 5.10). However, not all the reference samples showed shrinkage porosity leading to an early failure, like the toughest specimen in set A14 (see Fig. 5.10a), which had the highest UTS of all the continuous laser welded couples. The latter fracture surface showed a typical brittle failure with clean rupture through the whole section and some delamination of the welded materials in the center. No apparent defect was observed at the perimeter and failure took place at high stress (450 MPa), which corresponds to the exact superelastic stress as mentioned in the previous subsection. As will be shown by the *in situ* tests and by the mechanical modelling (see chapter 6), rupture occurs when reaching the superelastic plateau.

Nevertheless, most of the reference samples showed shrinkage porosity due to lack of liquid feeding in the final step of solidification (see Fig. 5.10b). This porosity was often located at the weld surface (see Fig. 5.10c) as heat is extracted trough the wires and the last place to solidify is near the position of the contact surface of the wires prior welding. As porosity voids nucleate more easily on a free surface, they concentrate near the surface, around half of the weld length. This lack of liquid feeding during dendritic growth leads to complex voids pinched in between the dendrite arms and trunks (see Fig. 5.10d). These high curvature shapes increase the stress intensity factor and act as crack nucleation site leading to an early failure of the specimens.

An important difference between pulse and continuous laser welding to notice is the

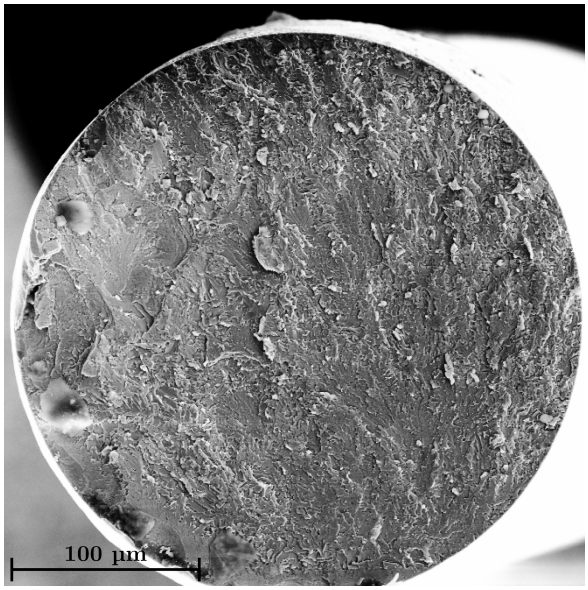

(a) SE image from the fracture surface seen from SS wire side, from the toughest specimen from sample set A14.

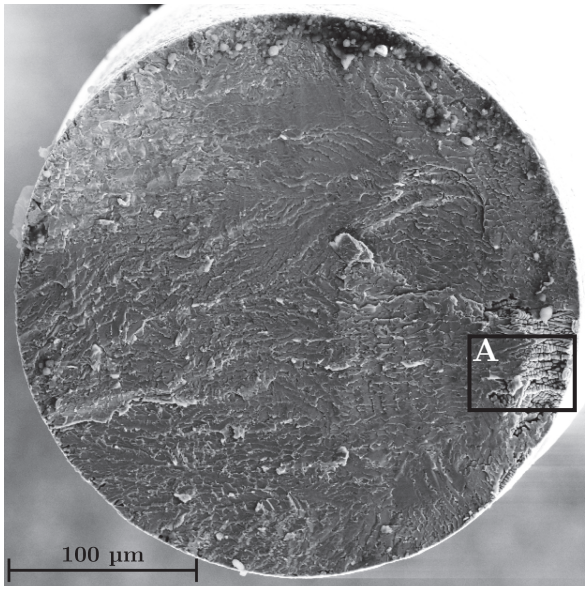

(b) SE image from the fracture surface seen from SS wire side, from the weakest specimen from sample set A18 (Zone A = porosity).

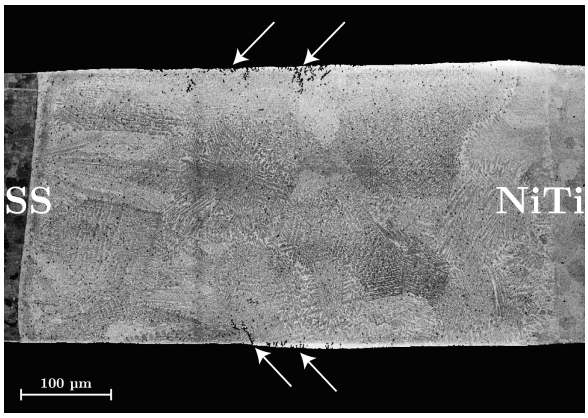

(c) BSE image from a longitudinal cross-section of an untested specimen from sample set A14. Arrows highlight the surface shrinkage porosities

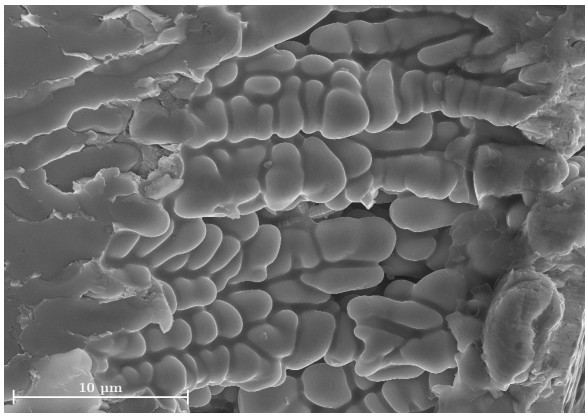

(d) SE image from the shrinkage porosity located in zone A of (b), which acted as a preferential crack initiation site.

Figure 5.10: SEM images from the reference sample set with intermediate continuous laser welding parameters. Surface shrinkage porosities are sometimes observed in bulk welded areas, weakening the joined couple and widening the deviation between maximal and minimal UTS values of specimens with with similar parameters.

	P	t_w	V	E	UTS	$StDev$
Units	W	s	RPS	J	MPa	MPa
Parameter #	1	2	3	-	-	-
A01	15	0.12	15	1.8	332.4	74
A02	25	0.12	15	3	228.2	62.4
A03	15	0.24	15	3.6	205.2	38.3
A04	25	0.24	15	6		
A05	15	0.18	10	2.7	286	39.2
A06	25	0.18	10	4.5		
A07	15	0.18	20	2.7	303.33	60.9
A08	25	0.18	20	4.5		
A09	20	0.12	10	2.4	313.7	60.5
A10	20	0.24	10	4.8		
A11	20	0.12	20	2.4	261.7	43.1
A12	20	0.24	20	4.8		
A13	20	0.18	15	3.6	308.9	23.9
A14	20	0.18	15	3.6	365	55.7
A15	20	0.18	15	3.6	348.3	48.2
A16	20	0.18	15	3.6	292.3	56.0
A17	20	0.18	15	3.6	348.5	61
A18	20	0.18	15	3.6	350.4	66.5

Table 5.3: Experimental matrix of the DoE made at BREDAM using a continuous laser, with variation of the power (P), the weld duration (t_w) and the wire rotation speed (V). The corresponding weld energies (E), mean UTS over five samples (UTS) and standard deviation ($StDev$) are shown in the last columns. The missing values correspond to weld sample sets with an excessive energy that formed molten round ends.

final diameter of the welded area. The small contact force, which was imposed before welding, is accommodated in the case of continuous welding but not with pulsed laser. When the velocity of the continuous laser is fast enough, the weld becomes totally molten and the liquid releases the compressive stress set up when putting the two wires in contact prior to welding. In pulsed welding, each pulse induces melting and solidification occurs before the next pulse. Thus, the stress is never released. This was visible by the observed weld diameter reduction in the case of pulsed welding and the weld diameter increase of the continuous welded samples.

One specimen with a high UTS was surprisingly found in set A01, which had a weld energy insufficient to make a complete welding of the joined couple. The previous pulsed laser DoE specimens showed their best properties at low energy, but with a minimal requirement being to reach the middle of the wires with each spot weld pools. This sample set was observed using a longitudinal cross-section of an untested couple and the fracture surface of the toughest specimen (see Fig. 5.11). The BSE observation of the longitudinal cross-section shows a unique microstructure, composed of weld pools below the sample surface and a brazing-type structure near the center instead of the usual unwelded central contact area (see Fig. 5.11a). Detailed view highlights the "top" weld pool dendritic microstructure, showing the different grain orientations and the channel used by molten metal to infiltrate the gap at the center of the wires (see Fig. 5.11b). This molten metal acts as a brazing filler materials in between the two dissimilar wires, thus

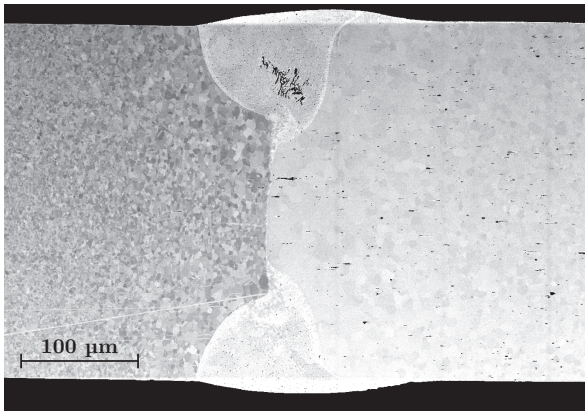

(a) BSE image from a longitudinal cross-section of an untested specimen from sample set A01.

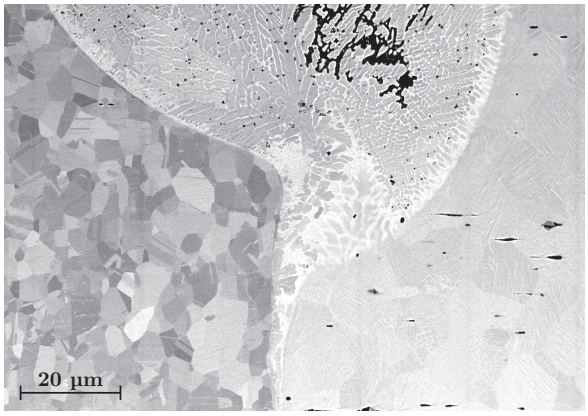

(b) BSE image from the upper weld pool of (a), which shows an internal shrinkage porosity and an unusual brazing microstructure at the bottom.

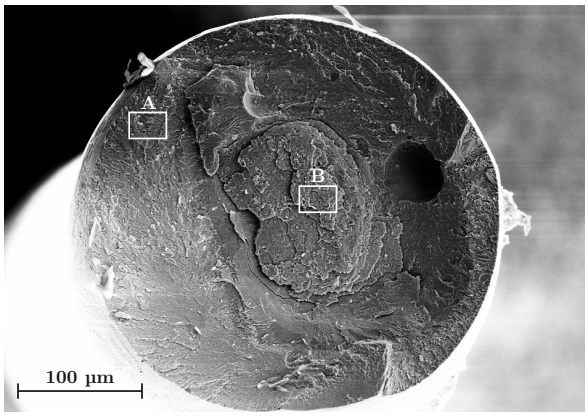

(c) SE image of the fracture surface (NiTi wire side) of the highest UTS sample from set A01.

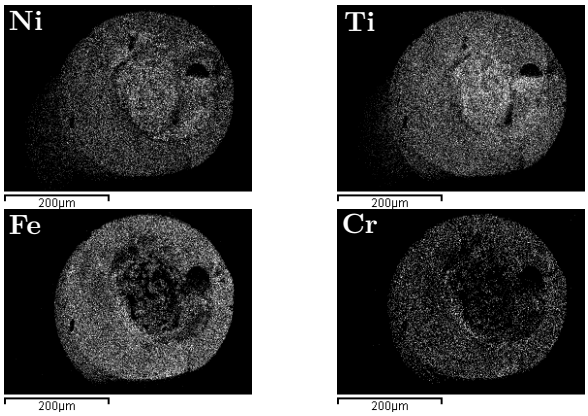

(d) EDX mapping of the four main elements (Ni, Ti, Fe, Cr) from the sample shown in (c).

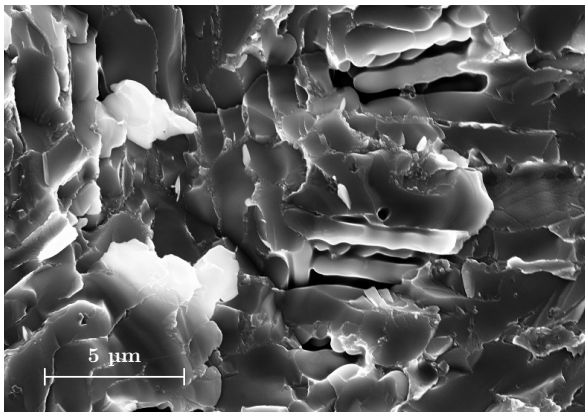

(e) SE image of the brittle fracture area on the perimeter of sample shown in (c) (zone A).

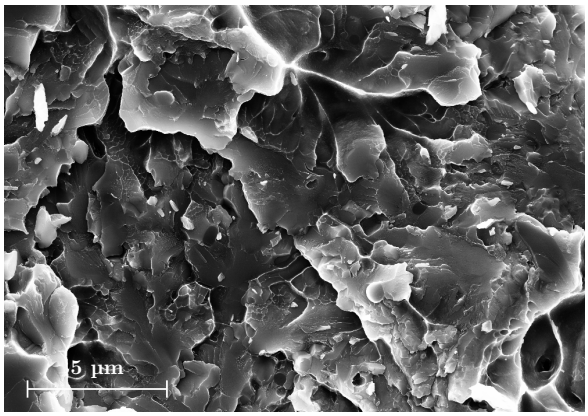

(f) SE image of the ductile fracture area on the center of sample shown in (c) (zone B).

Figure 5.11: Sample set A01 showing partial penetration weld (a) and central contact surfaces are brazed using the molten material from the weld pool area as a filler material. Some porosity are observed in the weld pools (b). The NiTi side fracture surface (c) of the toughest specimen shows inhomogeneous composition of the main elements (d), and a brittle microstructure at the perimeter of the welded surface, labelled A in (c) (e), surrounding a ductile area labelled B in (c) (f).

removing the usual unwanted central void, which would reduce the UTS of the specimen.

The high quality weld fracture surface showed similarities with the best of the pulsed laser specimens, which were later observed during SEM *in situ* tensile experiments (see subsection 6.1.1). Two main areas could be identified on the NiTi wire side fracture surface (see Fig. 5.11c), the perimeter area and the central one. EDX mapping (see Fig. 5.11d) showed a lack of iron and chromium in the center compared to the homogeneous perimeter area. The latter has an overall composition of 50-50 mixing between SS and NiTi, but the center has almost no iron and chromium (the sum is less than 10 at.%). As EDX gives information from the top micrometers below the sample surface, thin films (below 1 µm thickness) are averaged with the substrate laying below. Thus, the signal shown in Fig 5.11d indicates that a very thin layer of the molten weld covers the base NiTi wire standing untouched below the brazing material, as few iron and chromium are detected. The penetration of the latter material in this specimen differs from the pulsed laser case, especially because the weld remains molten during the welding time. The molten filler material wets the base wire surfaces and penetrates by capillarity between them to ensure a transverse joining of the couple.

Shrinkage voids were still found in the weld pools: interdendritic porosity is visible in Fig. 5.11a near the surface. The perimeter area of the weld shows a brittle behaviour, with clear sectioning of the dendrite arms and trunks without plastic deformation, only the interdendritic phase seems to deform before fracture (see Fig. 5.11e). Delamination is also observed in the outer area, leaving deep cracks in the microstructure. Contrariwise, the central zone shows a ductile behaviour with an increasing fraction of microvoids due to plastic deformation before specimen failure (see Fig. 5.11f). Voids forming during solidification in the bulk of the weld are an issue in continuous laser welding and explain the large deviation of the tested specimen UTS within the same sample set.

5.7 Other dissimilar laser welds

This section regroups the last welding considerations made on the NiTi-SS dissimilar system, aiming to define a standard set of pulsed laser parameters to be used later for the correlation between the mechanical properties and microstructures (see chapter 6). Indeed, the pulsed laser DoE shows the best UTS results and especially the lowest standard deviation within the same sample set, which is crucial for the following investigations and for industrial applications. The chosen parameters were those of sample set E11 ($PPP = 100\,\mathrm{W}$, $t_p = 1.6\,\mathrm{ms}$, $Pos = 20\,\mu\mathrm{m}$ on SS wire), so-called "standard" parameters.

The industrial project linked to this work also aimed to achieve sound dissimilar weld between NiTi and platinum-iridium (10 wt.% iridium), later called PtIr. These standard parameters were the starting point to produce NiTi-PtIr dissimilar welds and were refined according to the welded couples surface aspects (see Table 5.4).

Standard parameters led to partial welding of the couples due to the higher reflectivity of PtIr compared to SS (and thus none of the C03 samples could be tested). Thus, the weld energy was increased using longer pulses (C04) and higher power (C05). As the absorption is higher in the liquid phase, the last sample set (C06) was produced with shorter pulses but much higher power, in order to form a liquid film at the surface as fast as possible and so to increase absorption. The overall dispensed energy is lower, but the absorbed one is higher.

Increasing pulse duration leads to a sound weld, showing a structure similar to brazing

	PPP (W)	t_p (ms)	E (mJ)	UTS (MPa)	$StDev$ (MPa)
C03	100	1.6	142	-	-
C04	100	2.0	176	444	34
C05	120	1.8	191	400	85
C06	160	0.5	66	468	73

Table 5.4: Pulsed laser parameters used for NiTi-PtIr dissimilar welding investigations. The laser beam was positioned precisely at the interface of the two wires to reduce the number of variables. Mean UTS and its standard deviation were measured on five samples for each set of parameters.

observed on continuous laser welded specimens at low weld energy (see micrograph of Fig. 5.12a). If the outer part of the joint corresponds to usual observations, the central area of the weld is brazed by the molten NiTi wire, while PtIr remains solid (due to its higher melting point). This made a bond between the wires using diffusion of PtIr wire into the molten NiTi phase, explaining the remaining flat PtIr wire surface in the center. A rounding of the edges of the brazed-type surface at the bottom of the weld pool is visible (see Fig. 5.12a). This was probably caused by Marangoni convection flux, which acts in the same direction than that in NiTi-SS dissimilar welding (see Fig. 5.1). The interface shows dendritic structure growing from the PtIr surface into the NiTi phase, which acts as a strong brazing bond without porosity. These brazing conditions are very interesting as the expected phases remain the same as the initial ones. Besides this aspect, the solidification interval is smaller, reducing the probability of shrinkage porosity formation. Indeed, a smaller solidification interval reduces the likelihood of missing interdendritic liquid feeding as the dendrites are shorter.

The last two sets of parameters show transverse welding in both cases, with the usual welding microstructure. However C05 samples present some trapped defects (intermetallic phases and voids), formed during the extended liquid phase interaction time resulting from the long pulse duration (see Fig. 5.12c). The C06 parameter set leads to a thinner weld than the previous ones and to higher mechanical properties. The microstructure shows traces of convection fluxes through the contrast inside the weld pools (see Fig. 5.12d). One out of the five tested samples of these two last parameter sets had an early failure at low tensile strength, explaining the high standard deviation of their UTS values. This was probably the result of internal defects, such as porosities or a remaining oxide skins trapped in the weld pool. Five samples are not enough to determine whether these defects are a big issue in this weld configuration, and thus, more samples need to be produced under the same conditions.

Two specimens of parameter set C04 and two of C06 sustained the superelastic deformation before rupture, as for the standard NiTi-SS sample set. The maximal UTS was equal to the superelastic strain or even 5% higher. This represents the best UTS that could be expected in NiTi laser dissimilar welding, as superelasticity was found to be the limiting property for coherent deformation of the joined area (see section 6.1.4). Based on these observations, some welded couples were produced between NiTi and SS, using another composition for the nominal NiTi wire to alter the superelastic stress. The only available NiTi wires with the same diameter (300 µm) had a superelastic plateau at slightly lower stress (420 MPa instead of 450 MPa). However, the results (not shown here) definitely confirmed the slight lowering of the maximal UTS of the welded couple to the new superelastic stress. The standard deviations were very broad due to oxide layers

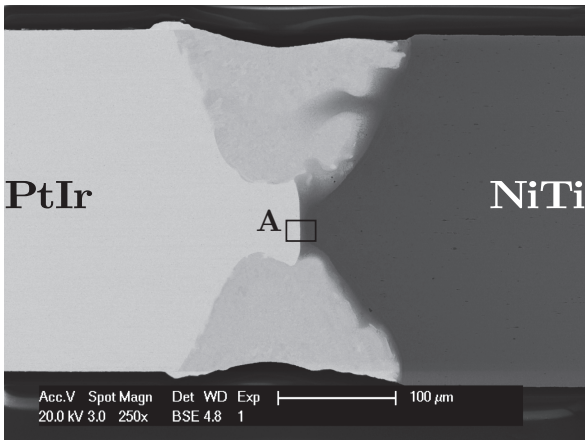

(a) BSE longitudinal view of a specimen using C04 parameter set.

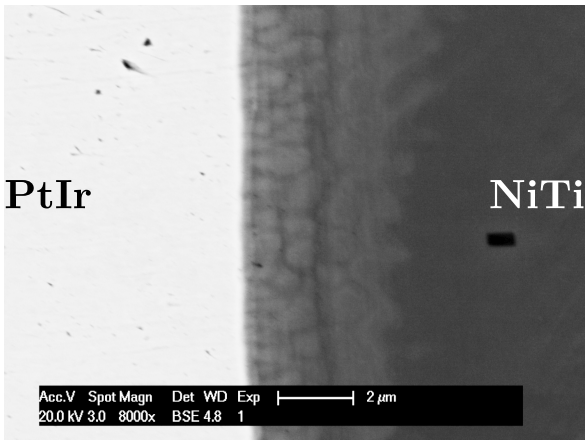

(b) BSE longitudinal view of a specimen using C04 parameter set.

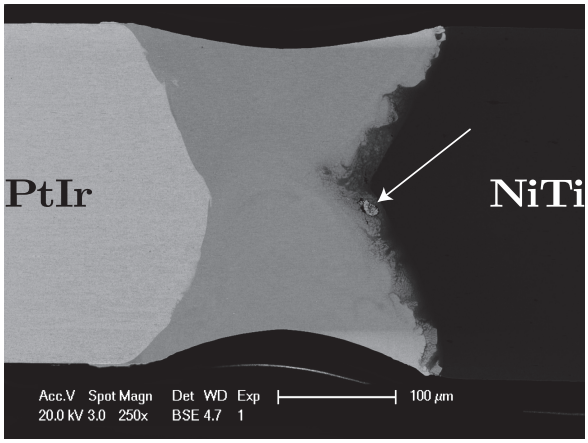

(c) BSE longitudinal view of a specimen using C05 parameter set.

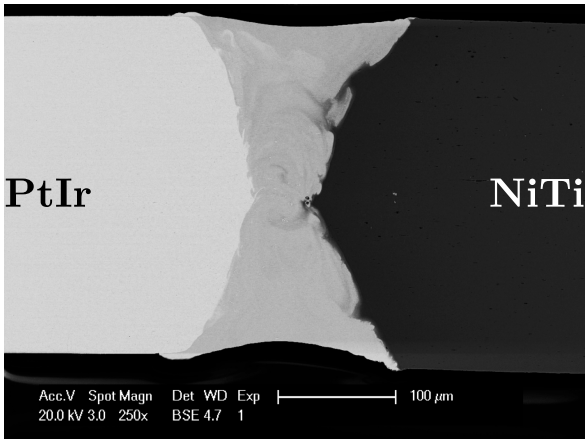

(d) BSE longitudinal view of a specimen using C06 parameter set.

Figure 5.12: BSE images of NiTi-PtIr dissimilar welded couples, PtIr is always on the left.

remaining prior to welding. This oxide folded in the pool and acted as a preferential void nucleation center and crack initiation site.

5.8 Summary

In this chapter, we have shown that sound welds can be produced between NiTi and SS submillimetric wires, but their maximum UTS was found to be limited by the superelastic stress of the NiTi base wires. The best results were achieved using a pulsed laser, because continuous laser welding produced too large welded regions, which usually exhibit shrinkage porosities. These defects reduce the UTS of the welded couple, as they act as preferential crack initiation sites. Several parameters were investigated and only three were identified as main parameters. The positioning of the laser beam with respect to the wires contact interface influences the dilution factor of the weld pool. It was shown that the best results are obtained when the laser is focussed on the SS side (20 µm). The maximum power delivered during the laser pulse, in combination with the pulse duration, defines whether or not the weld is transverse. Indeed, if the energy is not sufficient, an

unwelded contact surface remains in the center of the wires. The laser power needs to be sufficient to reach the keyhole welding mode, in order to lower the required energy to have a transverse weld.

Chapter 6

Mechanical properties and Microstructure

Two main mechanical testing techniques were used during this study: tensile tests to collect information about the average Ultimate Tensile Strength (UTS) of the welded specimens and nanoindentation to gather intrinsic and localized mechanical properties, such as hardness (leading to yield stress) and Young's (elastic) modulus. Tensile testing was done systematically on samples from all laser parameters sets, as it was the primary interest of the industrial partner for medical applications (see chapter 5).

In addition, nanoindentation was performed on carefully selected samples as its preparation was more time consuming and resulting in more information on relative changes in local properties.

The fracture mechanism of the welded couple was further investigated by *in situ* tensile testing conducted on representative samples to validate some of the hypotheses drawn during the first fracture surface analyses. Moreover, automated Digital Image Correlations (DIC) were conducted on the latter *in situ* tensile tests to widen the understanding of their fracture mechanism. Finally, microstructure investigations at micron scale have been realised to correlate laser welding phase formation to fundamental study of the system presented in chapter 4.

6.1 Fracture analysis

After tensile testing of pulsed laser welded wires, several samples, which had crossed the superelastic plateau, were observed. However, most of these welded samples broke at superelastic stress before sustaining superelastic strain. Nevertheless, some of the remaining samples, which deformed above normal elastic strain (meaning they crossed the superelastic plateau, at least partially), were observed in an SEM using SE imaging. The investigations showed that all wires reaching the superelastic stress broke on the same side of the joint, namely the weld-NiTi base wire interface. This first observation was the starting point of *in situ* tensile testing experiments (see section 6.1.1), but also a motivation for further investigations on fracture surfaces.

Imaging of samples corresponding to various parameter sets led to the same observation: The fracture surface could easily be separated in two regions, the outer perimeter and the center of the wire. Indeed, the fracture surfaces showed similar characteristics, a ductile fracture near the center surrounded by a brittle ring on the perimeter. These

observations were done mainly on sound welds, which broke on the weld-NiTi interface, and the two fracture surfaces were investigated (see Fig. 6.1, (a) and (b), both SE images). Incomplete weld through the diameter of the wires led to porosity or defects making the testing neither representative, nor reproducible of the standard behaviour.

The center area of the fracture surface showed typical ductile rupture characteristics with heavily plastically deformed structures. Indeed, on these ductile rupture areas, the remaining grain structure is still visible and shows that it was deformed plastically until the bridges broke during striction, forming the classical microvoids (see Fig. 6.1c). Contrariwise, the outer area showed typical brittle fracture surface characteristics. Indeed, delamination, clear cuts and flat surfaces are generally encountered in brittle rupture (see Fig. 6.1d).

These two main microstructures were further investigated by chemical analysis using EDX measurements. As the surfaces were rough, no quantitative measurements could be conducted by EDX, but no significant iron and chromium element were measured on the ductile fracture surface at the center. On the other side, all base material elements were detected in the brittle outer ring of the surface. These observations led to the conclusion that fracture occurred in the welded area, right at its interface with NiTi wire, and propagated through the remaining of the NiTi base wire in the center. To assess this hypothesis, measurements were made on both fracture surfaces (on the NiTi and SS wires sides) and showed exactly the same results.

Furthermore, several fracture surfaces were reconstructed using the MeX© software to investigate the topology in 3D. SE images were taken with three different tilt angles to allow 3D reconstruction of the surfaces (-7°, 0°, 7°). The resulting reconstruction showed almost flat surfaces with an increasing roughness in the center, resulting from the NiTi base wire plastic deformation before failure. These considerations were based on calculated ratios between true and projected surfaces in both domains, which is in this case the actual surface divided by the wires section. The surrounding brittle domain had a ratio around 1.15 and the ductile center area is always above 1.30. This confirms the appearance of the fracture surface seen on SE images (see Fig. 6.2): The center surface is more deformed and its roughness is higher than the perimeter one, due to the presence of typical deformation microvoids.

These results indicate that the weld has a brittle behaviour and the NiTi base wire is much more ductile as annealing was performed prior to welding to recover the superelastic properties and thus work-hardening is reduced. This leads to a fracture surface with a brittle and undeformed structure on the outer ring and a more plastically deformed surface near the center.

6.1.1 *In situ* testing

In situ tensile testing was made on optimal pulsed laser welded couples, in order to observe the local fracture mechanism due to stress concentration without external defect contribution. To guarantee a good weld quality, a precise set of parameters was chosen, identical to one of the best sets of the second DoE (see Fig. 5.6, #11, Table 5.2). Indeed, this set was identified as the optimal combination of parameters to reach a complete mixing of the base wires and a transverse welding with an overlapping in the center (see Fig. 6.3). These were so-called "standard" conditions ($PPP = 100\,\mathrm{W}$, $t_p = 1.6\,\mathrm{ms}$, $Pos = 20\,\mu\mathrm{m}$ on SS wire).

The first experiments were done without imaging to avoid non-continuous deformation,

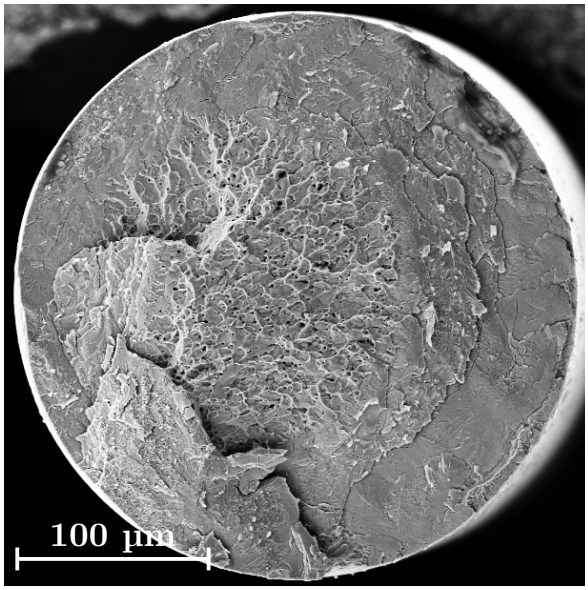

(a) General view of the fracture surface viewed from the SS side.

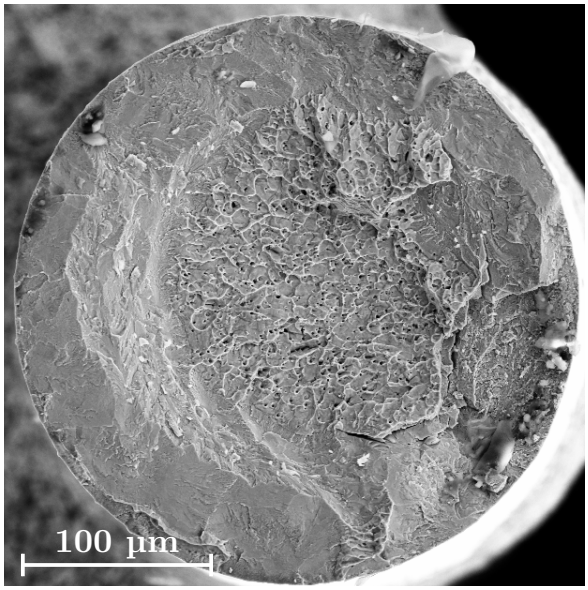

(b) General view of the fracture surface, including the weld, viewed from the NiTi side.

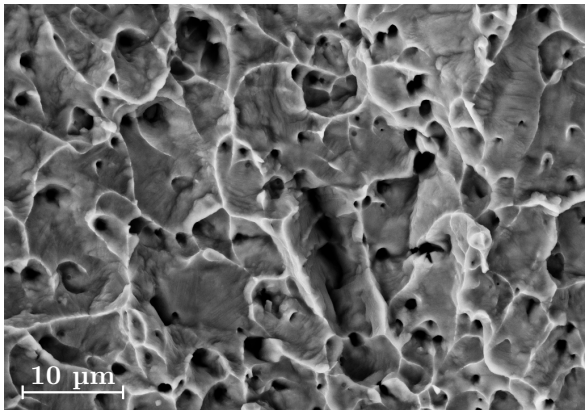

(c) Detailed view of the ductile fracture surface in the center area, viewed from the NiTi side.

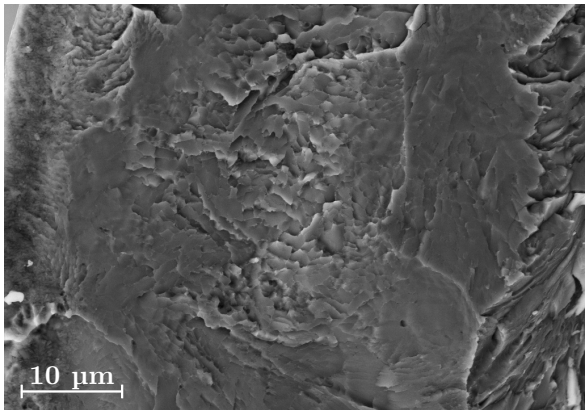

(d) Detailed view of the brittle fracture surface in the outer area, viewed from the NiTi side.

Figure 6.1: SE imaging of fracture surfaces of sound welded NiTi-SS wires, overviews and details of the microstructure in distinct regions.

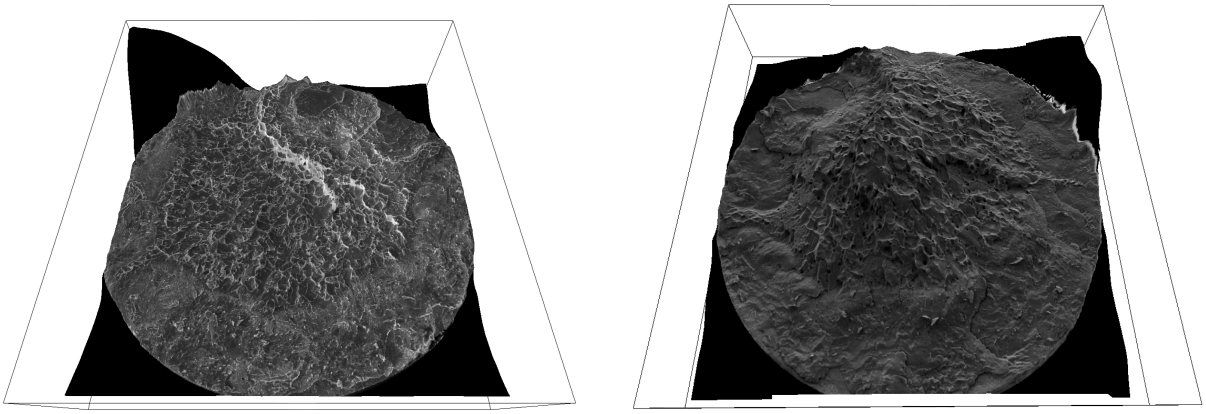

(a) Fracture surface viewed from the NiTi side (300 µm diameter wire).

(b) Fracture surface viewed from the SS side (300 µm diameter wire).

Figure 6.2: 3D reconstruction of both fracture surfaces showed a brittle rupture domain surrounding a ductile structure with characteristic microvoids in the center. The size of the box is 300 µm in the basic direction and around 60 µm in height.

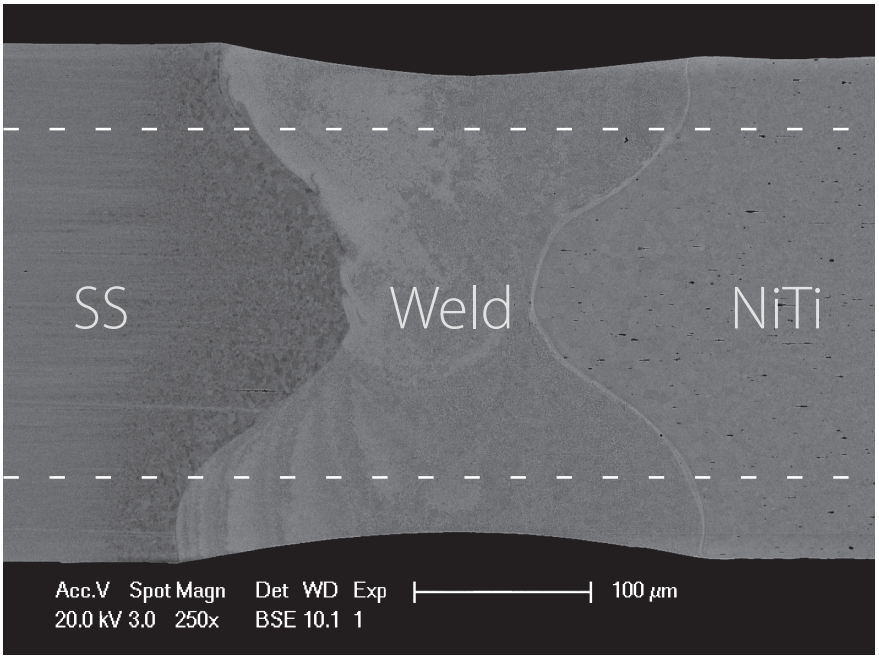

Figure 6.3: Cross-section BSE image of a typical welded couple used in *in situ* tensile testing experiments. The present weld has the original diameter of 300 µm and the dashed lines corresponds to the reduced diameter (200 µm) of the mechanically grounded specimen used for *in situ* tensile experiments. The weld was made using standard conditions ($PPP = 100$ W, $t_p = 1.6$ ms, $Pos = 20$ µm on SS wire).

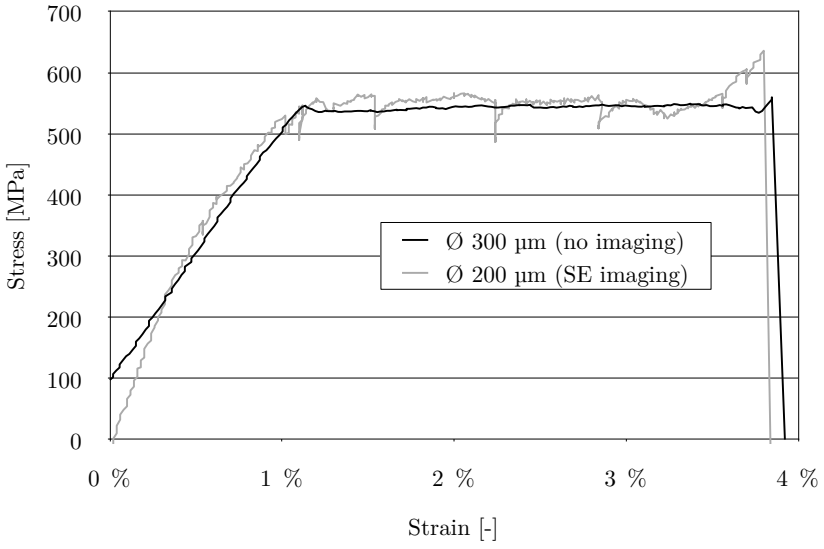

Figure 6.4: Typical tensile curves of *in situ* testing in SEM. Stress and strain are computed from the initial size of the specimen (respectively grip gap and wire diameter), which leads to an average deformation of the wires and may vary as the fraction of each tested materials changes. The black curve corresponds to a test without SE imaging and the grey one with SE images at each kink of the line (partial stress recovery due to compliance). A preloading was applied on the 300 µm specimen to fit to the capstan grips.

as the tensile test had to be stopped during SE signal recording. Fig. 6.4 shows the difference between the tests with and without SE imaging of the weld surface. Kinks in the stress-strain curve results from the tensile device compliance and possible slipping of the capstan grips. The effect of preliminary loading is also visible on the black curve, its elastic part is straighter compared to the other curve, due to a better positioning in the grip. As capstan grips work with a full turn around a pin and then an attachment of the wire with a screw, tension is hard to achieve at the initial position (see section 3.5.2). A preliminary loading to 100 MPa helps the wire to fit to the capstan pins and screws, and explains the beginning offset on the corresponding stress-strain curve.

When imaging the specimen during tensile testing, several steps of deformation and fracture behaviour were observed and analysed. Unusual behaviour was noticed during tensile testing: a crack nucleates when reaching the superelastic stress and then propagates at the end of the plateau (see Fig. 6.5).

Fig. 6.5 also highlights surface defects in different parts of the joined wire couple. For instance, the last spot of the weld is visible on the left side of the surface, the large circle delimits the ultimate weld spot made by the pulsed laser. At the last spot center, a shrinkage defect resulting from the final solidification of the liquid bath is clearly visible (see Fig. 6.5). This could make preferential nucleation site for cracks as the stress intensity factor depends on the notch geometry. Other surface defects are also visible, like ripples on the laser weld spot borders (see Fig. 6.5, bottom right side of the weld surface) due to liquid surface oscillations during solidification [99]. Surface defects are also present on the base wires, such as corrosion pits visible on the NiTi wire (on top) due to oxide

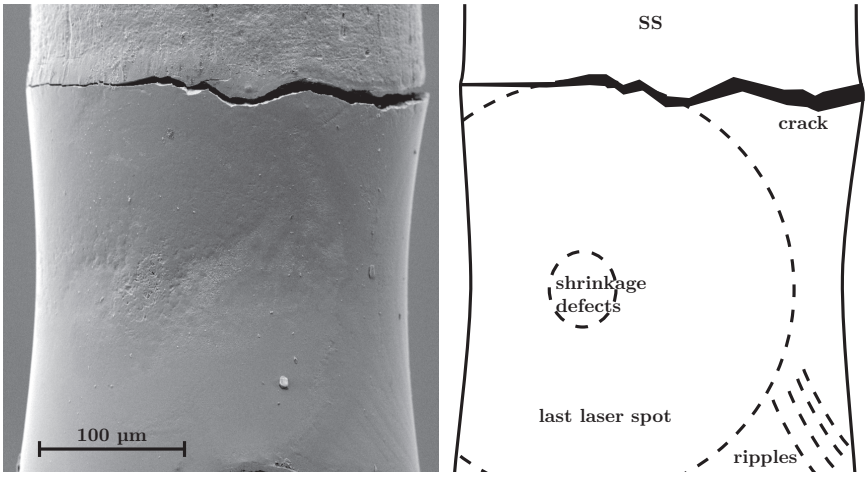

Figure 6.5: *In situ* tensile test experiment made on 300 µm diameter welded wires, showing complete propagation of the crack at the outer perimeter. Stress is still sustained by the remaining NiTi base wire (top wire), located in the center of the sinusoidal shape of the weld.

layer removal etching (wire drawing scratches on the SS base wire could also act as crack nucleation sites).

These considerations required to test a welded specimen without surface defects in order to assess the precise location of rupture independently of these imperfections. A batch of welded couples was machined down to a final diameter of 200 µm using centerless grinding by abrasive wheels (see dashed lines on Fig. 6.3 for the new diameter). This grinding suppressed the thinning of the weld and led to a perfectly straight wire with no visible differences between the two wires and the welded zone. Perpendicular grinding scratches are uniform on both sides of the weld. The EDX analysis was then used for positioning the weld in the tensile test device. Statistical noise is higher on stress measurements performed on these reduced section specimens due to the smaller force applied on the gauge (see Fig. 6.4, grey curve).

During tensile testing, the elastic domain is linear and reversible with an effective Young's modulus $\langle E \rangle$ corresponding to two wires put in series, if one neglects the small welded area itself. If the lengths of NiTi and SS in between the grip are the same, one has indeed $\langle E \rangle^{-1} = 0.5(E_1^{-1} + E_2^{-1})$, where E_1 and E_2 are the Young's modulus of the two base wires. No noticeable damage could be observed until the superelastic plateau was reached (see Fig. 6.6a, and the corresponding position on the stress-strain plot).

Right at the onset of the superelastic plateau (see Fig. 6.6b), a crack initiates at the surface of the specimen, in the transition zone between the NiTi wire and the weld region (see Fig. 6.6b). Then, the crack does not evolve until the end of the plateau and the only visible change is the reduction of the NiTi diameter, since the reversible martensitic transformation occurs at constant volume [14].

Finally, at the end of the superelastic plateau when the stress in the specimen starts increasing again, the crack propagates over the whole perimeter of the specimen along a circle, still in the region of transition between the weld and the NiTi wire (see Fig. 6.6c). This crack opening instantaneously leads to an increased load carried then by the reduced section of the specimen and after a small displacement increment, the central part of the specimen also breaks. The cracked surface corresponding roughly to a cross section of the specimen, the final fracture occurs in the NiTi and a small portion of NiTi remains attached to the weld area (see Fig. 6.3 for the shape of the weld).

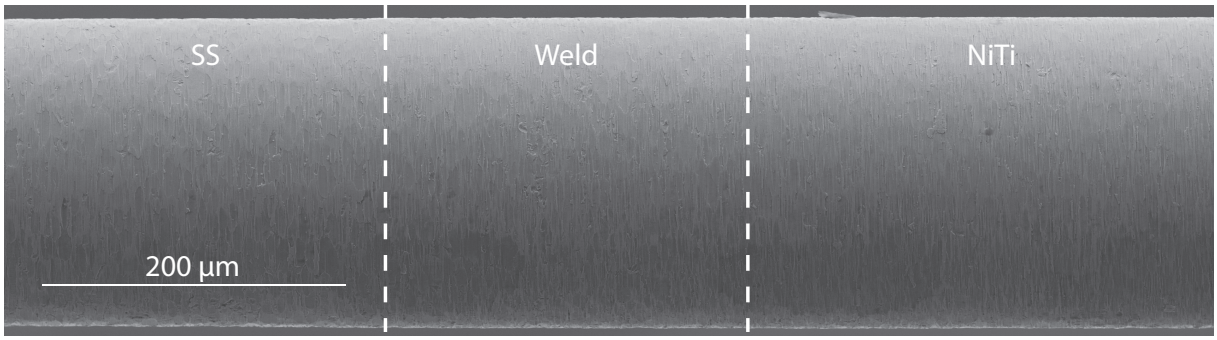

(a) During elastic deformation, no change are visible in the welded area.

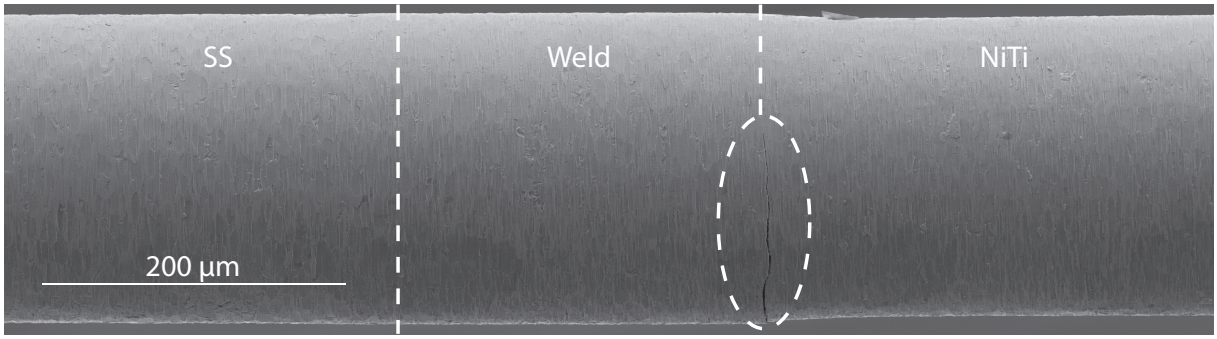

(b) Reaching the superelastic plateau, a crack initiates at the initial kink and does not evolve during the entire superelastic deformation. The dashed ellipse highlights the crack location. The reduced section of the NiTi base wire is also visible as it has crossed the superelastic plateau.

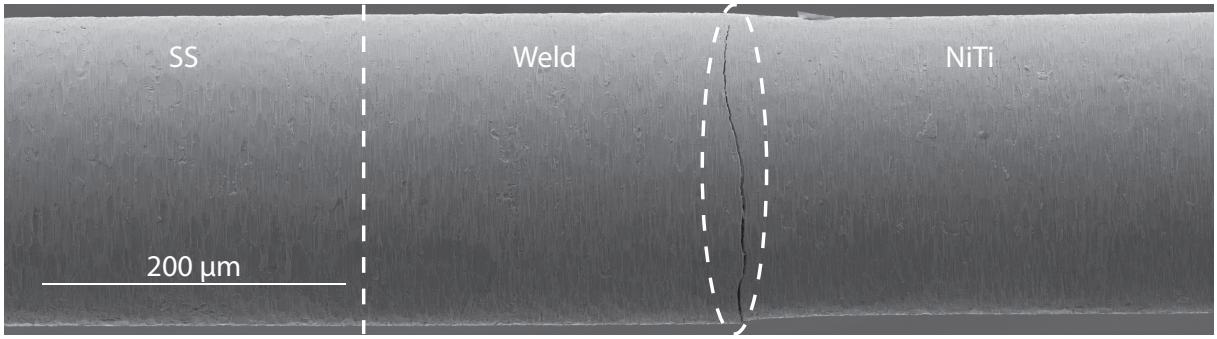

(c) At the end of the plateau, stress increases in the welded couple and the crack propagates over the entire NiTi-weld interface perimeter.

Figure 6.6: SE images of the weld surface during *in situ* tensile testing of the reduced diameter couple. Dashed lines show the limits of the weld region, as determined by EDX qualitative analysis.

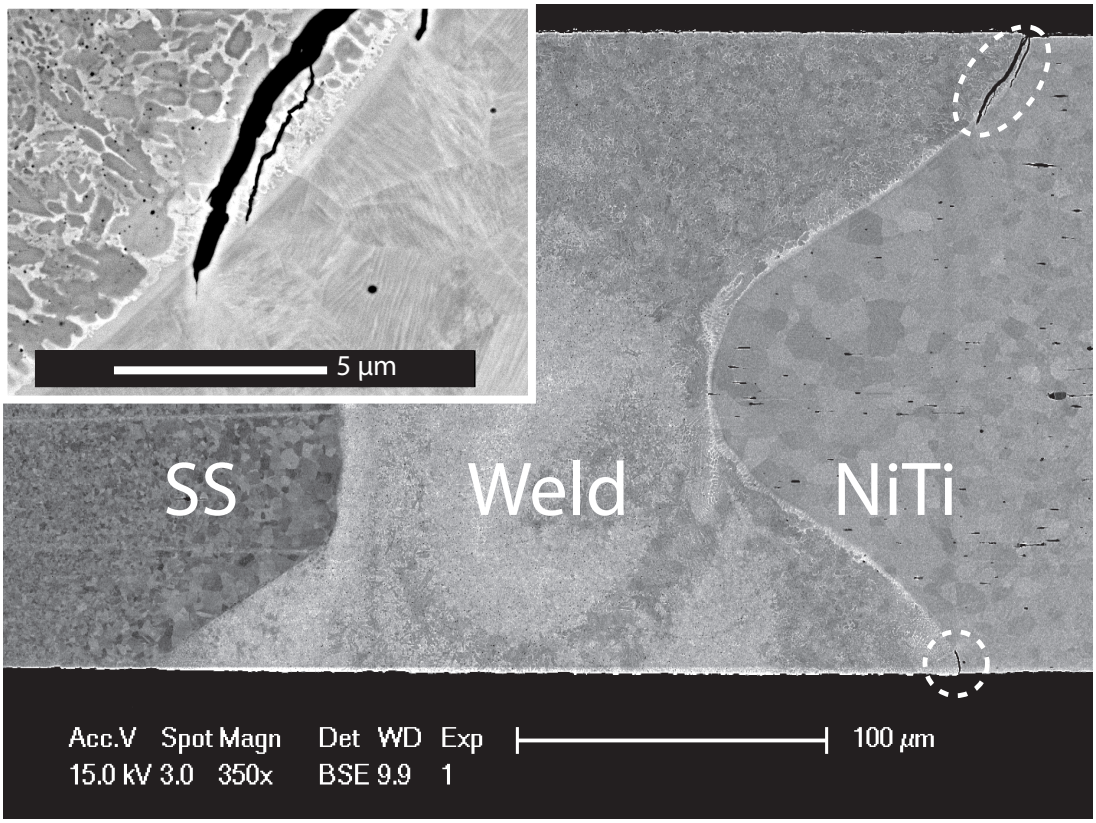

Figure 6.7: SEM BSE image showing a longitudinal cut of a welded NiTi-SS couple deformed up to the end of the superelastic plateau. The two dashed white circles reveal that the crack has propagated over the whole perimeter of the specimen and the enlarged view shows the tip of the upper part of the crack.

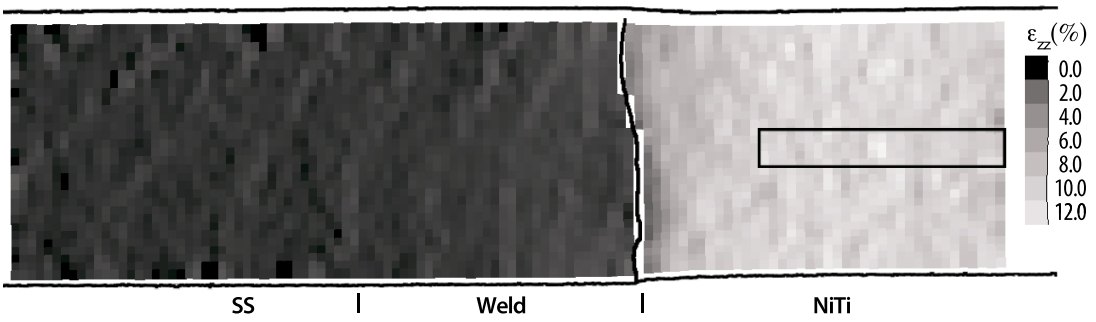

Figure 6.8: Strain field measured by automated image correlation in a longitudinal section of a welded couple during *in situ* tensile testing, between the initial state (unloaded, Fig. 6.4, beginning of tensile curve) and the final state (post-superelastic plateau). The longitudinal component of the strain tensor is shown with various grey level squares, each of them being centred on the deformed position of the initially equally-spaced square grid.

The sample shown in Fig. 6.7 was deformed until the end of the superelastic plateau (end of grey stress-strain curve in Fig. 6.4). After polishing a longitudinal section, the crack that propagated over the entire perimeter of the specimen appears on both external sides of the section (dashed white circles). The crack initiates in the weld, near, but not exactly at, the interface with NiTi and propagates nearly parallel to the weld-NiTi interface until it reaches the NiTi base wire. When reaching the NiTi base material, the latter large elastic deformation reduces the stress intensity factor and the crack is stabilized up to the final increase of stress at the end of the plateau. This could be deduced after imaging details of the crack tip after unloading (see Fig. 6.7, detailed area), where the end of the crack (in the NiTi base wire) is closed but still visible.

6.1.2 Automated digital image correlation

Image correlations were used as a validation (and comparison) of the stress-strain calculations (see section. 6.1.4). Indeed, displacements of surface defects and singularities can be tracked between successive images, and from that components of the strain (and rotation) tensors can be deduced. Please keep in mind that such measurements were made at the surface of the sample (see Fig. 6.6) and of course not on longitudinal sections. Only axial deformation was computed as radial and hoop deformations have large errors due to the recording of surface deformation, possible rotation of the tested wire and aspect ratio of the surface defects used for grid reference. However, theoretically, all deformation components could be computed as the wire is assumed to be cylindrical, but SE images should have a lower pixel size to reach sufficient accuracy for the radial and hoop computations, out of reach in this present tensile configuration.

Figure 6.8 shows the obtained strain field at the end of the tensile test described in Fig. 6.4 (see the corresponding SE image in Fig. 6.6c). The external contour of the welded wires and the final crack are also drawn (black lines) in order to clearly localize the position of the measured strains. The tensile component of the strain tensor, ε_{zz}, is displayed with squares of various grey levels (scale on the left), the center of which being centred on the deformed position of the initially equally-spaced square grid. A bimodal strain repartition is clearly visible: The SS wire and weld region are deformed less than 1% (dark regions), while the NiTi wire experiences a deformation of 9% to 11% (light grey region). This corroborates the computed stress-strain state of section 6.1.4, as the

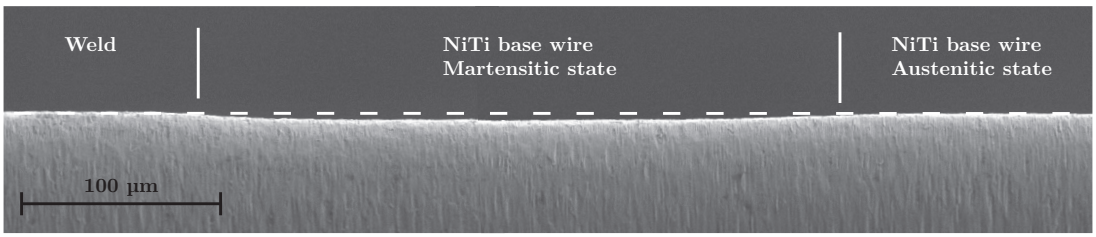

Figure 6.9: Wire surface view during *in situ* tensile testing joined couple (interface between weld and NiTi base wire), right after the onset of the superelastic plateau. The reduction of wire radius is visible on part of the SE image, where the stress induced martensite transformation occurred.

NiTi wire accommodates the deformation by crossing its superelastic plateau. Near the crack, the NiTi surface is relaxed and exhibits a lower axial strain (intermediate grey level region).

In order to better understand the macroscopic superelastic plateau observed in Fig. 6.4, a more detailed analysis of the deformation measured by image correlation was performed between the beginning of the plateau and its end. The NiTi wire deformation component ε_{zz} between these two images was averaged over a sub-domain shown by the rectangle drawn on the right of Fig. 6.8. Surprisingly, while the macroscopic deformation of the whole grip gap increases from 1% (beginning of the plateau) to 3.6% (end of the plateau) (see Fig. 6.4), the average local deformation $\langle\varepsilon_{zz}\rangle$ measured within the rectangle between these two states is only 0.2 %. This shows that the massive transformation already occurred in this region, right after the kink of the plateau, and that the macroscopic superelastic plateau measures the progression of this phase transformation along the whole length of the NiTi wire. The small deformation measured in the rectangle corresponds to the small deformation increase once the whole NiTi wire has transformed into martensite (see Fig. 6.4). Imaging right after the onset of the superelastic plateau, the wire portion transformed to martensite is visible on the micrograph by a radius reduction (see Fig. 6.9). This surface reduction is a consequence of the constant volume transition (Poisson's ratio: $\nu = 0.5$) between austenite and martensite structures.

6.1.3 Indentation testing

To gain a better understanding of the internal stresses developing in the specimen during deformation, mechanical computations were performed with Abaqus© using the inhomogeneous properties measured by nanoindentation (see section 6.1.4). Three domains were considered: the SS region, the NiTi region and the welded zone itself, which was considered to be homogeneous in composition. This last assumption was validated by EDX measurements, which revealed no major composition variations over the welded zone, except for the small white areas at the NiTi-weld interface (see Fig. 6.11).

Assuming axisymmetric properties, the zone outlined by the white rectangle of the longitudinal section shown in Fig. 6.10 was mapped with 5 rows of 16 indentation points. The indentation points were made on a square grid of 25 µm spacing (see Fig. 6.10a). The third position of the bottom row was not indented because of an instrumental problem during the measurement. The local hardness H of the material is not indispensable for the mechanical computations, but it was nevertheless measured and used to deduce the corresponding yield stress (σ_y) according to the approximate relationship:

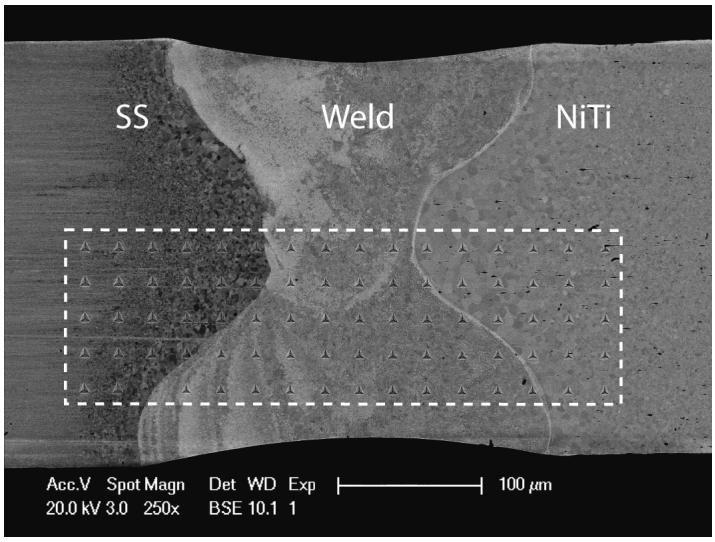

(a) BSE image of a longitudinal section which was indented in the dashed white rectangle with a square grid spacing of 25 µm.

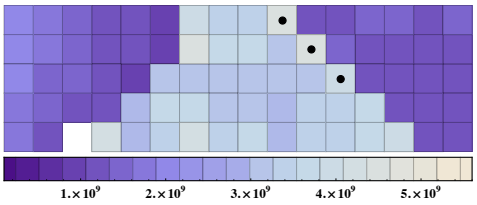

(b) Yield stress plot H (Pa) deduced from the indentation test in the white rectangle shown in (a).

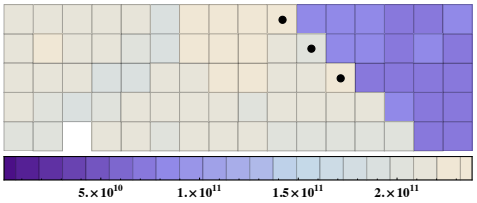

(c) Young's Modulus plot E deduced from the indentation test in the white rectangle shown in (a)

Figure 6.10: Indentation test on a longitudinal section of a NiTi-SS laser weld.

$$\sigma_y \approx \frac{1}{3}H \tag{6.1}$$

	E (GPa)	σ_y (GPa)	N
NiTi	75 ± 4	1.24 ± 0.05	20
Weld	216 ± 6	3.62 ± 0.36	36
SS	208 ± 8	1.38 ± 0.29	23

Table 6.1: Mean Young's modulus (E), yield stress (σ_y) and total number of indentations (N) for the three modelling domains (NiTi, Weld, SS), as obtained from nanoindentation experiments, with their respective standard deviations.

The average Young's modulus E and yield strength σ_y of the three zones, *i.e.*, SS, NiTi and weld region, are summarized in Table 6.1. As can be seen in the maps of Fig. 6.10, the SS base wire shows a slightly reduced hardness (or yield strength) near the weld. This corresponds to the Heat Affected Zone (HAZ), since the high σ_y of the base SS is mainly due to the cold-work during wire drawing. During laser heating, recrystallization occurs and reduces the yield strength. The grain size increase due to heating is clearly visible on the SEM micrograph of Fig. 6.7, especially near the center of the SS wire. The Young's modulus does not show such effect, since it is a more intrinsic property of the material. The hardness of the NiTi wire is not affected in the HAZ, since the wires were annealed after drawing in order to recover their superelastic properties.

Inside the welded area, small variations of the hardness and Young's modulus can be noticed, especially an increase of these properties in the area where the SS content is high (whiter parts of the weld seen in BSE due to higher Cr and Fe compositions). These variations are nevertheless small (± 10%) compared with the large increase between the weld hardness and that of the base wires (see Table 6.1). For these reasons, only the average values listed in Table 6.1 will be used in the mechanical calculations.

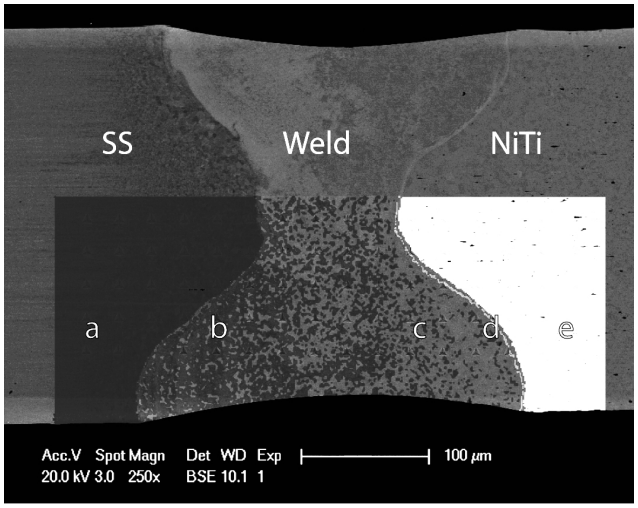

(a) Chemical EDX analysis of a typical weld area superimposed to the SE image. The grey levels indicate the local compositions, the dark region corresponding to that of SS and the white one to NiTi. These regions are also identified with letters (a) to (e) and are reported in the Fe-Ni-Ti Gibbs simplex of Fig. 6.11b.

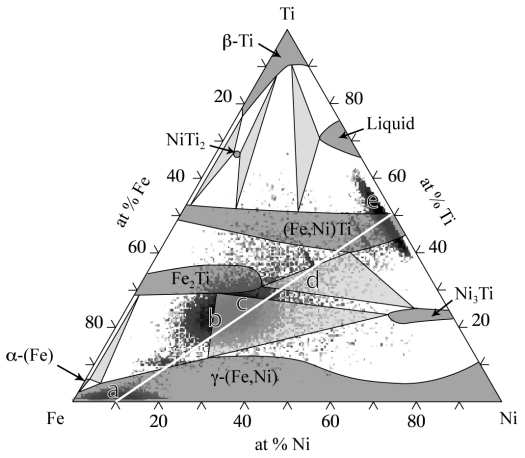

(b) Gibbs simplex of Fe-Ni-Ti similar to Fig. 2.7c with superimposition of the chemical compositions measured by EDX in zones (a) to (e) of the weld area.

Figure 6.11: EDX chemical analysis of the region near a SS-NiTi weld put into relation with the corresponding Fe-Ni-Ti ternary phase diagram.

It is interesting to link these mechanical properties with the local composition measured by EDX (see Fig. 6.11a). Compositions were subdivided into SS- and NiTi-rich areas, the first ones having a higher elastic modulus than the second. At the weld-NiTi interface (right of the figure), a hardness increase can be observed (see the points outlining the 3 light grey squares with $H \geq 12$ GPa). At this interface, a thin white layer is visible at the microscopic scale on Fig. 6.10a, with a phase composition and density giving a brighter contrast than the average NiTi (see Fig. 6.11).

6.1.4 Mechanical Modelling

For the stress-strain calculations performed with Abaqus©, the welded specimen was assumed to be axisymmetric, although the welding process itself is not since it was made by a succession of spot welds with a rotation of the two wires. This is a reasonable assumption since the process is at quasi-steady state (i.e., nearly constant base temperature of the wires) after a few spot welds have been made, and any reheating of a spot weld by the next ones has a minor influence compared to the mixing of the two base materials. Half a longitudinal section was therefore enmeshed over the length of the welded zone (250 µm) and 100 µm on each side of the weld. Three materials (NiTi, Weld, SS) were considered with the properties determined by nanoindentation (see section 6.1.3). NiTi was modelled as an elastic medium up to the superelastic stress (550 MPa), followed by an ideally plastic regime up to 8% strain with a Poisson ratio $\nu = 0.5$ since the austenite-martensite transformation occurs at constant volume [14]. After the superelastic plateau, the strain was modelled by an elastic domain. This elastic-ideally plastic-elastic approximation is only valid upon monotonic loading of the specimen, since during unloading, the superelastic plateau would be omitted in the model. This was chosen because of the restrained possibility of Abaqus© to manage superelasticity. Both the welded zone and

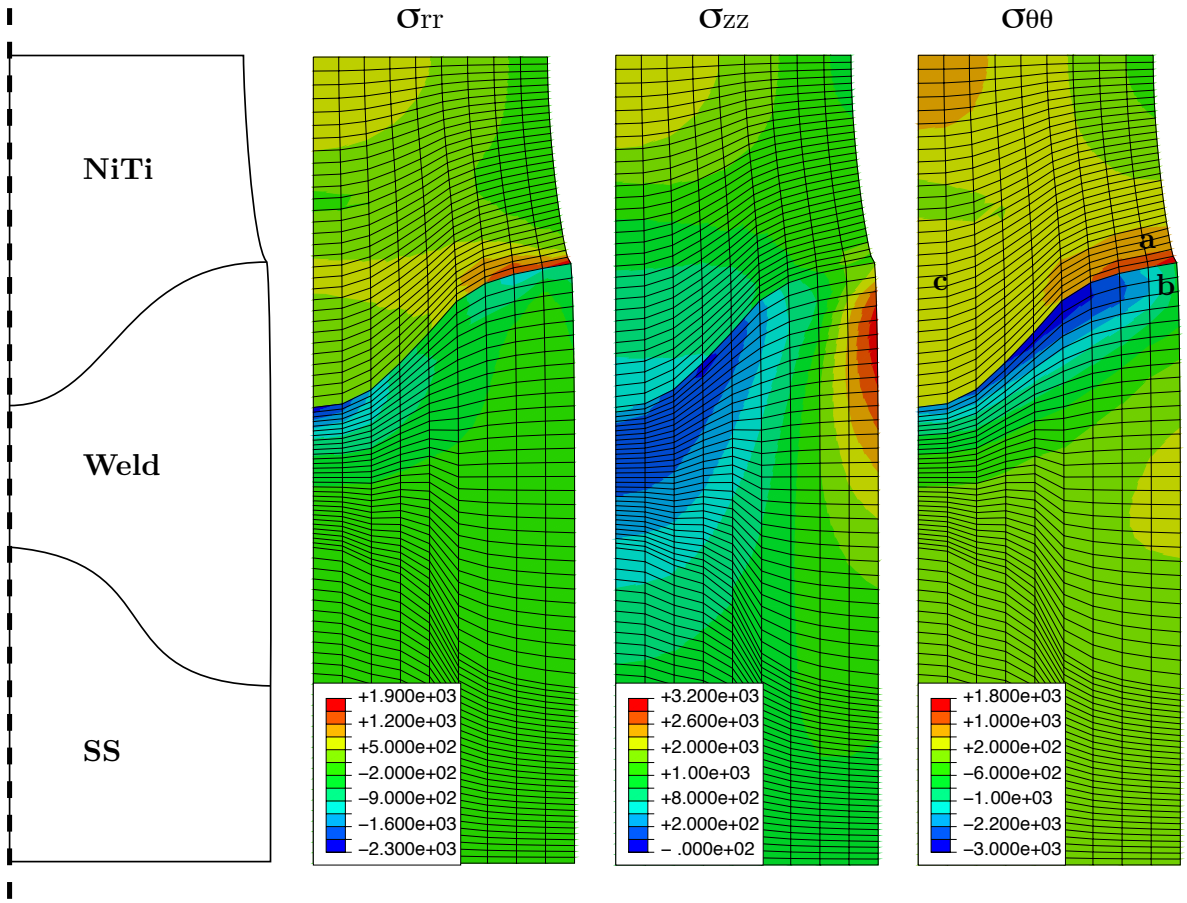

Figure 6.12: Axisymmetric stress calculation of the welded zone, the NiTi wire on top and the SS wire at the bottom, showing the radial (σ_{rr}), axial (σ_{zz}) and hoop ($\sigma_{\Theta\Theta}$) components of the stress tensor. The macroscopic average strain at this point is 5%.

the SS wire were treated as brittle elastic domains. As both domains have higher Young's modulus than NiTi and higher yield stress than the superelastic limit, most of the strain will be localized between the NiTi wire and the welded zone. The interface between the domains was approximated by a sinusoidal boundary fitted to the actual micrographs (see Fig. 6.11a).

Figure 6.12 shows the radial component σ_{rr} and the hoop component $\sigma_{\theta\theta}$ of the stress tensor calculated after 5% total deformation. As can be seen from the highly reduced diameter of the NiTi wire associated with a deformation at constant volume, the superelastic plateau of NiTi has been crossed. Although this deformation stage corresponds to the end of the superelastic plateau of Fig 6.4, the 5% overall deformation of the simulation cannot be directly compared to the 3.5% measured at the end of the experimental tensile curve, since the weld region is much more important in the 450 µm simulation domain than in the 5 cm grip gap of the *in situ* experiment. Moreover, due to the contact with the much harder weld domain, the largest stresses are confined to this region. The large difference in the deformation behaviour of these two neighbouring domains also explains the location of the crack initiation. Indeed, due to its deformation at constant volume once the superelastic plateau has been reached, the NiTi wire is in tension not only along the axial component of the applied load, but also in both the radial and hoop components (region labelled (a) in Fig. 6.12). Please note that the outer ring of the weld region

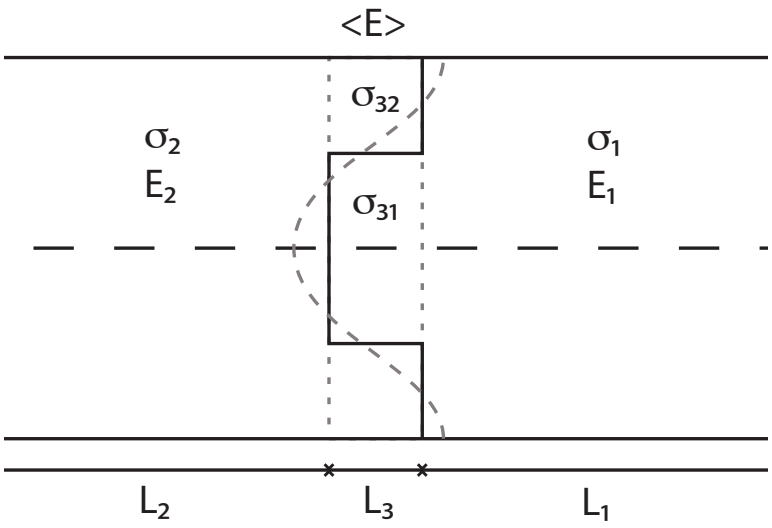

Figure 6.13: Composite model used for a simple stress distribution analysis between NiTi (domain 1) and (SS + weld) (domain 2).

(region labelled (b)) has a compressive radial component. The axial tensile component of the stress tensor in the weld combined with the radial compression component initiates the crack in this zone. The computed axial stress σ_{zz} showed a maxima near this location that explains the preferential initiation site for the start of austenite-martensite phase transformation.

Moreover, the radial component of the stress tensor in the NiTi domain is fairly uniform near the center of the wire, but exhibits a maximum in region labelled (c), which is not closest to the weld. This somehow shields the stress in the tip region of NiTi closest to the weld near the center of the wires and explains why the crack propagates through the NiTi wire near the center of the welded specimen, rather than along the NiTi-weld interface (see Fig. 6.2).

6.1.5 Composite model

In order to better understand the stress localization at the crack initiation point in the welded area, a simple composite model is developed here. For that purpose, only the interface between NiTi and the weld is considered, the later domain having the properties of SS (see Table 6.1), while its sinusoidal shape is approximated by a staircase (see Fig. 6.13). Domain (1) is the NiTi wire, while domain (2) corresponds to the (weld + SS) region. From this simple geometry arrangement, an accommodation domain made of domains (1) and (2) in parallel can be identified (in between the dashed lines): it has a length L_3 corresponding roughly to the extent of the sinusoidal interface shape between NiTi and the weld region. Its average elastic modulus is labelled $\langle E \rangle$. The model considers the uniaxial component of the stress and strain only, and therefore a constant cross-section S of the sample.

The equilibrium of forces along the axial direction imposes that:

$$\sigma_1 = \sigma_2 = \langle \sigma_3 \rangle = \sigma \tag{6.2}$$

The stress $\langle \sigma_3 \rangle$ in domain (3) is an average over the two phases, which can be deduced

from the assumption that both phases in this region have the same strain:

$$\langle \sigma_3 \rangle = (\sigma_{31} \cdot g_1 + \sigma_{32} \cdot g_2) \tag{6.3}$$

where g_1 and g_2 are the corresponding surface fractions of phases (1) and (2) in domain (3), i.e., $g_1 = S_1/S$ and $g_2 = S_2/S$ (see Fig. 6.13).

Using Hooke's law for the parallel configuration of the accommodation zone (3), this can be written also as:

$$\langle E \rangle = E_1 \cdot g_1 + E_2 \cdot (1 - g_1) \tag{6.4}$$

Since $\sigma_{32} = E_2 \cdot \Delta L_3/L_3$, the stress intensity factor in the (SS+weld) region in the accommodation domain (3) is given by:

$$\frac{\sigma_{32}}{\sigma} = \frac{E_2}{g_1 \cdot E_1 + (1 - g_1) \cdot E_2} \tag{6.5}$$

With $E_2 \cong 3E_1$ (see Table 6.1) and $g_1 \cong 2/3$, the stress intensity factor in the (SS+weld) region at the outer surface of the wire is about 9/5, i.e., the stress in the region where the crack appears is nearly twice the applied stress.

6.2 Microstructure analysis

6.2.1 Focussed ion beam

The interface between the NiTi base wire and the weld area is crucial for understanding the fracture mechanism of the NiTi-SS joined wires, as seen in the previous sections. Even if rupture is the result of inhomogeneities of mechanical properties, this interface is the initial crack nucleation site. As classical EDX analysis performed on bulk of the weld cannot resolve the phase distribution in the weld microstructure, 3D-EDX was performed on a smaller zone at the NiTi-weld interface using focussed ion beam (FIB) slicing. The main advantage of the latter technique is the depth information, implying that EDX resolution is improved by information of previous and next slices. Moreover, resolution of the surface is better in these SE images, due to the use of a lower acceleration voltage and imaging filters for the acquired data, as a post-treatment.

A standard sample was used for this FIB 3D reconstruction, as it shows the most representative microstructure. Monte Carlo simulation was performed to determine the interaction volume for SE and EDX signals for the average medium composition of SS and NiTi (the acceleration voltage was set to 10 KeV). The analysed volume was taken in the middle of a cross-section, with the slices parallel to the wires axis and spaced by 12.5 nm, according to the SE resolution. However, EDX mapping was taken only every 8 slices as the characteristic interaction volume at 10 keV is 100 nm in each direction, according to the simulations. Thus the SE resolution is $8^3 = 512$ times higher than the EDX one, and correlation between both information will increase EDX resolution using SE contrast refinement.

Analysing the resulting maps, an intensity contrast is clearly visible on the SE signal recorded on the in-lens detector, corresponding to different phases or areas of similar structure. No precise information can be deduced from SE signal as it is the overall signal of several effects, such as channelling, density, structure and electron configurations. So compiling EDX data with SE images helps to improve the quality of phase determination and the accuracy of their boundaries.

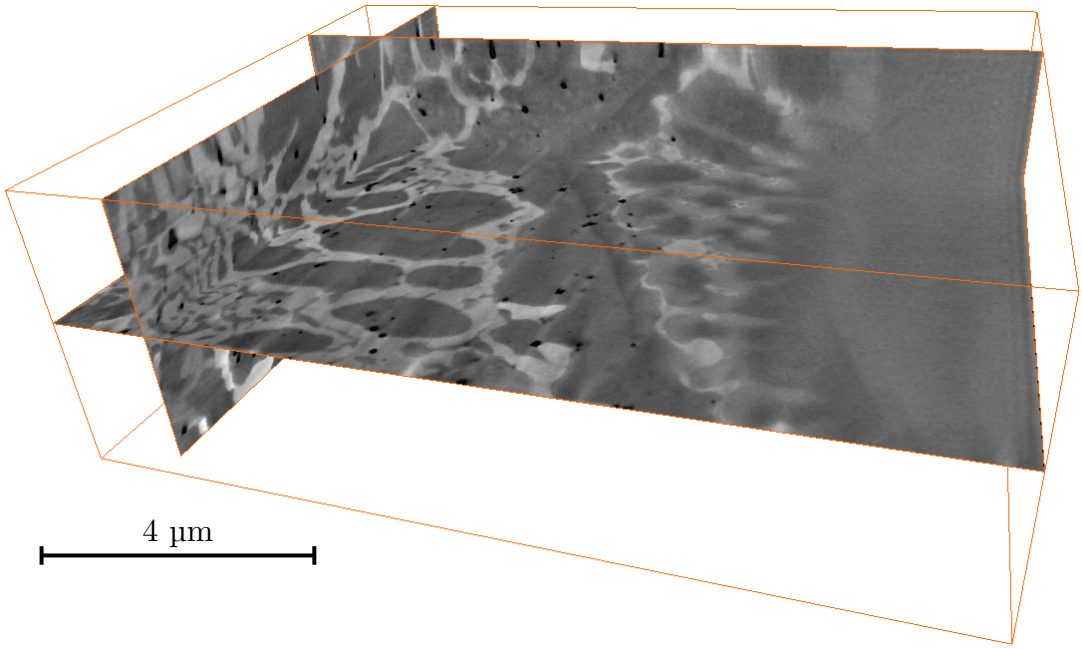

Figure 6.14: Snapshot of a 3D reconstructed volume of a typical NiTi-Weld interface region near the wire center. NiTi is visible on the right (homogeneous grey level) and the weld bulk structure is on the left, showing complex morphologies.

The first treatment applied to the SE images stack (pile-up of successive images) was to ensure a good alignment of the images, by correlation processing. This step was required even if no motion of the stage was done during the whole slicing and imaging of the volume. Following, the stack was resized to the size of the EDX scanned area and some linear defects due to inhomogeneities in the milled surface were removed in the reciprocal space, using Fast Fourier Transformation (FFT), where linear objects are easy to recognize. Fig. 6.14 shows the reconstructed volume (12.8 x 9.8 x 4.4 μm^3) with a SE contrast highlighting different phases.

Due to the long acquisition time required for EDX mapping regarding SE images, and to the EDX resolution, the cubic voxel size is 8 times larger in all directions (100 nm). Dwell time for each EDX map is 5 minutes, leading to a satisfying X-ray count for each characteristic energy used for the main element quantification. Only nickel, titanium, iron, chromium, carbon and oxygen were quantified, after removing background "Bremstrahlung" signal.

A long acquisition was done on the first slice (1 hour dwell time) to accurately resolve the element concentrations in each contrast zone visible on the SE images stack. These compositions measured over the surface are then plotted in the Fe-Ni-Ti Gibbs simplex, superimposed with the theoretical isothermal cut at 1000 °C in Fig. 6.15a. The black line connects the original compositions of the base materials, NiTi and SS, and represents the possible compositions in the microstructure. The measured concentrations of the three elements was plotted in transparency according to their quantification frequency (from blue to red). According to the diffusion theory of Kirkaldy, the experimental diffusion path follows the theoretical rules [33]. For instance, solute balance of the elements is kept, with an experimental diffusion path side to side over the black line, avoiding ternary zones and following tie-lines in the binary domains. The NiTi is clearly present on the experimental phase distribution as part of the analysed volume is made of the NiTi base wire material

(point 1). The second important phase composition frequency is divided into two peaks (the color scale only shows low frequency and values above limit is plotted in red) with separated compositions following tie-lines of binary (Fe,Ni)Ti-Ni_3Ti domain (path 2-3). Similar observation can be made with the iron-rich concentrations, as the frequency of composition avoids the ternary domain and sticks to tie-lines in binary domains (path 3-4). The two remaining highly represented compositions are located at solubility limits in Fe_2Ti and γ-(Fe,Ni) domains (path 4-5).

This classification is used for phase determination while reconstructing the analysed volume with quantified EDX mappings (see Fig. 6.15b). Accurate positioning of the upper and lower concentrations of each element was refined using SE images to fit the observed microstructures, leading to polygonal domains in the ternary phase diagram.

SS-rich compositions are missing in this analysis because the volume is confined to the NiTi-weld interface. However, the mixing can be considered almost homogeneous over the weld as the diffusion path goes up to the SS domain. Additionally, compositions are slightly off the equilibrium concentrations shown (see Fig. 6.15) as the rapid cooling leads to incomplete diffusion in solid phases. Moreover, final solidification happens around the ternary eutectic temperature (1113 °C) and thus differs from the shown isothermal cut and solubility limits change with temperature. The simulated 1300 °C isothermal cut (see Fig. 2.7b) is more representative of the analysed concentration, but is based on experimental data from iron-rich part of the diagram, thus missing composition of interest in this study.

The phase formation sequence reconstructed by FIB slicing and EDX mapping analysis represents the diffusion path followed by the microstructure during solidification (see Fig. 6.16). At the end of the laser pulse, when solidification starts, the weld is completely molten and only the NiTi base wire is solid at the studied interface (see Fig. 6.16a, corresponding to the red domain in Fig. 6.15b). The first phase formed during solidification is NiTi phase with the highest allowed concentration of iron. This phase grows epitaxially to avoid the nucleation energy cost, as the structure is the same as the remaining base wire. Moreover, at the beginning of the laser pulse solidification, the velocity of the isotherm is slow and planar front growth can happen. This planar front quickly destabilizes to a cellular structure and then to dendrites in order to make diffusion in the liquid easier (see Fig. 6.16b, corresponding to the blue domain in Fig. 6.15b). The remaining liquid in between the dendrite arms solidifies with the Ni_3Ti structure (see Fig. 6.16c, corresponding to the yellow domain in Fig. 6.15b), but leads to an excess of iron in the liquid in front of the solidified microstructure. The latter reaches a sufficient iron concentration to form the last phase (Fe_2Ti), delimiting the ternary phase domain (see Fig. 6.16d, and corresponding to the green domain in Fig. 6.15b). Finally, the bulk of the weld solidifies forming an equilibrium between Fe_2Ti and γ-(Fe,Ni) phases showing a pseudo-dendritic network of the first surrounded by the last (see Fig. 6.16e and Fig. 6.16f, respectively corresponding to the brown and black domain in Fig. 6.15b).

This successive phase formation sequence is corroborated by the liquidus projection of the ternary phase diagram (see Fig. 2.7a) in the case of bulk solidification. However, epitaxial growth leads to a preferential development of the NiTi structure at the frontier with the solid base wire, explaining the unexpected contrast observed at this interface during fracture analyses.

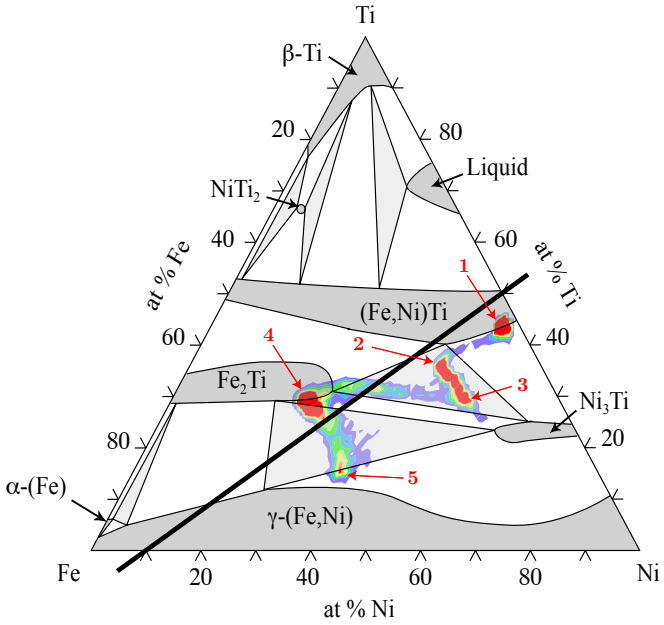

(a) All present phases were found during a one hour EDX acquisition and traces of the diffusion path are visible. The black line connects the two base wire compositions, and is crossed by diffusion path (point 1 to 5).

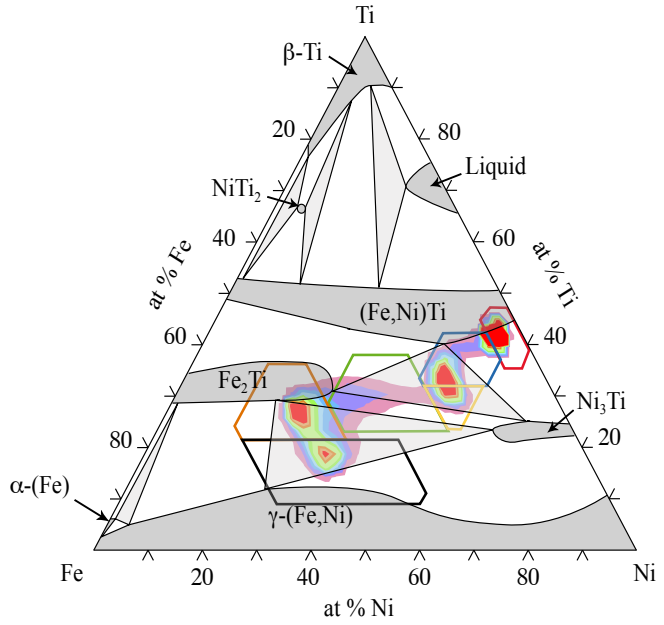

(b) Six compositions (highlighted by polygons) areas were isolated on the basis of frequency distribution during a 5 minute EDX acquisition and used in 3D reconstruction phase selection.

Figure 6.15: 1000°C isothermal cut of Fe-Ni-Ti ternary phase diagram with, superimposed, the quantified EDX mappings done on the first slice, before FIB slicing. The lower map was acquired with the same conditions of the EDX stack maps used in 3D reconstructions (5 minutes). The upper one was analysed over a complete hour to ensure a better phase quantification. Colour scale (from cold to hot colours) is relative to the distribution of compositions over the whole scanned area. Four main zones are visible and one was cut in two parts as the long mapping seems to indicate a separation.

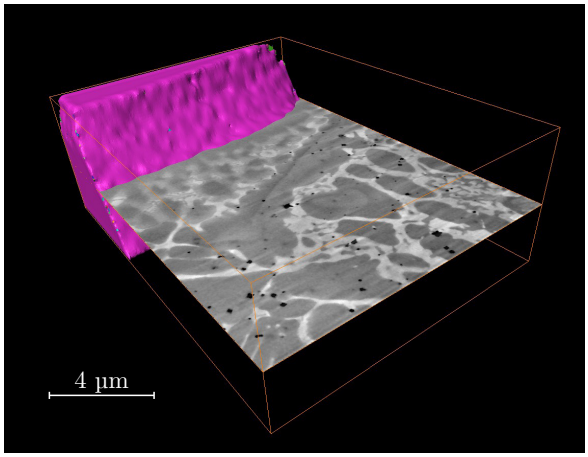

(a) Original NiTi phase (red).

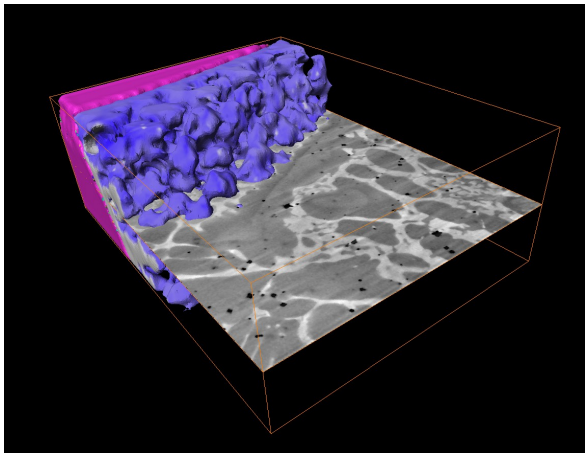

(b) (Fe,Ni)Ti phase (blue).

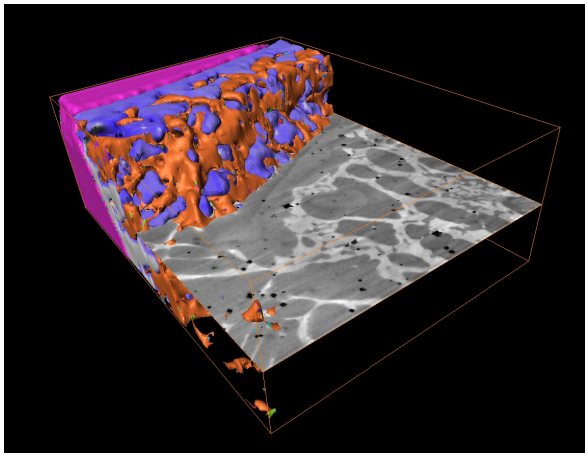

(c) Ni_3Ti phase (yellow).

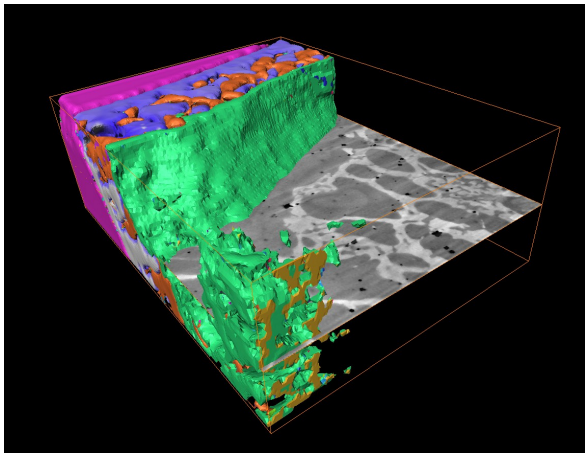

(d) Fe_2Ti and Ni_3Ti phase (green).

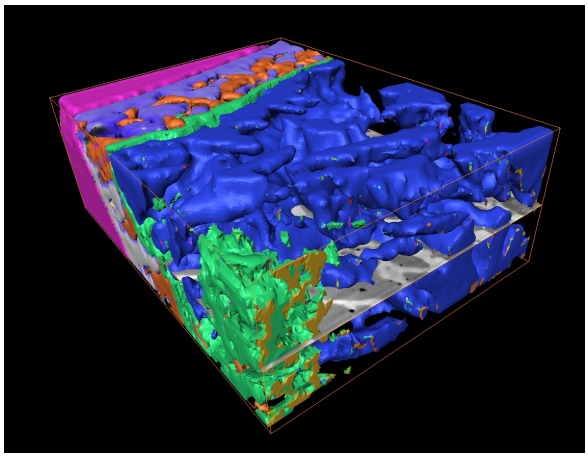

(e) Fe_2Ti phase (brown).

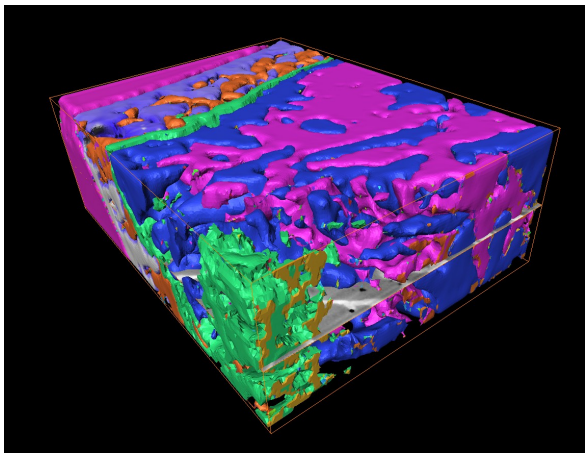

(f) γ-(Fe,Ni) phase (black).

Figure 6.16: Phase sequence shown with successive volume reconstruction superposition from the NiTi base wire side to the weld area. The relative compositions (corresponding domain color is in brackets) are highlighted in Fig. 6.15b by polygones of the same color, following the diffusion path from the NiTi side to the iron-rich corner.

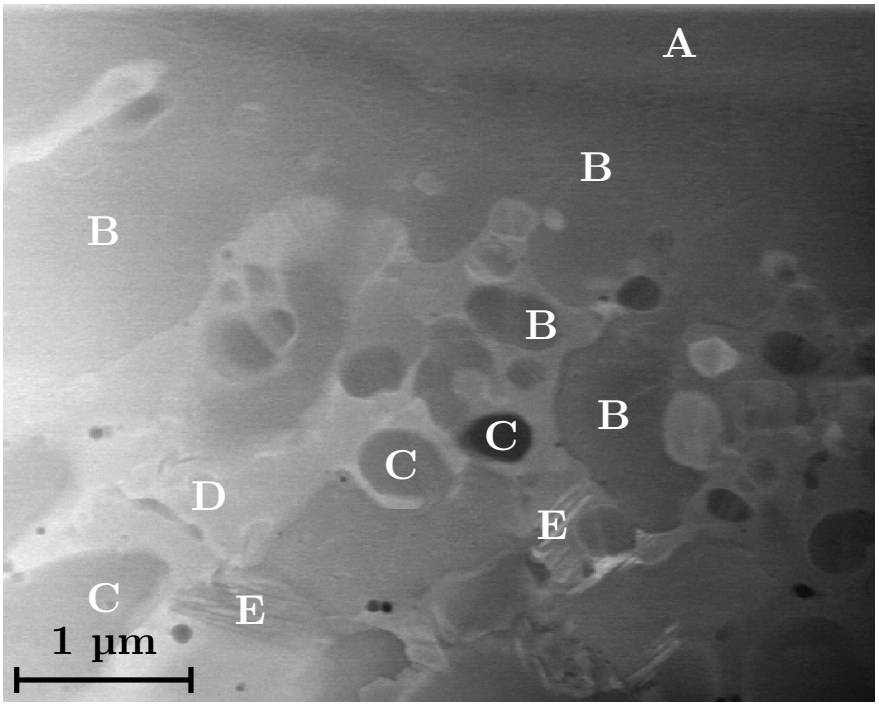

Figure 6.17: TEM observation of a longitudinal cross-section and EDX analyses showed several phases at the NiTi-weld interface region. NiTi unmolten base wire is at the top (A), planar NiTi solidification front grew epitaxially on it (B), primary dendrites of Fe_2Ti (C) are surrounded by Ni_3Ti (D) and (Fe,Ni)-Ti (E) eutectic. This image was taken in DSTEM, where the contrast mainly results in diffraction variations according to the crystal orientations.

6.2.2 Transmission electron microscopy

Transmission Electron Microscopy was performed in DSTEM mode on a sample extracted by FIB from specific zones of the weld microstructure, in order to confirm the observations made in the previous section 6.2.1. Three areas of a standard pulsed laser weld were selected for TEM EDX chemical analyses. First, the NiTi-weld interface visible as a thin light sinusoidal curve on BSE SEM images (see Fig. 6.11a, area d). Second, a BSE dark bulk region containing some iron and nickel, on the NiTi-side of the weld (see Fig. 6.11a, area c). And finally, a BSE light bulk region of the weld containing more iron and nickel (see Fig. 6.11a, area b). The last TEM lamellae was milled out in a continuous laser weld.

The NiTi-weld interface region showed the most interesting results, as it allowed to identify precisely the deduced phases of the FIB 3D-reconstruction sample (see Fig. 6.17). The thickness of the visible transition interface (around 5 µm) corresponds to the analysed size by TEM.

On Fig. 6.17, the end of the unmolten NiTi base wire is visible at the top (labelled A). At the end of the laser pulse, solidification starts on this interface with a low isotherm velocity. The first solidified structure grew epitaxially on the NiTi phase and has the same crystallographic orientation, but an increasing amount of iron. This solid-liquid interface changes from a planar front to a cellular structure, as the solidification speed increases (labelled B). Then, a primary Fe_2Ti phase nucleates in the weld bulk region (labelled C), trapping pockets of liquid in between their arms and trunks. This remaining liquid decomposed into a mixture of Ni_3Ti (labelled D) and (Fe,Ni)-Ti (labelled E) phases. The NiTi-weld interface was visible in BSE SEM as the repartition of Ni_3Ti was regrouped

after the (Fe,Ni)-Ti epitaxial growth along NiTi base wire. Indeed, nickel having a higher density, a brighter BSE signal is obtained from this phase.

The second TEM lamella, in the dark region of the weld (see Fig. 6.11a, area c) showed Fe_2Ti dendrites embedded in a γ-(Fe,Ni) and Ni_3Ti mixing. Contrariwise to the light region (third TEM lamella), which was composed of γ-(Fe,Ni) surrounded by the other phases. The change in SS content produces the BSE SEM contrast. Finally, the continuous specimen showed very coarse Fe_2Ti dendrites surrounded by a Ni_3Ti and (Fe,Ni)-Ti mixture.

All these results corroborated the observations made in the previous section. Indeed, all the phases that were expected from the Fe-Ni-Ti phase diagram, were found in the TEM analyses. This corroborates the idea that the Fe_2Ti phase seems to be unavoidable during NiTi-SS dissimilar welding. Moreover, it forms most of the time as a primary structure making a continuous network inside each grain.

6.3 Summary

In this chapter, we have shown that the NiTi-SS welded couples exhibit fracture surfaces with two distinct areas, a ductile center surrounded by a brittle ring, which explains the results shown in the previous chapter (UTS values in the several DoE). The mechanical integrity of the welded NiTi-SS couple was investigated. The local properties were measured in the weld area using nanoindentation, in order to perform finite elements computations. These computations revealed a strong stress concentration in the outer region of the welded area, especially due to the constant volume of the martensitic transformation, which was stress-induced during tensile testing. This behaviour was assessed during *in situ* tensile testing, performed in an SEM. Moreover, stress-strain state was corroborated by digital image correlation, which emphasized that the martensitic transformation of the NiTi wire started near the NiTi-weld interface, where the stress is the largest. It then propagates along the NiTi wire during the macroscopic isostress plateau until the whole NiTi wire is transformed to martensite at the end of the plateau. Finally, chemical analyses and 3D FIB reconstructions of the interface showed the absence of an intermetallic layer at the interface. Morover, TEM analyses showed the presence of intermetallic phases in the whole welded area. All these observations pointed out that the mechanical properties discontinuity is more dramatic to the welded couple strength than any brittle phase formation.

Chapter 7

Synthesis and conclusions

This chapter summarizes the results from the different experiments and analyses made during this study. The goal, as defined in the introduction chapter, was to produce sound welds between NiTi and SS submillimetric wires using laser welding. As a part of this study, another aim was to realise an analysis of the fracture mechanism and provide an explanation of the systematic failure of the welded couples and of the location of failure.

Literature review indicated that failure of welded couples was determined primarily by the chemical compositions of the weld. Indeed, well known brittle intermetallics are present in the Fe-Ni-Ti system (such as Fe_2Ti and Ni_3Ti). Several studies have shown the possible influence of the solidification paths and kinetics on the presence of these phases in the solidified structures.

Therefore, controlled speed solidification experiments were performed and analysed to get information on the system at different mixing rates. Theses experiments showed the large and unavoidable formation of these brittle phases, with however some changes in their repartition. Indeed, as shown in chapter 4, in SS-rich samples, the brittle phases were in between a continuous dendritic network of steel austenite phase. The latter observations led to the positioning of the laser beam on the SS base wire in order to increase its fraction in the weld pool during the dissimilar laser welding experiments (fewer brittle phases are present).

However, no information was found in the literature about any study of the mechanical strength of welded couples and their intrinsic properties of shape memory alloys. Thus, the study focussed initially on the analysis of these brittle intermetallic phases, such as Fe_2Ti and Ni_3Ti, the fracture mechanism itself and of its dependence on the intrinsic properties of the base wires and on the shape of the weld itself being looked only at the end of the project.

7.1 Laser welding

Based on the literature review and on the controlled speed solidification investigations, laser welding experiments were conducted using statistical models in order to increase the result reproducibility and the welding efficiency (DoE). In addition to the classical pulsed laser welding parameters, such as pulse power, duration and frequency, the dilution factor which influences the welded area composition was also investigated. The dilution factor was investigated by changing the position of the laser beam with respect to the interface between the NiTi and SS wires. However, it could not be investigated over a wide range since a deep penetration depth was needed to reach the wire axis, thus requiring a

transition to keyhole mode. However, this type of weld pools have a highly reduced width at the bottom, thus reducing the variation range acceptable for the beam positioning according to the wires interface.

Moreover, the best welded couples were obtained with the lowest weld energy and interaction time at the liquid state, but the weld still have to be complete over the interface. The latter conclusion shows the difficulty to apply DoE investigation techniques in the case of pulsed laser welding. A trend to minimize the pulse duration and power has been clearly observed in the second DoE, in order to reach high UTS welds. Nevertheless, the DoE models cannot predict the UTS reduction due to partial welding, when the welding energy is insufficient. These models are also limited, since they cannot account for all of the complex phenomena that occur during laser welding. For example, when the laser energy vaporizes the wire matter, no bounding occurs. Thus, the optimal parameters had to be determined manually to reach the lowest possible weld energy, while ensuring a transverse welding of the wire couple section. This issue of modelling is caused by the very strong non-linearity of the relation between power and penetration depth. When the laser welding mode changes from keyhole to conduction, the welded depth is much lower.

In the precise case of dissimilar pulsed laser wire welding, the first DoE analysis showed a maximum for intermediate values. Indeed, only a few samples were welded across their complete contact surface. Using low energy, a remaining unwelded surface reduces the final wire couple UTS. Contrariwise, at high energy, the weld zone is vaporized and no contact occurs.

Afterwards, a restricted number of parameters were investigated over narrower ranges, ensuring a complete welding of the couple section for all the configurations. The model resolution was set to a quadratic dependence and each parameter could take three values (maximum, medium and minimum). Using this model, the maximal UTS were found in lower welding energy couples, for which shrinkage porosities are less present. Thus, the model predicts better results with a lowering of the welding energy, without any consideration of the partial welding. An optimal range is also predicted at high welding energy value, which is an artefact due to the quadratic dependence on the parameters. Indeed, when an extreme of the parameter range gives good results and all the remaining result in lower - but constant - values, a quadratic model predicts high values at the other extreme. In summary, values predicted outside the investigated parameter range must not be taken in account.

To draw a good prediction of the UTS values, a precise forecast of the minimal parameters leading to a complete welding of the section is required. This would allow a cut-off of the quadratic model and the prediction of the best parameters. Nevertheless, a safety margin needs to be used, as little variation in the experiments would lead to a partial welding, and thus a low UTS.

In addition, continuous wave laser experiments were made to assess the influence of cooling rate on the microstructure. In this case, larger grains with intergranular shrinkage porosity were observed, reducing the apparent welded couple tensile strength or, at least, broadening their distribution. Fracture surface observations have illustrated the need to reduce the weld energy in order to avoid the formation of these shrinkage porosities, which lower the maximal tensile properties of the welds. Thus, continuous wave laser welding was not further studied in the experimental design.

Several pulsed laser welding experiments were performed between NiTi and PtIr wires. These investigations were made using the same configuration and similar parameters, in order to have a comparison with the NiTi-SS system.

Both pulsed and continuous laser welding showed the presence of brittle intermetallic phases in the welded areas and a visible interface layer between the NiTi base wire and the welded area. Nevertheless, the best sample UTS never overpassed significantly the superelastic stress of the NiTi wire, even when superelastic strain was observed. Moreover, the observed fracture surfaces showed two clearly distinct zones with opposite fracture behaviour. On these samples, a brittle perimeter area (welded zone) was always surrounding the ductile center (NiTi base wire).

In order to investigate the fracture behaviour of the welded couples, optimal laser weld conditions were defined, in agreement with the previous observations. These parameters were defined as standard conditions to produce sound joined couples between NiTi and SS 300 µm diameter wires. They can be summarized as follows:

- The laser beam has to be positioned 20 µm from the interface, on the SS wire, in order to increase the SS content of the welded area and thus to reduce the presence of the brittle intermetallic phases (Fe_2Ti and Ni_3Ti).

- The pulse duration optimum is 1.6 ms, which is the minimal time of interaction with the liquid phase. Below this value, not enough energy is delivered to the specimen, and on the other hand, the power has to be low enough to avoid vaporizing of the materials.

- The power has to be set to 100 W in order to reach a transverse welding of the wires with the minimal energy. If the power is higher, shrinkage porosities develop in the weld and thus reduce the mechanical strength. Whereas, below this value, the energy is insufficient and an unwelded part remains near the center of the contact interface, which reduces the welded solid section and concentrates the stress in the latter during tensile testing.

However, a few samples in the NiTi-SS system showed very interesting microstructures resulting from a mixed brazing-welding process. At low energy, when only the perimeter is successfully welded, the central part of the contact surface between the wires can be brazed, the molten pool feeding the gap between the wires as a filler material. The latter ensures a complete transverse joint with no porosity remaining in between the wire surfaces. Similar structures were produced in NiTi-PtIr dissimilar wire couples. The center of the contact interface being bonded by diffusion of the PtIr into the NiTi wire, this makes a chemical joining rather than a physical one.

7.2 Fracture behaviour

The previous observations, made on the NiTi-SS and NiTi-PtIr systems, led to the investigation of the mechanical properties and their modelling to understand their fracture mechanism. As none of the UTS from the DoE experiments overpassed significantly the superelastic plateau, *in situ* tensile tests were performed in an SEM. These experiments, conducted on standard NiTi-SS welded couples, revealed the unexpected early crack initiation at the beginning of the superelastic plateau, and its propagation over the whole weld perimeter before failure.

7.2.1 Microstructural effect

In order to develop a realistic mechanical model of the welded couple, the mechanical properties (Young's modulus and yield stress) of the welded area were investigated using nanoindentation. A weakening of the mechanical properties was observed in the SS, near its interface with the welded zone. This results from the recrystallization of the drawn SS wire during laser welding in the Heat Affected Zone (HAZ). However, no mechanical properties variation was observed in the NiTi wire, at the precise location of the usual rupture. In addition, no lowering of the mechanical properties was measured in the welded area, and even an increase of the yield stress was measured.

Chemical analyses performed on the welded area showed a large amount of intermetallic phases (Fe_2Ti and Ni_3Ti) in every region of the weld, even near the NiTi-weld interface. This was predicted by either the constrained (Bridgman), or unconstrained (infrared) growth solidification experiments. Indeed, all the mixing ratios showed the presence of these brittle phases.

A slight BSE contrast was observed between different areas in the weld, especially between the NiTi-rich and the SS-rich sides (see Fig. 6.10a, dark and bright regions in the welded areas). This contrast is explained by a higher content in Fe and Cr in the brighter regions (see subsection 6.1.3). Indeed, chromium seems to concentrate in the SS-rich regions, and to avoid the NiTi-rich areas.

The localization of the chromium element is due to its low solubility in the NiTi-rich phases, such as Ni_3Ti and (Fe,Ni)-Ti, compared to the SS-rich ones, such as (α, γ)-Fe or Fe_2Ti. Indeed, the isothermal cuts of the Cr-Fe-Ti and the Cr-Ni-Ti ternary phase diagrams show a low solubility of chromium in the Fe-Ni-Ti intermetallic phases, except Fe_2Ti (see Fig. 7.1). Thus, a slight BSE contrast is visible between the SS-rich and NiTi-rich sides, due to the remaining composition gradient in the weld.

A careful analysis of the NiTi-weld interface revealed the absence of an intrinsic layer at this location. The observed contrast is due to the succession of different phases, due to the low solidification speed at the NiTi-weld interface. Indeed, the isotherms velocity is almost null when solidification starts at the end of the laser pulse. Thus, a planar front grows epitaxially on the NiTi base wire, before a succession of phases appear in order to reach the weld pool composition. Theses was clearly observed by 3D-EDX reconstruction using FIB slicing, and by TEM-EDX measurements.

7.2.2 Geometrical effect

The tensile tests were modelled using finite element calculations and the mechanical properties determined by nanoindentation. These computations showed that the bowl-shaped interface between the weld and the NiTi base wires induces a stress concentration in the outer ring of the welded area. Indeed, the radial contraction of the NiTi base wire at the superelastic stress implies radial and hoop stress concentrations at the interface. This contraction is due to the variation of the mechanical properties between the NiTi and the welded area. Moreover, the constant volume of the stress-induced martensitic transformation of the NiTi crystalline structure emphasizes this effect. In comparison, the same bowl-shaped interface is present on the SS-side, but no stress concentration occurs as the Young's modulus is similar, and no phase change happens (see Fig. 6.12).

The martensitic transformation is initiated when the superelastic stress is reached at a given location, which occurs precisely at the NiTi-weld interface. A simple elastic com-

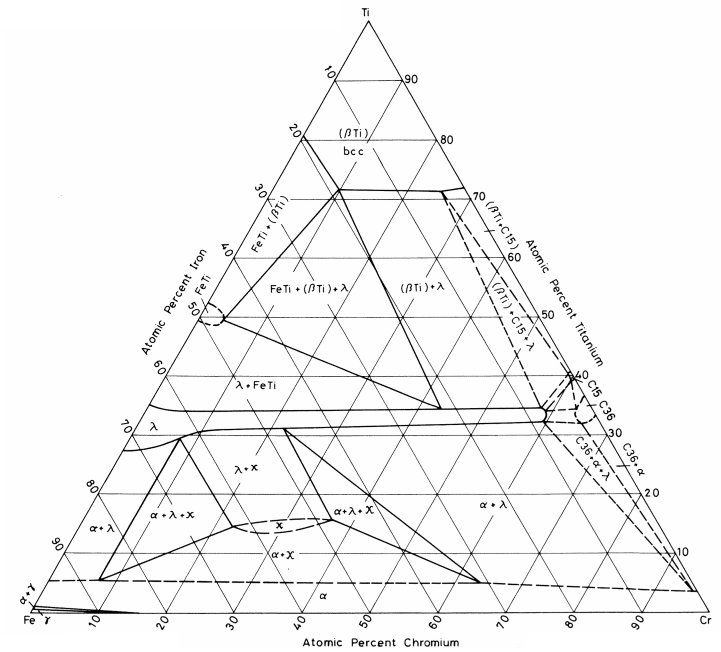

(a) Cr-Fe-Ti isothermal section at 1000 °C in atomic percent, showing the large solubility of chromium in the λ-Fe_2Ti and α-Fe phases. Contrariwise, chromium is much less soluble in the FeTi intermetallic phase.[100]

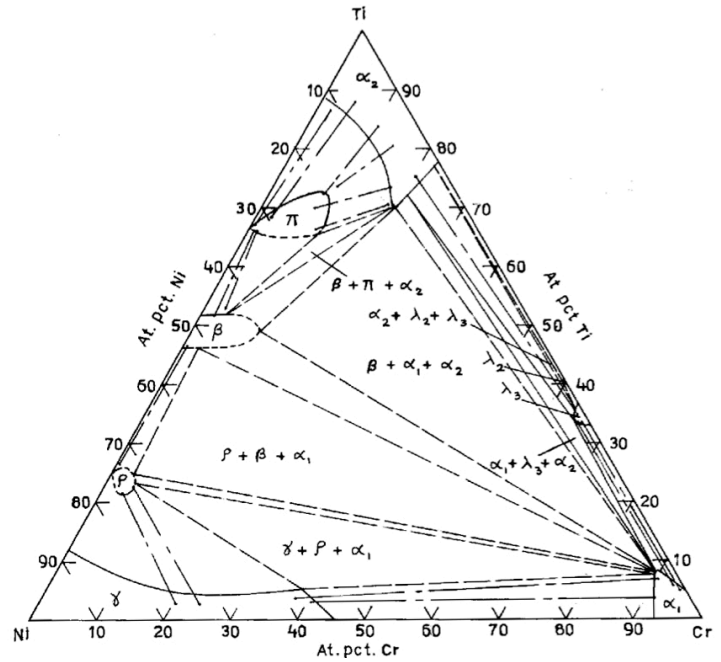

(b) Cr-Ni-Ti probable and schematic isothermal section at 927 °C in atomic percent, showing the low solubility of chromium in the β-NiTi and ρ-Ni_3Ti phases. More chromium is allowed in the γ-Ni phase.[101]

Figure 7.1: Isothermal cuts of the Cr-Fe-Ti and Cr-Ni-Ti ternary phase diagrams, emphasizing the low solubility of chromium in the intermetallic phases, except for the Fe_2Ti, which shows almost a complete solubility. This explains the higher concentration of chromium in the SS-rich regions of the weld.

posite model could explain this highly reproducible location, yet without accounting for the martensitic transformation. Indeed, as the outer ring of the weld area is stronger than the NiTi remaining in the middle, the stress is sustained by the outer region. Thus, the latter reaches the superelastic stress earlier than the remaining of the wire and transforms to martensite. The contraction of the wire increases this effect and the transformed phase fraction evolves when the habit plane progresses. This martensitic transformation initiation at the interface is corroborated by the digital image correlation, which shows a fully deformed structure near the interface at the beginning of the macroscopic superelastic plateau.

As the section of the NiTi wire reduces progressively, the longitudinal stress increases gradually along the whole wire length. When it is fully transformed, which occurs at the end of the macroscopic isostress plateau, the brittle crack then finishes to propagate at the periphery of the weld. At that point, all the load is carried by the center of the welded couple. The crack nearly propagates parallel to the weld-NiTi interface but within the welded area, *i.e.*, perpendicularly to the applied stress. Once it reaches the interface with the NiTi base wire, it continues to propagate perpendicularly to the applied stress, therefore in the NiTi wire. This point is discussed at the end of this subsection since it is strongly related to the shape of the weld.

Complementary computations were then performed in order to assess the importance of the NiTi-weld interface geometry on the stress concentration (see Fig. 7.2). A flat interface would have a lower stress concentration, in each cylindrical components as shown in Fig. 7.2a. Furthermore, when increasing this trend up to an inverse shape interface, *i.e.*, a weld that would be thicker at the center at the wires compared to the periphery, the stress concentration almost disappears (see Fig. 7.2b). However, such a shape is difficult - if not impossible - to produce using the laser welding process.

This stress concentration explains the initiation of the crack at the surface inside the welded area, but not the rupture through the end of the NiTi base wire. Indeed, a small increment of the crack would lead to a similar stress-strain state on a smaller diameter. Thus, the fracture should follow the interface slightly in the welded area up to the complete failure of the joint. However, another effect is involved when the angle between the interface and the pulling direction decreases. The fracture mechanism changes from a pure Mode I crack (opening) to a Mode II crack (in-plane shear). Why the crack chooses to continue in the NiTi wire, perpendicularly to the applied stress, rather than to follow the weld-NiTi interface depends on many parameters: toughnesses of the NiTi base wire and of the weld, as well as the angle between the interface and the direction of the applied stress.

Extrapolating from these observations, a conical interface would be ideal (similar to the inverse bowl shape), if its opening angle maximizes the competition between the two fracture modes. Indeed, the contraction of the NiTi base wire will thus reduce Mode I fracture, and apply a compressive stress on the interface, which will prevent Mode II fracture.

7.3 Conclusions

The resulting failure analysis led to the conclusion that, more than the unavoidable brittle phase formation, the mechanical properties mismatch between the base materials was the reason for the maximal UTS limit of the welded couples. Indeed, when reaching

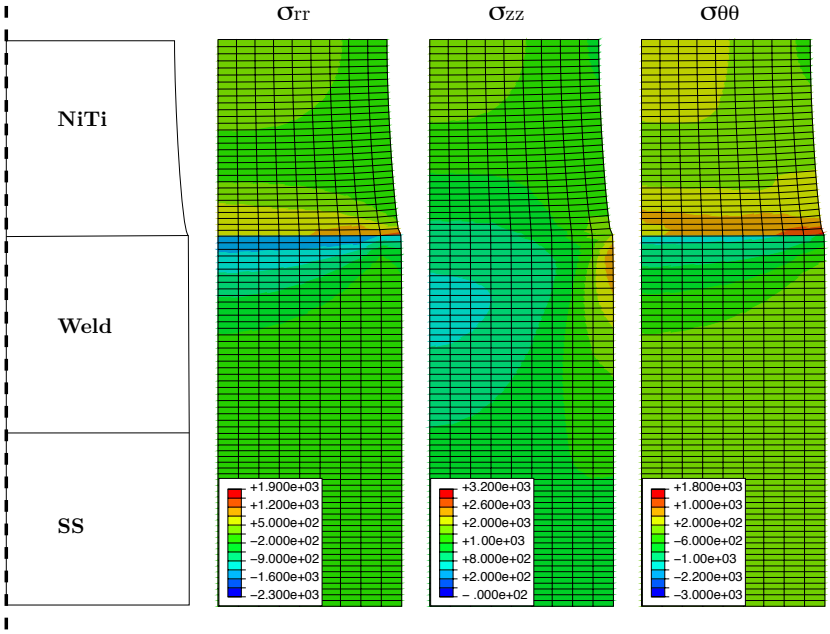

(a) The use of straight interfaces between the welded area and the base wires, predicts a reduction of the stress concentration compared to its typical bowl shape.

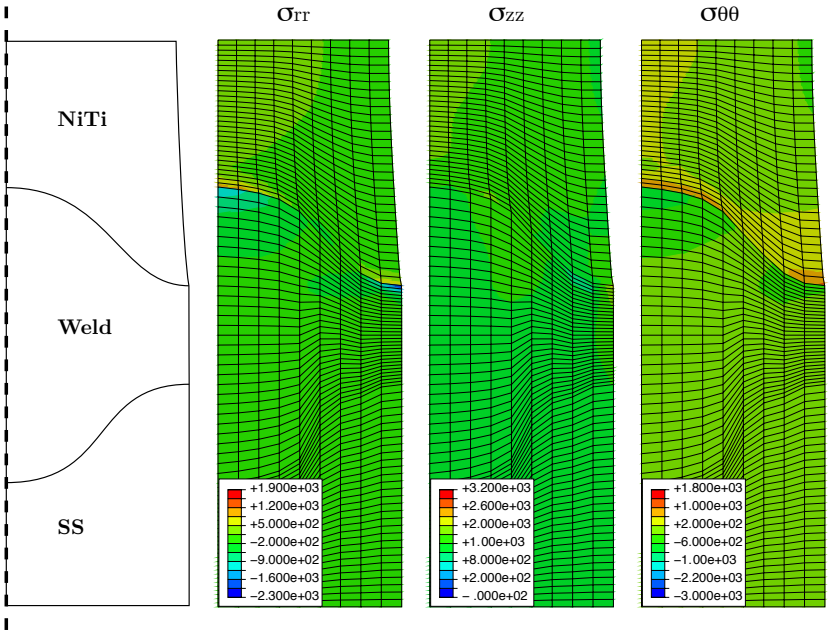

(b) An inverted bowl shape makes the concentration disappear, or at least to be much lower. The ideal shape would be a conical interface with the appropriate angle.

Figure 7.2: Complementary finite element calculations with various interface shapes in order to study its influence on the stress concentration. The stress scaling is identical to that of Fig. 6.12, in order to ease the visualization. The flat interface (top) shows a reduced stress concentration, and the inverse shape is almost ideal.

the superelastic stress, the base NiTi wire starts to plastically deform and the stress is transferred to the welded area, which does not exhibit such superelastic property. This stress concentration occurs in the perimeter of the welded area, especially because the interface between the weld and the NiTi base wire has a bowl-shape. A change of this interface shape to a planar interface (or an inverse bowl shape) will increase the strength of the weld as the stress would be more uniform over the whole section. Indeed, no stress concentration would occur, contrariwise to the perimeter area of the bowl-shape welds, as in the present case explained by the simple mechanical model.

7.4 Perspectives

Finally, to complete this work, additional experiments could be undertaken. As the maximal UTS is fixed by the superelastic limit, an increase of the latter will allow to really determine the welded couple strength. Either a modification of the composition or a change of the testing temperature could provide this superelastic stress modification. As the application field is the biomedical industry, and invasive surgery in particular, the human body temperature may be sufficient to reach satisfactory strength at the temperature of use. In parallel, post welding thermal treatments could be planned to remove the martensitic transformation of the NiTi wire around the welded zone. Indeed, a slight change of the elements concentrations, as in a diffusion couple system, would reduce or even suppress these shape memory properties near the NiTi-weld interface. As the failure is caused by the mismatch between the base materials mechanical properties, and in this particular case the constant volume martensitic transformation occurring during tensile test, removing the SE property of the NiTi base wire close to the weld area would reduce the stress concentration in the weld perimeter area.

Bibliography

[1] T. Duerig, A. Pelton, and D. Stöckel. An overview of nitinol medical applications. *Materials Science and Engineering A*, 273-275: 149–160, **1999**.

[2] J. Ryhanen. Biocompatibility of nitinol. *Minimally Invasive Ther. Allied Technol.*, 9(2): 99–105, **2000**.

[3] A. Bansiddhi, T.D. Sargeant, S.I. Stupp, and D.C. Dunand. Porous NiTi for bone implants: A review. *Acta Biomater.*, 4(4): 773–782, **2008**.

[4] L.S. Castleman, S.M. Motzkin, and F.P. Alicandri. Biocompatibility of nitinol alloy as an implant material. *J. Biomed. Mater. Res.*, 10(5): 695–731, **1976**.

[5] P. Locci, L. Marinucci, C. Lilli, S. Belcastro, N. Staffolani, S. Bellocchio, F. Damiani, and E. Becchetti. Biocompatibility of alloys used in orthodontics evaluated by cell culture tests. *J. Biomed. Mater. Res.*, 51(4): 561–568, **2000**.

[6] J.R. Fisher, G.A. Rosenblum, and B.D. Thomson. Asthma induced by nickel. *J. AM. MED. ASSOC.*, 248(9): 1065–1066, **1982**.

[7] J.K. Bass, H. Fine, and G.J. Cisneros. Nickel hypersensitivity in the orthodontic patient. *Am. J. Orthod. Dentofacial Orthop.*, 103(3): 280–285, **1993**.

[8] K. Otsuka and C.M. Wayman. *Shape Memory Materials:*. Cambridge University Press, **1998**.

[9] W.J. Buehler, J.V. Gilfrich, and R.C. Wiley. Effect of low-temperature phase changes on the mechanical properties of alloys near composition TiNi. *Journal of Applied Physics*, 34(5): 1475–1477, **1963**.

[10] L. Bataillard. *Transformation Martensitique Multiple dans un Alliage à Mémoire de Forme Ni-Ti*. Ph.D. thesis, EPFL nº 1518, **1996**.

[11] David A. Porter and Kenneth E. Easterling. *Phase Transformations in Metals and Alloys*. CRC 2 edition, second edition, **1992**.

[12] K. Bhattacharya, S. Conti, G. Zanzotto, and J. Zimmer. Crystal symmetry and the reversibility of martensitic transformations. *Nature*, 428(6978): 55–59, **2004**.

[13] K. Otsuka and X. Ren. Recent developments in the research of shape memory alloys. *Intermet.*, 7(5): 511–528, **1999**.

[14] K. Otsuka and X. Ren. Physical metallurgy of Ti-Ni-based shape memory alloys. *Progress in Materials Science*, 50(5): 511–678, **2005**.

[15] S. Miyazaki, K. Otsuka, and C. M. Wayman. Shape memory mechanism associated with the martensitic transformation in Ti-Ni alloys. II. variant coalescence and shape recovery. *Acta Metallurgica*, 37(7): 1885–1890, **1989**.

[16] Y. Liu and P. G. McCormick. Factors influencing the development of two-way shape memory in NiTi. *Acta Metallurgica et Materialia*, 38(7): 1321–1326, **1990**.

[17] Tom Duerig, Alan Pelton, and Christine Trepanier. *Nitinol*. to be published, **2011**.

[18] T.B. Massalsky. *Binary Alloys Phase Diagrams*. American Society for Metals, **1986**.

[19] A. Falvo, F. Furgiuele, and C. Maletta. Two-way shape memory effect of a Ti-rich NiTi alloy: Experimental measurements and numerical simulations. *Smart Mater Struct*, 16(3): 771–778, **2007**.

[20] H.F. Lopez, A. Salinas, and H. Calderón. Plastic straining effects on the microstructure of a Ti-rich NiTi shape memory alloy. *Metall Mat Trans A Phys Metall Mat Sci*, 32(13): 717–729, **2001**.

[21] H.F. Lopez. Analysis of solute segregation effects on the peritectic transformation. *Acta Metallurgica Et Materialia*, 39(7): 1543–1548, **1991**.

[22] H.F. Lopez, Rodriguez A. Salinas, and Galicia J.L. Rodriguez. Microstructural aspects of precipitation and martensitic transformation in a Ti-rich Ni-Ti alloy. *Scripta Mater*, 34(4): 659–664, **1996**.

[23] A.S. Paula, K.K. Mahesh, C.M.L. dos Santos, F.M. Braz Fernandes, and C.S. da Costa Viana. Thermomechanical behavior of Ti-rich NiTi shape memory alloys. *Materials Science and Engineering: A*, 481-482: 146–150, **2008**.

[24] M. Nishida, C.M. Wayman, and T. Honma. Precipitation processes in near-equiatomic TiNi shape memory alloys. *Met Trans A*, 17(9): 1505–1515, **1986**.

[25] T. Saburi, S. Nenno, and T. Fukuda. Crystal structure and morphology of the metastable X phase in shape memory Ti-Ni alloys. *Journal of The Less-Common Metals*, 125(C): 157–166, **1986**.

[26] C.Y. Xie, L.C. Zhao, and T.C. Lei. Effect of ti3ni4 precipitates on the phase transitions in an aged ti-51.8at *Scripta Metallurgica et Materiala*, 24(9): 1753–1758, **1990**.

[27] S.K. Wu and H.C. Lin. The effect of precipitation hardening on the m_s temperature in a $Ti_{49.2}Ni_{50.8}$ alloy. *Scripta Metallurgica et Materiala*, 25(7): 1529–1532, **1991**.

[28] Z. Sun and J. C. Ion. Laser welding of dissimilar metal combinations. *Journal of Materials Science*, 30(17): 4205–4214, **1995**.

[29] R. Borrisutthekul, Y. Miyashita, and Y. Mutoh. Dissimilar material laser welding between magnesium alloy AZ31B and aluminum alloy A5052-O. *Science and Technology of Advanced Materials*, 6 (2): 199–204, **2005**.

[30] K. Uenishi, M. Seki, T. Kunimasa, M. Takatsugu, K.F. Kobayashi, T. Ikeda, and A. Tsuboi. YAG laser micro welding of stainless steel and shape memory alloys. In *Proceedings of SPIE - The International Society for Optical Engineering*, volume 4830, pages 57–62. **2002**.

[31] H. Gugel, A. Schuermann, and W. Theisen. Laser welding of NiTi wires. *Materials Science and Engineering A*, 481-482(1-2 C): 668–671, **2008**.

[32] Y.W. Yen, J.W. Su, and D.P. Huang. Phase equilibria of the Fe-Cr-Ni ternary systems and interfacial reactions in Fe-Cr alloys with Ni substrate. *J Alloys Compd*, 457(1-2): 270–278, **2008**.

[33] J. S. Kirkaldy and L. C. Brown. Diffusion behaviour in ternary, multiphase systems. *Canadian Metallurgical Quarterly*, 2(1): 89–117, **1963**.

[34] J.B. Clark. Conventions for plotting the diffusion paths in multiphase ternary diffusion couples on the isothermal section of ternary phase diagram. *Trans Metall Soc AIME*, 227: 1251–1252, **1963**.

[35] F. J. J. Van Loo. Multiphase diffusion in binary and ternary solid-state systems. *Progress in Solid State Chemistry*, 20(1): 47–99, **1990**.

[36] J.A. Dantzig and M. Rappaz. *Solidification*. CRC Press, **2009**.

[37] K.P. Gupta. *Phase Diagrams of Ternary Nickel Alloys, Part 1*. The Indian Institute of Metals, **1990**.

[38] R. Vogel and H.S. Wallbaum. Das System Eisen-Nickel-Nickeltitanid Ni_3Ti-Eisentitanid Fe_2Ti. *Archiv fur das Eisenhuttenwesen*, 12: 299–304, **1938**.

[39] L.P. Dudkina and I.I. Kornilov. Investigation of the equilibrium diagram of the TiNi-TiFe system. *Russian Metallurgy*, 4: 98–101, **1967**.

[40] V.B. Krishnan, R.M. Manjeri, B. Clausen, D.W. Brown, and R. Vaidyanathan. Analysis of neutron diffraction spectra acquired *in situ* during mechanical loading of shape memory NiTiFe at low temperatures. *Materials Science and Engineering: A*, 481-482: 3–10, **2008**.

[41] J. Pfetzing-Micklich, M.F.-X. Wagner, R. Zarnetta, J. Frenzel, G. Eggeler, A.E. Markaki, J. Wheeler, and T.W. Clyne. Nanoindentation of a pseudoelastic NiTiFe shape memory alloy. *Adv. Eng. Mater.*, 12(1-2): 13–19, **2010**.

[42] F..J..J. Van Loo, J.W.G.A. Vrolijk, and G.F. Bastin. Phase relations and diffusion paths in the Ti-Ni-Fe system at 900°C. *Journal of the less-common metals*, 77(1): 121–130, **1981**.

[43] G. Cacciamani, J. De Keyzer, R. Ferro, U.E. Klotz, J. Lacaze, and P. Wollants. Critical evaluation of the Fe-Ni, Fe-Ti and Fe-Ni-Ti alloy systems. *Intermetallics*, 14(10-11): 1312–1325, **2006**.

[44] J. De Keyzer, G. Cacciamani, N. Dupin, and P. Wollants. Thermodynamic modeling and optimization of the Fe-Ni-Ti system. *Calphad*, 33(1): 109–123, **2009**.

[45] N.L. Abramycheva, I.V. V'yimitskii, K.B. Kalmykov, and S.F. Dunaev. I. isothermal cross-section of the phase diagram of the Fe-Ni-Ti system at 1273°K. *Vestnik Moskovskogo Universiteta Seriya 2 Khimiya*, 40(2): 139–143, **1999**.

[46] S.C. Drake. *BSc thesis, p. 34.* Ph.D. thesis, MIT, **1982**.

[47] G. Ghosh. Fe-Ni-Ti (iron-nickel-titanium). In G. Effenberg and S. Ilyenko, editors, *Ternary Alloy Systems - Phase Diagrams, Crystallographic and Thermodynamic Data: Light Metal Systems, Part 4: Selected Systems from Al-Si-Ti to Ni-Si-Ti*, volume IV of *New Series*. Landolt-Börnstein, **2006**.

[48] G Wang. Welding of nitinol to stainless steel. *Proceedings of the Second International Conference on Shape Memory and Superelastic Technologies*, pages 131–136, **1997**.

[49] L.P. Efimenko, L.P. Petrova, and S.I. Sviridov. Interactions in TiFe-Ni system at 1200°C. *Russian Metallurgy (Metally)*, 4: 160–165, **1999**.

[50] P. Riani, G. Cacciamani, Y. Thebaut, and J. Lacaze. Phase equilibria and phase transformations in the Ti-rich corner of the Fe-Ni-Ti systems. *Intermetallics*, 14(10-11): 1226–1230, **2006**.

[51] S. Hinotani. Microstructure and growth of reaction phases in the diffusion bonding of Ti to Fe, Ni and Cu. *Sumitomo Met*, 42(4): 241–246, **1990**.

[52] V. Raghavan. Fe-Ni-Ti (iron-nickel-titanium). *J.Phase Equilib. Diffus.*, 31(2): 186–189, **2010**.

[53] Albert Einstein. Zur quantentheorie der strahlung [on the quantum theory of radiation]. *Physik. Zeitschr*, 18: 121–128, **1917**.

[54] W.M. Steen. *Laser Materials Processing.* Springer-Verlag, **2003**.

[55] X. Liu, D. Du, and G. Mourou. Laser ablation and micromachining with ultrashort laser pulses. *IEEE J. Quantum Electron.*, 33(10): 1706–1716, **1997**.

[56] D. Favez. *Soudage laser or-acier: métallurgie et procédé.* Ph.D. thesis, Ecole Polytechnique Fédérale de Lausanne, **2009**.

[57] Mady Elias and Jacques Lafait. *La couleur – Lumière, Vision et Matériaux.* Belin, Paris, **2006**.

[58] Horst-Gûnter Rubahn. *Laser Applications in Surface Science and Technology.* Chichester etc., **1999**.

[59] M. Von Allmen. Laser drilling velocity in metals. *Journal of Applied Physics*, 47(12): 5460–5463, **1976**.

[60] M. Von Allmen and A. Blatter. *Laser-Beam Interactions with Materials: Physical Principles and Applications.* Springer, **1995**.

[61] P. A. Franken, A. E. Hill, C. W. Peters, and G. Weinreich. Generation of optical harmonics. *Phys. Rev. Lett.*, 7(4): 118–, **1961**.

[62] John F. Ready. *Industrial applications of lasers*. Academic Press, San Diego etc., second edition, **1997**.

[63] Y. Kawahito and T. Okada. Intelligent laser process control in the micro spot welding for copper. *20th Icaleo Congress Proceedings*, 92–93: 1793–1802, **2001**.

[64] T. Stehr, J. Hermsdorf, T. Henning, and R. Kling. Closed loop control for laser micro spot welding using fast pyrometer systems. *Physics Procedia*, 5(Part 2): 465–471, **2010**.

[65] R. Borrisutthekul, T. Yachi, Y. Miyashita, and Y. Mutoh. Suppression of intermetallic reaction layer formation by controlling heat flow in dissimilar joining of steel and aluminum alloy. *Materials Science and Engineering A*, 467 (1-2): 108–113, **2007**.

[66] E. Beyer. *Schweissen mit Laser*. Springer, **1995**.

[67] J.Y. Lee, S.H. Ko, D.F. Farson, and C.D. Yoo. Mechanism of keyhole formation and stability in stationary laser welding. *Journal of Physics D: Applied Physics*, 35(13): 1570–1576, **2002**.

[68] S.W. Pierce, P. Burgardt, and D.L. Olson. Thermocapillary and arc phenomena in stainless steel welding. *Weld J (Miami Fla)*, 78(2): 45S–52S, **1999**.

[69] A. Haboudou, P. Peyre, A. B. Vannes, and G. Peix. Reduction of porosity content generated during Nd:YAG laser welding of A356 and AA5083 aluminium alloys. *Materials Science and Engineering A*, 363(1-2): 40–52, **2003**.

[70] N. Wang, S. Mokadem, M. Rappaz, and W. Kurz. Solidification cracking of superalloy single- and bi-crystals. *Acta Materialia*, 52(11): 3173–3182, **2004**.

[71] P. Schlossmacher, T. Haas, and A. Schüssler. Laser-welding of Ni-Ti shape memory alloys. *Proceedings of the First International Conference on Shape Memory and Superelastic Technologies*, pages 85–90, **1994**.

[72] H. Zimmermann. Fatigue behaviour of a laser welded pseudoelastic NiTi alloy under bending stresses. *Ermüdungsverhalten einer lasergeschweiSSten pseudoelastischen NiTi-legierung unter biegebeanspruchung*, 28(2): 82–87, **1997**.

[73] P. Schlossmacher, T. Haas, and A. Schüssler. Laser-welding of a Ni-rich TiNi shape memory alloy: Mechanical behavior. *Journal De Physique. IV : JP*, 7(5), **1998**.

[74] P. Sevilla, F. Martorell, C. Libenson, J.A. Planell, and F.J. Gil. Laser welding of NiTi orthodontic archwires for selective force application. *Journal of Materials Science: Materials in Medicine*, 19(2): 525–529, **2008**.

[75] Akio Hirose, Masato Uchihara, Takao Araki, Keizoh Honda, and Mitsuaki Kondoh. Laser welding of Ti-Ni type shape memory alloy. *Nippon Kinzoku Gakkai-si*, 54(3): 262–269, **1990**.

[76] Y. T. Hsu, Y. R. Wang, S. K. Wu, and C. Chen. Effect of CO_2 laser welding on the shape-memory and corrosion characteristics of TiNi alloys. *Metallurgical and Materials Transactions A: Physical Metallurgy and Materials Science*, 32(3): 569–576, **2001**.

[77] M. Nishikawa, H. Tanaka, M. Kohda, T. Nagaura, and K. Watanabe. Behaviour of welded part of Ti-Ni shape memory alloy. In *Journal de Physique (Paris),Colloque*, volume 43 of *ICOMAT-82: International Conference on Martensitic Transformations.* Louvain-La-Neuve,Belg, **1982**.

[78] J. Beyer, E.J.M. Hiensch, and P.A. Besselink. *Resistance Welding Of TiNi-Shape Memory Alloys*, chapter The Martensitic Transformation in Science and Technology, pages 199–206. E. Hombogen and N. Jost, **1989**.

[79] A. Ikai, K. Kimura, and H. Tobushi. TIG welding and shape memory effect of TiNi shape memory alloy. *Journal of Intelligent Material Systems and Structures*, 7(6): 646–655, **1996**.

[80] M. Makita, K. Kimura, H. Tobushi, and P.H. Lin. TIG welding of TiNi shape memory alloy. *Nippon Kikai Gakkai Ronbunshu,A Hen/Transactions of the Japan Society of Mechanical Engineers,Part A*, 60(579): 2603–2611, **1994**.

[81] T. Shinoda, T. Tsuchiya, and H. Takahashi. Friction welding of shape memory alloy. *Welding International*, 6(1): 20–25, **1992**.

[82] S. Masunaga. Property of bonded metal,including forming material of nickel-titatium alloy, and the method of manufacturing the same, **1995**.

[83] A. Barcellona, L. Fratini, D. Palmeri, C. Maletta, and M. Brandizzi. Friction stir processing of NiTi shape memory alloy: Microstructural characterization. *Int. J. Mater. Form.*, 3(SUPPL. 1): 1047–1050, **2010**.

[84] Dietmar Mietrach. Method of bonding titanium or titanium alloy to an iron-nickel alloy, **1987**.

[85] Peter C. Hall. Method of welding titanium and titanium based alloys to ferrous metals, **2004**.

[86] D. Favez and M. Rappaz. Micro- and macrosegregation of a peritectic Au-Fe alloy during bridgman solidification. In *12th International Conference on Modeling of Casting, Welding, and Advanced Solidification Processes*, pages 269–278. Vancouver, BC, **2009**.

[87] Francisco Ales. Medical guidewire and welding process, **1996**.

[88] Aiden Flanagan. Process for laser joining dissimilar metals and endoluminal stent with radiopaque marker produced thereby, **2003**.

[89] F. Kohler. *Peritectic solidification of Cu-Sn alloys : microstructure competition at low speed.* Ph.D. thesis, EPFL, **2008**.

[90] Joseph I. Goldstein, Dale E. Newbury, David .C Joy, Charles E. Lyman, Patrick Echlin, Eric Lifshin, Linda Sawyer, and Joseph Michael. *Scanning Electron Microscopy and X-ray Microanalysis.* Kluwer Academic/Plenum Publishers, **2003**.

[91] Valerie Randle. *Microtexture Determination and its Applications.* The Institute of Materials, **1992**.

[92] Adam J. Schwartz, Mukul Kumar, and L. Adams, Brent. *Electron backscatter diffraction in materials science*. Kluwer Academic/Plenum Publishers, **2000**.

[93] Lucille A. Giannuzzi and Fred A. Stevie. *Introduction to Focused Ion Beams: Instrumentation, Theory, Techniques and Practice*. Springer, **2004**.

[94] M. Bornert, F. Valès, H. Gharbi, and D. Nguyen Minh. Multiscale full-field strain measurements for micromechanical investigations of the hydromechanical behaviour of clayey rocks. *Strain*, 46(1): 33–46, **2010**.

[95] L. Allais, M. Bornert, T. Bretheau, and D. Caldemaison. Experimental characterization of the local strain field in a heterogeneous elastoplastic material. *Acta Metallurgica Et Materialia*, 42(11): 3865–3880, **1994**.

[96] W.C. Oliver and G.M. Pharr. Improved technique for determining hardness and elastic modulus using load and displacement sensing indentation experiments. *J Mater Res*, 7(6): 1564–1580, **1992**.

[97] **Calco***soft*©*, user manual, Calcom SA, http://www.calcom.ch, CH-1015 Lausanne, Switzerland.*

[98] W.F. Gale and T.C. Totemeier. *Smithells Metals Reference Book (8th Edition)*. Elsevier, **2004**.

[99] M. Rappaz, D. Corrigan, and L. A. Boatner. Analysis of Ripple Formation in Single Crystal Spot Welds. *Modeling of Casting, Welding and Advanced Solidification Processes*, VIII: 713, **1998**.

[100] V Raghavan. *Phase Diagrams Ternary Iron Alloys*, chapter The Cr-Fe-Ti (Chromium-Iron-Titanium) System, pages 43–54. Indian Inst. Met. 1, **1987**.

[101] K. Gupta. The Cr-Ni-Ti (chromium-nickel-titanium) system-update. *Journal of Phase Equilibria*, 24: 86–89, **2003**.

[102] George E. P. Box, Hunter J. Stuart, and Hunter William G. *Statistics for Experimenters: Design, Innovation, and Discovery , 2nd Edition*. Wiley-Blackwell, **2005**.

Appendix A

Design of Experiment

A.1 Literature bases

A.1.1 Full Factorial Design

A full factorial design is well adapted to get preliminary information on the experiment, before choosing the main factors and the most appropriate model. It consists in determining the interval of every factor and testing minima and maxima of each of them. As only extremes are tested, values of each factor are rewritten as "-1" (minima) and "1" (maxima). Screening the whole space of factors, the experimental matrix is written systematically ($2^{N_{param}}$, where N_{param} is the number of selected parameters), further illustrated by a 2^7 design. In a table where each column corresponds to a given parameter (*e.g.*, see Table 5.1), the first column is filled with an alternation of (-1,+1,-1,+1,-1,+1,-1,+1,...). The second column (second parameter) is completed by couples (-1,-1,+1,+1,-1,-1,+1,+1,...). The third column is completed with quadruplets (-1,-1,-1,-1,+1,+1,+1,+1,...) and so on, in order to explore the $2^{N_{param}}$ combinations. For readability reasons, this first matrix is not displayed here.

The realization of a full factorial design requires a large number of experiments (N_{exp}), as each factor increases the number of experiments by a factor two: $N_{exp} = 2^{N_{param}}$. Thus, in our case, $2^7 = 128$ experiments. Moreover, as only minima and maxima are taking into account, the variation is considered as linear, thus the model in only a first order model. However, a full factorial design gives access to all the information on each parameter effect on the response. Even the interactions between several parameters can be detected in this type of designs. Indeed, the interactions of two parameters will be important if both of them have the same values (maximum or minimum), and low if they have opposite effects. Thus, the interactions between factors will act as a single parameter having a value equal to the product of the two parameter columns. In a full factorial design, each parameter is considered independent and the interactions can be detected.

Finally, several additional experiments are required to determine the reproducibility in time of the model. For this example, three more experiments have been made with medium factor values (nb: 0 with the nomenclature used in the example matrix). One of these experiments was made at the beginning, another right in the middle and the last, at the end of the DoE. The other experiments were performed in a random order to minimize chronological effects.

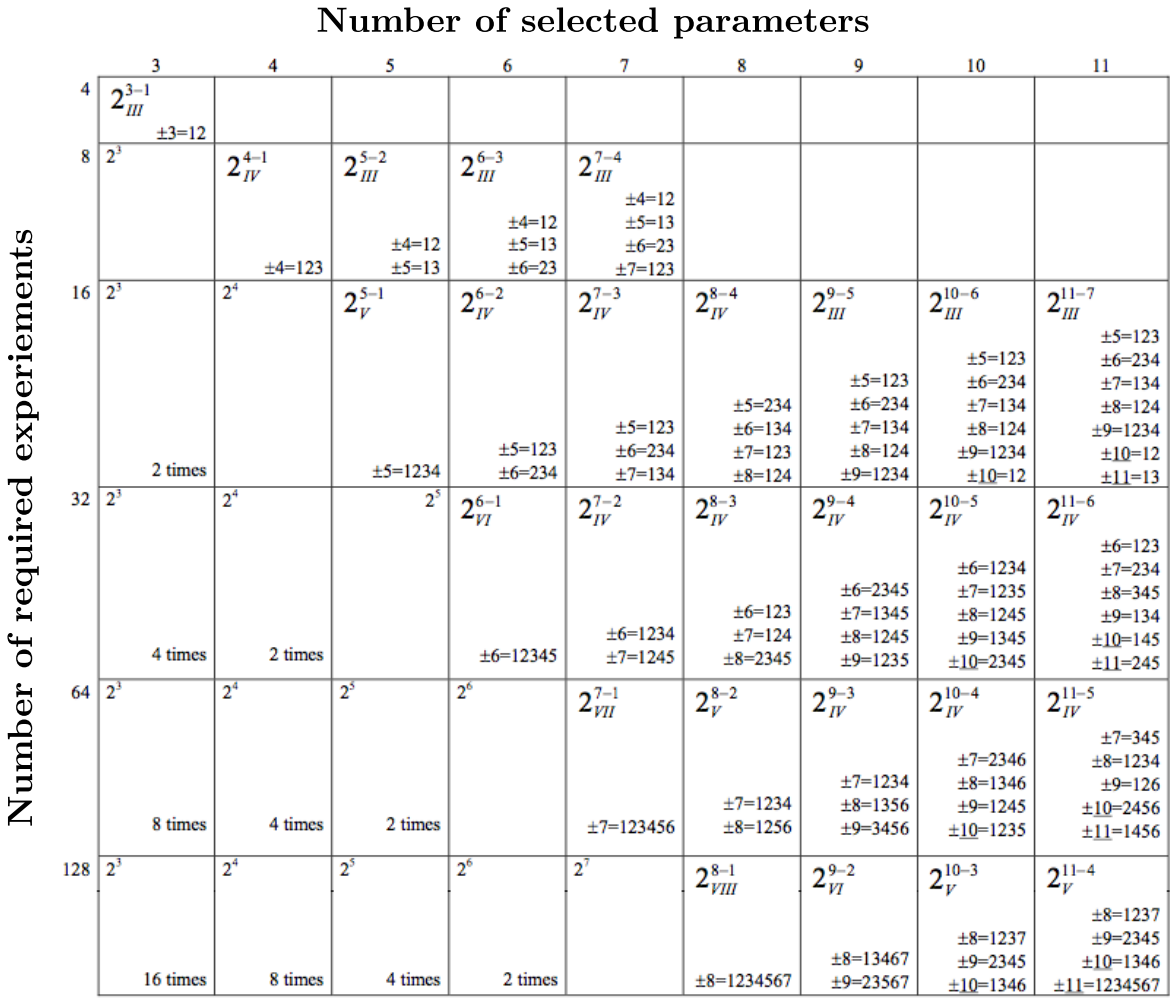

Figure A.1: This table represents the required number of experimental sets regarding the number of parameters involved. The possible *generators* are shown in each corresponding cell. For example, the $2_{\mathrm{IV}}{}^{7-3}$ needs 16 experimental sets for seven parameters, with $\pm 5 = 123$, $\pm 6 = 234$, $\pm 7 = 134$ as generators. This means that the column of parameter 5 is equal to the multiplication of the three first columns ($5 = 1 \times 2 \times 3$).

A.1.2 Fractional Factorial Design definition

A way to bypass the exponential increase of the number of experiments with the number of factors is to consider that some of the high-level interactions can be neglected. Starting from this hypothesis, one can use these interactions to introduce new factors, obtained by aliasing. Coming back to the last example of the full 2^7 design and referring to Fig. A.1, which lists for any type of full factorial design the possible neglected interactions, one can build the new model.

In Fig. A.1, the notation is $2^{N_{para}-N_{alias}}_{Resol}$, where *Resol* is the *Resolution* of the model and N_{alias} is the number of aliased parameter in the model.

This example considers, the fifth column of the table in Fig. A.1, with seven factors. The choice between $2_{\mathrm{VII}}{}^{7-1}$,$2_{\mathrm{IV}}{}^{7-2}$, $2_{\mathrm{IV}}{}^{7-3}$ and $2_{\mathrm{III}}{}^{7-4}$ model is dictated by the *Resolution*. The resolution will be more developed later, but one can already say that the higher the resolution, the better the model. Thus, the $2_{\mathrm{III}}{}^{7-4}$ model is here already eliminated (Resolution III while the two others have a Resolution IV). Moreover, the $2_{\mathrm{VII}}{}^{7-1}$ has a

good resolution, but the required number of experiments is large ($N_{exp} = 64$), thus it is also rejected. The choice between the two last models ($2_{\mathrm{IV}}{}^{7-2}$ and $2_{\mathrm{IV}}{}^{7-3}$) is now made for practical reasons and considering the level of possible neglected interactions. The $2_{\mathrm{IV}}{}^{7-2}$ needs 32 experiments while the $2_{\mathrm{IV}}{}^{7-3}$ needs only 16 experiments to be completed. The *Aliases*, given in the right down corners of the table, show that in the case of $2_{\mathrm{IV}}{}^{7-3}$ model, 3rd order interactions (123, 234 and 134) are considered as insignificant while for the $2_{\mathrm{IV}}{}^{7-2}$ model, 4th order interactions (1234, 1245) are neglected. Considering that 3rd order interactions are insignificant, the choice is then made on the $2_{\mathrm{IV}}{}^{7-3}$ model because with half of experiments comparing to the $2_{\mathrm{IV}}{}^{7-2}$ model, the quality (or *Resolution*) is the same. It is then possible to build the new experimental matrix with three generators: $\pm 5 = 123$, $\pm 6 = 234$ and $\pm 7 = 134$, but first, one has to understand what kind of interactions are taking into account. The *Alias* concept specifies that the first independent factors (corresponding to a full factorial design, in this case, 1, 2, 3, 4) and the *Generators* constitute a commutative group. Several properties are defined by the commutativity, as the presence of an inverse for each element and the presence of an identity (I), which is a column of "1".

Using the concept of aliasing, in this case, the fifth parameter is generated with the interaction between the three first parameters. Thus, its column is the result of the multiplication of the three first ones ($\pm 5 = 1 \times 2 \times 3$ = (-1,+1,-1,+1,...) × (-1,-1,+1,+1,...) × (-1,-1,-1,-1,...) = (-1,+1,+1,-1,...)).

$\pm 5 = 123$, $\pm 6 = 234$, $\pm 7 = 134$ are the generators of our model and $1235 = 2346 = 1347 = I$ is the identity (the multiplication of a column by itself gives a column of "1". Considering the 128 possible interactions of the full factorial design and calculating the aliasing, one can obtain sixteen groups of eight aliased factors. Every line of the table A.1 represents one aliasing group, which effects will be confounded (*e.g.*, $1 \times 2 = 3 \times 5$ =(+1,-1,-1,+1,+1,-1,-1,+1,...)). Indeed, the multiplied columns of each aliases in one line give the same result. This means that no information can distinguish the concerned interactions one from the others.

In this case, first order effects are mixed with third and higher order effects but not between them and second order effects are confounded between them, also with higher order effects (see bold area on table A.1). For instance, the result of the multiplication of columns 1 and 2, gives the same values than the multiplication of columns 3 and 5, or the columns 6 and 7,... It means that it will be possible to isolate every main effect but not the second order interactions. This is the property of the aliasing group of Resolution IV. The resolution can be defined as the ability to separate main effects and low-order interactions from each other. In general, Resolution III, IV and V are used because lower resolution models confound main effects and higher resolutions estimate high-order interactions, which rarely occurs in practice.

The building of the experimental matrix is done by the normal way for the first four columns (factors 1,2,3,4), like for a full factorial 2^4 (1: alternative -1 and 1, 2: alternative -1 -1 and 1 1, etc). The fifth column is obtained by the multiplication of the three firsts rows; $1 \times 2 \times 3$, the sixth by $2 \times 3 \times 4$ and the seventh by $1 \times 3 \times 4$. Table A.2 gives the experimental matrix for a $2_{\mathrm{IV}}{}^{7-3}$ fractional factorial design further used in this project.

A.1.3 Central Composite Design

In order to refine the results, a second design was made, once the first set of experiments has been realized. Based on the first model, we focused on the three main factors and

0	1235	1267	1347	1456	2346	2457	3567
1	235	267	347	456	12346	12457	13567
2	135	167	346	457	12347	12456	23567
3	125	147	246	567	12367	13456	23457
4	137	156	236	257	12345	12467	34567
5	123	146	247	367	12567	13457	23456
6	127	145	234	357	12356	13467	24567
7	126	134	245	356	12357	14567	23467
12	**35**	**67**	1346	1457	2347	2456	123567
13	**25**	**47**	1246	1567	2367	3456	123457
14	**37**	**56**	1236	1257	2345	2467	134567
15	**23**	**46**	1247	1367	2567	3457	123456
16	**27**	**45**	1234	1357	2356	3467	124567
17	**26**	**34**	1245	1356	2357	4567	123467
24	**36**	**57**	1237	1256	1345	1467	234567
124	136	157	237	256	345	467	1234567

Table A.1: Representation of aliases for fractional factorial design $2_{\mathrm{IV}}{}^{7-3}$. The bold numbers area represent the second order aliases that will be indistinguishable from each other. In each line, the interactions between the parameters are equivalent (*e.g.*, $1 \times 2 = 3 \times 5$ =(+1,-1,-1,+1,+1,-1,-1,+1,...)).

	X1	X2	X3	X4	X5=123	X6=234	X7=134
Exp#1	-1	-1	-1	-1	-1	-1	-1
Exp#2	1	-1	-1	-1	1	-1	1
Exp#3	-1	1	-1	-1	1	1	-1
Exp#4	1	1	-1	-1	-1	1	1
Exp#5	-1	-1	1	-1	1	1	1
Exp#6	1	-1	1	-1	-1	1	-1
Exp#7	-1	1	1	-1	-1	-1	1
Exp#8	1	1	1	-1	1	-1	-1
Exp#9	-1	-1	-1	1	-1	1	1
Exp#10	1	-1	-1	1	1	1	-1
Exp#11	-1	1	-1	1	1	-1	1
Exp#12	1	1	-1	1	-1	-1	-1
Exp#13	-1	-1	1	1	1	-1	-1
Exp#14	1	-1	1	1	-1	-1	1
Exp#15	-1	1	1	1	-1	1	-1
Exp#16	1	1	1	1	1	1	1

Table A.2: Resulting values for fractional factorial design $2_{\mathrm{IV}}{}^{7-3}$, labelled with the aliases.

developed a central composite design between a 2^3 full factorial design (8 experiments) and a "star" design (minimum 6 on the faces, plus the center has to be tested many times, 3 times in our case), taking into account second crossed order interactions but also quadratic terms a_{ii}. The easiest way to view the construction of the experiment matrix is to represent it in the three-dimensional space of factors.

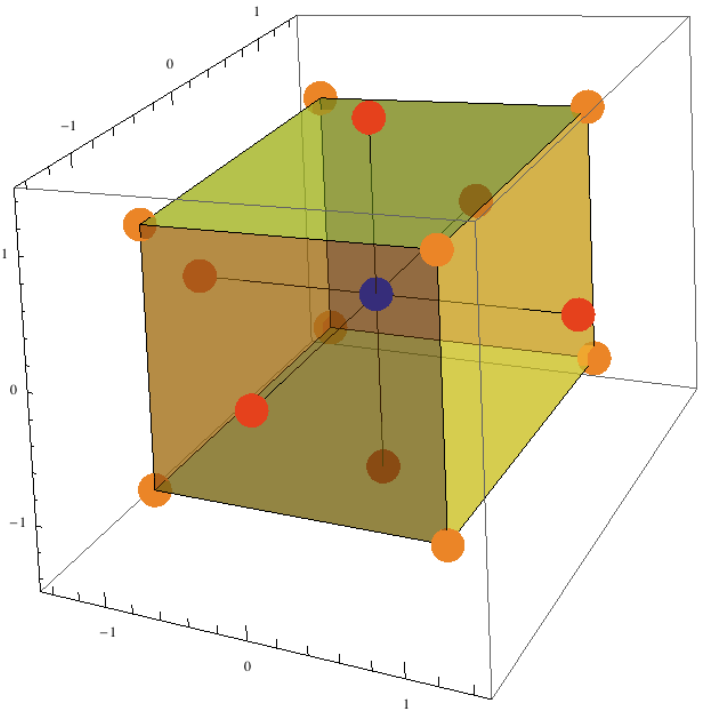

Figure A.2: Central Composite Design

As shown on Fig. A.2, the cube represents the full factorial design. The added points (coming from the star design) are given by an α coefficient depending on the number of factors studied and on the number of central points. Box suggests that for a 3 factors study, any value between 1.5 and 2 is satisfying [102]. He also gives a mathematical way to determine α, respecting the rotability and the orthogonal blocking of the design. However, the chosen value of α in this study is 1.35, in accordance with the central composite design with three central points.

A.1.4 Analysis of results

To analyse the different effects, the usual way is to proceed to an ANOVA (ANalysis Of VAriance). Since fractional factorial design is a first global screening but the only goal is to point out the most important main effects, an ANOVA is not necessary. Therefore, it was decided to proceed by analysis through a relative half-effect plot. However, for the central composite model, a full ANOVA was done. This section gives a short explanation of these two methods of result treatment.

Relative half-effect analysis

First, we consider the matrix A (model matrix), to which one adds a column I (identity) before the first column ($I + A = A_+$, A_+=[8x16]). Then, with the vector of results $\vec{v}$ (16

components), a simple calculation gives directly the effect:

$$\vec{y} = \frac{1}{8} A_+^T \times \vec{v} \tag{A.1}$$

$\vec{y}$ is the half-effect vector (8 components) developed as following:

$$\vec{y} = (y_0, y_1, y_2, y_3, y_4, y_5, y_6, y_7) \tag{A.2}$$

with y_0 the mean value and y_i the mean effect of factor x_i. It is then possible to draw the relative (to the mean value) half-effect plot, giving information about the importance of each factor variation on the global behaviour.

AnOVa

The goal of this calculation is to get the response surface as a function of our three main parameters used in the central composite design. The representation of the response has to be done in a 4 dimensions space (X_1, X_2, X_3, R).

The first step is to obtain the dispersion matrix D from the model matrix A, given in the following chapter, which is defined as:

$$D = (A^T \times A)^{-1} \tag{A.3}$$

One can then determine the Correlation Matrix C:

$$C_{ij} = \frac{D_{ij}}{\sqrt{D_{ij} \times D_{ij}}} \tag{A.4}$$

The diagonal coefficients of the inverse of the correlation matrix are called the Variance Inflation Factors (VIF or v_i with i = 0, 1, 2, 3, 12, 13, 23, 123, 11, 22, 33) and represent the coefficients of the response function. For any coordinate $(X_1, X_2, X_3)_p$, the response R_p is given by:

$$\begin{aligned} R_p = {} & c_0 + c_1 \times X_1 + c_2 \times X_2 + c_3 \times X_3 \\ & + c_{12} \times X_1 \times X_2 + c_{13} \times X_1 \times X_3 + c_{23} \times X_2 \times X_3 \\ & + c_{123} \times X_1 \times X_2 \times X_3 \\ & + c_{11} \times X_1^2 + c_{22} \times X_2^2 + c_{33} \times X_3^2 \end{aligned} \tag{A.5}$$

where, the c_i coefficients are obtained through the following equation:

$$\vec{c} = D \times [A^T \times \vec{y}] \tag{A.6}$$

It is then possible to build a surface response as a function of the three factors.

A.2 Quadratic DoE calculations

The experience matrix for the central composite design was established following a Box-Benkhen scheme and is given in Table A.3.

Then, the model matrix (Table A.4) is only the first part of the experiment matrix, as it was designed to have the specific and normalized values. The model matrix is also

	X_1	X_2	X_3	PPP	t_p	pos	f	RPM	E_{pulse}	UTS
E01	0	0	0	0.12	1.8	0	13.9	22.1	193	393.2
E02	0	0	0	0.12	1.8	0	13.9	22.1	193	375.5
E03	0	0	0	0.12	1.8	0	13.9	22.1	193	351.5
E04	1	1	1	0.14	2	20	12.5	19.9	264	374.1
E05	1	1	-1	0.14	2	-20	12.5	19.9	263	395.8
E06	1	-1	1	0.14	1.6	20	15.6	24.9	201	380.4
E07	1	-1	-1	0.14	1.6	-20	15.6	24.9	200	409.6
E08	-1	1	1	0.1	2	20	12.5	19.9	177	341.7
E09	-1	1	-1	0.1	2	-20	12.5	19.9	177	446.5
E10	-1	-1	1	0.1	1.6	20	15.6	24.9	141	383.2
E11	-1	-1	-1	0.1	1.6	-20	15.6	24.9	142	463.1
E12	1.35	0	0	0.147	1.8	0	13.9	22.1	247	373.9
E13	-1.35	0	0	0.093	1.8	0	13.9	22.1	149	468.2
E14	0	1.35	0	0.12	2.07	0	12.1	19.2	230	370.6
E15	0	-1.35	0	0.12	1.53	0	16.3	26.	160	387.5
E16	0	0	1.35	0.12	1.8	27	13.9	22.1	192	422.3
E17	0	0	-1.35	0.12	1.8	-27	13.9	22.1	191	418.4

Table A.3: Experiment matrix for the second dataset of experiments, with normalized and real values. The "f" and "RPM" columns are values calculated to have a constant cooling time relatively to pulse duration. "E_{pulse}" is the energy (per pulse, in mJ) produced by the laser unit (response value). The "UTS" column is the average UTS of 5 welded couples tested for each set of parameters, given in MPa.

	a_0	a_1	a_2	a_3	a_{12}	a_{13}	a_{23}	a_{123}	a_{11}	a_{22}	a_{33}
E01	1	0	0	0	0	0	0	0	0	0	0
E02	1	0	0	0	0	0	0	0	0	0	0
E03	1	0	0	0	0	0	0	0	0	0	0
E04	1	1	1	1	1	1	1	1	1	1	1
E05	1	1	1	-1	1	-1	-1	-1	1	1	1
E06	1	1	-1	1	-1	1	-1	-1	1	1	1
E07	1	1	-1	-1	-1	-1	1	1	1	1	1
E08	1	-1	1	1	-1	-1	1	-1	1	1	1
E09	1	-1	1	-1	-1	1	-1	1	1	1	1
E10	1	-1	-1	1	1	-1	-1	1	1	1	1
E11	1	-1	-1	-1	1	1	1	-1	1	1	1
E12	1	1.35	0	0	0	0	0	0	1.82	0	0
E13	1	-1.35	0	0	0	0	0	0	1.82	0	0
E14	1	0	1.35	0	0	0	0	0	0	1.82	0
E15	1	0	-1.35	0	0	0	0	0	0	1.82	0
E16	1	0	0	1.35	0	0	0	0	0	0	1.82
E17	1	0	0	-1.35	0	0	0	0	0	0	1.82

Table A.4: Model matrix for the second dataset with a quadratic model.

composed of the constant factor (a_0) and the interactions and quadratics ones. The response is the average tensile test (UTS) values (10 tests) for each set of parameters:

Table A.5 gives the dispersion matrix for the quadratic model (the linear model with

interaction is quite similar and, thus, is not represented here).

0.269	0	0	0	0	0	0	0	-0.10	-0.10	-0.10
0	0.086	0	0	0	0	0	0	0	0	0
0	0	0.086	0	0	0	0	0	0	0	0
0	0	0	0.086	0	0	0	0	0	0	0
0	0	0	0	0.13	0	0	0	0	0	0
0	0	0	0	0	0.13	0	0	0	0	0
0	0	0	0	0	0	0.13	0	0	0	0
0	0	0	0	0	0	0	0.13	0	0	0
-0.10	0	0	0	0	0	0	0	0.15	$-5e^{-4}$	$-5e^{-4}$
-0.10	0	0	0	0	0	0	0	$-5e^{-4}$	0.15	$-5e^{-4}$
-0.10	0	0	0	0	0	0	0	$-5e^{-4}$	$-5e^{-4}$	0.15

Table A.5: Dispersion matrix for the quadratic model.

Then the coefficients (see Table A.6) for the linear with interaction model and the quadratic model can be obtained by equation A.6.

	Lin	Quad
c_0	397.38	382.15
c_1	-17.34	-17.34
c_2	-8.67	-8.67
c_3	-19.78	-19.78

	Lin	Quad
c_{12}	4.75	4.75
c_{13}	16.73	16.73
c_{23}	-2.18	-2.18
c_{123}	4.05	4.05

	Quad
c_{11}	15.22
c_{22}	-7.83
c_{33}	14.83

Table A.6: List of coefficients for both models (Lin = Linear Model with Interaction, Quad = Quadratic Model). The UTS is thus modelled using Equ A.5, as the coefficient values are given in MPa.

Resume

Jonas Vannod
Rue du Jura 1
1023 Crissier
Switzerland

+41 21 634 09 88
jonas.vannod@a3.epfl.ch

Born on February 7, 1983
Single, two children
Swiss citizen

Education

2007–2011	PhD degree in materials science and engineering, EPFL, Lausanne, Switzerland.
2001–2007	Engineering degree in Materials Science and Engineering at Ecole Polytechnique Fédérale de Lausanne (EPFL), Switzerland.

Professional Experience

2007–2011	Teaching assistant at the Computational materials laboratory (LSMX) of EPFL. Teaching assistant at the Inderdisciplinary center for electron microscopy (CIME) of EPFL.
2003	Internship in the R&D division of Tetrapak, Romont, Switzerland (3 months).